Modelling polarization and flux surface observations of Martian mesospheric CO_2 ice clouds during twilight

MSc thesis

N. Hadzisejdic

TU Delft

Modelling polarization and flux surface observations of Martian mesospheric CO_2 ice clouds during twilight

MSc thesis

by

N. Hadzisejdic

to obtain the degree of Master of Science

at the Delft University of Technology,

to be defended publicly on Thursday January 23, 2020 at 01:00 PM.

Student number: 4190785

Project duration: February 25, 2019 – January 23, 2020

Thesis committee:

Dr. D.M. Stam,	TU Delft, supervisor
Prof. dr. L.L.A. Vermeersen,	TU Delft
Dr. A. Menicucci,	TU Delft

An electronic version of this thesis is available at http://repository.tudelft.nl/.
Front image retrieved from
https://visibleearth.nasa.gov/images/86036/night-shining-clouds/860391

TU Delft

Acknowledgements

First of all, I want to express my gratitude for the supervision and guidance by Dr. Daphne Stam. I admire her enthusiasm for the field very much. It was very pleasant working with her on this research for the past year. From the start the goal was quite clear for this research, but in my experience, I had a lot of freedom in the path towards it. I could pour a great deal of my creativity into it and when I lost track, she was always able to change my perspective and help me on my way.

I want to thank my mother, Bosa, and my father, Dalibor, for all the love they have given me and for their part in making me the person I am now. And more concretely, I very much appreciate all the care packages (loads of food) sent to me in the stressful, final weeks of this thesis research.

I can always rely on my friends and roommates. They dragged/kicked me to the campus when morale was low and were available for a laugh when distraction was needed.

Thank you Boris, Umit en Lieke for your time, thoughtful notes and advice that have significantly improved this thesis. Also Boris, lots of thanks for the Photoshop wizardry. I am very happy that you moved from Rotterdam to Delft in these past months so I could see you more often.

A very special thank you is reserved for my girlfriend, Eliza. Her love and support was crucial in achieving all of this. I am very lucky to have her by my side.

Summary

Motivation for research on Martian mesospheric CO_2 ice clouds
Martian mesospheric CO_2 ice clouds are formed out of the main constituent of the Martian atmosphere: CO_2 gas. The nature of these clouds is poorly understood, therefore, characterization of these clouds in terms of particle morphology would give valuable insight into the Martian climate. So far, these CO_2 clouds have only been detected from space. In this Master Thesis, feasibility of a surface-based observation strategy has been investigated to predict the flux and polarization signal of the CO_2 clouds, using a Monte Carlo radiative transfer code. This code was coined PA3S, short for Polarized Atmospheric Spherical Shell Simulation. Simulations with PA3S were performed mostly at three wavelengths in the visible spectrum: 0.4, 0.6 and 0.8 μm. This is because a surface-based instrument would have to receive a sufficient amount of photons from the clouds, discouraging measuring in infrared.

Development and validation of PA3S code
Because measuring during twilight from the start seemed the most promising strategy, a plane-parallel code was not deemed appropriate. PA3S uses spherical shells to simulate lighting conditions during twilight. The code takes the full polarization state into account and allows for simulations of skylight at several solar elevations in one run. The code has been made parallel with OpenMP for better performance. Simulation output was verified using data of the well known single scattering Rayleigh sky polarization portrait from literature, for example Horváth (2014) and Pomozi et al. (2001).

Required inputs for PA3S code
To predict the flux and polarization signal of the CO_2 ice clouds, the relevant constituents of that Martian atmosphere that had to be included in the simulations, have been identified. Next to the CO_2 ice clouds particles, these were CO_2 gas and dust. Optical constant of CO_2 gas were evaluated with Rayleigh scattering theory. Martian dust optical constant were calculated with a combination of experiments from literature. For the CO_2 ice clouds particles, a different approach was required since their shapes and size are not known. Based on experiments of CO_2 ice crystal growth at Martian atmospheric conditions (Mangan et al., 2017), three suggested shapes were considered: cubes, octahedra and cube-octahedra. With the software package ADDA (Yurkin and Hoekstra, 2011), scattering matrices for these shapes were calculated for various particle sizes and wavelengths. Subsequently, scattering matrices of size distributions of these particles were calculated using a size distribution derived from measurements by Määttänen et al. (2010).

Results generated with PA3S
Results have been generated with four combinations of constituents present. Firstly, only results with CO_2 gas are shown to check if second order Rayleigh scattering neutral points occur on Mars. Secondly, simulation results with CO_2 gas and a cloud are given to examine the signal created by the cloud particles. Thirdly, CO_2 gas and dust results are presented to assess the effect of the background dust. Finally, results are shown with all constituents present: CO_2 gas, dust and a CO_2 ice cloud. These are used to predict the flux and polarization signal of the CO_2 ice clouds.

Conclusions on feasibility of surface-based measurements
Firstly, simulation results with only gas showed that no second order Rayleigh scattering neutral points are present in the Martian atmosphere. Furthermore, it was concluded that the influence of the dust is critical, it obscures the clouds far more than the gas. Finally, simulation results suggest that the CO2 clouds are not observable from the surface during the day, however, they are observable during twilight. At low solar elevation angles, the degree of polarization of the cloud varies sharply between 0 and 20% in parts of the sky were a cloud is present and is discernible from the degree of polarization of the background.

Advice on instrument design
Observation from the surface allows for detection of the cloud's degree of polarization at a broad range of scattering angles, which is advisable since it is useful for effective characterization of cloud particle morphology. PA3S simulations suggest that, even though the cloud is observable in the degree of polarization in the twilight zone, the cloud signal consists of a relatively low flux. This has important implications for the instrument design in terms of sensitivity and integration times, among other factors.

Contents

List of Figures

List of Tables

List of abbreviations

ADDA	Amsterdam Discrete Dipole Approximation
AoP	Angle of Polarization
API	Application Programming Interface
CAD	Computer-Aided Design
CPU	Central Processing Unit
CRISM	Compact Reconnaissance Imaging Spectrometer for Mars
DDA	Discrete Dipole Approximation
DoP	Degree of Polarization
ENU	East-North-Up
GCM	General Circulation Model
HDF5	Hierarchical Data Format 5
HRSC	High-Resolution Stereo Camera
IR	Infra-Red
MAVEN	Mars Atmosphere and Volatile Evolution
OMEGA	Observatoire pour la Minéralogie, l'Eau, les Glaces et l'Activité
OpenMP	Open Multi-Processing
PA3S	Polarized Atmospheric Spherical Shell Simulation
PIP	Point-In-Polyhedron
RGB	Red Green Blue
SPICAM	Spectroscopy for Investigation of Characteristics of the Atmosphere of Mars
THEMIS-VIS	Time History of Events and Macroscale Interactions during Substorms - Visible Imaging Subsystem
UV	Ultra-Violet

List of symbols

AoP	angle of polarization	rad
C_{abs}	absorption cross-section	m^2
C_{sca}	scattering cross-section	m^2
DoP	degree of polarization	%
$\bar{E}$	electric field vector	V/m
I	total flux	photons
$\mathbf{I}_0$	intial photon Stokes vector	photons
L	photon path length	km
L_S	solar longitude	rad
N	degree of Gauss-Legendre quadrature, number of weights and abscissae	-
N_L	Loschmidt's number, $2.54743 \cdot 10^{25}$	m^{-3}
N_i	number of photons in a bin	-
N_{gas}	gas column number density	$1/m^2$
P	scattering matrix	-
P_r	randomly sampled probability of scattering in a certain direction	-
P_{SD}	scattering matrix of a size distribution of particles	-
P_{bottom}	pressure at bottom of a layer	Pa
P_{top}	pressure at top of a layer	Pa
Q	linearly polarized flux, flux at 0° minus flux at 90°	photons
Q_{ext}	extinction coefficient	-
S	saturation index	-
U	linearly polarized flux, flux at 45° minus flux at 135°	photons
V	circularly polarized flux	photons
Z	phase matrix	-
a	single scattering albedo	-
a_{cloud}	cloud single scattering albedo	-
az	azimuth in local horizontal frame of a detector	rad
$\mathbf{c}$	center of sphere in Cartesian coordinates	km
d_{max}	maximum path through cloud	km
$\hat{\mathbf{e}}$	East direction at a detector in Cartesian coordinates, unit vector	-
el	elevation in local horizontal frame of a detector	rad
g	gravitational acceleration	m/s^2
k	free wave number	m^-1
m_{gas}	molecular mass of gas	kg
n	complex refractive index	-
$\hat{\mathbf{n}}$	North direction at a detector in Cartesian coordinates, unit vector	-
$n(r_i)$	number of particles of radius r_i	-
n_i	imaginary refractive index	-
n_i	mixing ratio	-
n_r	real refractive index	-
$\mathbf{p}$	position in Cartesian coordinates	km
$\mathbf{p_0}$	last photon position	km
Δp_i	pressure difference in a layer	Pa
$\mathbf{p}_{isct}$	point of intersection	km
p_{surf}	surface pressure	Pa
r	radius	km
r_g	size distribution median	µm
r_i	Gauss-Legendre abscissae mapped to interval of size distribution radii	m

$r_{cl,max}$	maximum cloud radius	km
$r_{cl,min}$	minimum cloud radius	km
r_{eq}	equivalent radius	µm
t	distance to intersection of line and sphere	km
t	time	s
t_{cl}	cloud thickness	km
$\hat{\mathbf{u}}$	up direction at a detector in Cartesian coordinates, unit vector	-
w_{ri}	Gauss-Legendre weights mapped to interval of size distribution radii	-
w_{xi}	Gauss-Legendre weights	-
x	random number from a uniform distribution	-
x	size parameter	-
x_i	Gauss-Legendre abscissae	-
α_{entry}	cloud entry angle	rad
δ	depolarization factor	-
ϑ	elevation in the photon reference frame	rad
θ	scattering angle	rad
θ_S	solar elevation angle	rad
θ_r	randomly sampled scattering angle	rad
λ	latitude	rad
λ	wavelength	µm
$\lambda_{cl,max}$	maximum cloud longitude	rad
$\lambda_{cl,min}$	minimum cloud longitude	rad
μ_g	geometric median	-
σ_g	geometric standard deviation	-
σ_1	angle between original Stokes vector reference plane and scattering plane	rad
σ_2	angle between scattering plane and Stokes vector reference plane after scattering	rad
τ	optical thickness	-
τ_{abs}	absorption optical thickness	-
τ_r	randomly sampled optical thickness	-
τ_{cloud}	cloud optical thickness	-
τ_{dust}	dust optical thickness	-
τ_{gas}	gas optical thickness	-
τ_{layer}	total optical thickness of a layer	-
τ_{sca}	scattering optical thickness	-
φ	azimuth in the photon reference frame	-
ϕ	latitude	rad
$\phi_{cl,max}$	maximum cloud latitude	rad
$\phi_{cl,min}$	minimum cloud latitude	rad
χ	angle of polarization	rad
ψ	azimuthal angle of scattering	rad
ψ_r	randomly sampled azimuthal scattering angle	rad
ω	harmonic oscillation velocity	m/s
Ω	solid angle	sr

1

Introduction

On Mars, an exotic type of clouds exists: high-altitude mesospheric CO_2 ice clouds. These clouds are formed by condensation of CO_2 gas, which is the main constituent of the Martian atmosphere. Numerous analyses have been done on observations from orbiters of these mesospheric clouds (see, among others Montmessin et al., 2007, Määttänen et al., 2010 and McConnochie et al., 2010). In contrast, this research is based on a surface-based observation strategy to deduce cloud particle morphology, specifically during twilight. Lighting conditions during twilight are possibly ideal for observation of the thin clouds since the high-altitude clouds (above 70 km) still receive direct sunlight while the remaining skylight is scattered light. Also, when observing from the surface during twilight, there is no signal from the ground that could obscure the cloud signal. This is illustrated in Figure 1.1. From this context the research goal arises; simulation of the observed signal for different atmospheric conditions to serve as a feasibility study and as input for instrument design. During twilight, all light observed by an instrument from the surface is light coming from the Sun under the horizon. This means that the common plane-parallel atmosphere assumption is not valid. In this research the twilight illumination conditions are simulated with a Monte Carlo radiative transfer code set in a spherical shell atmosphere model. For the purpose of shorter notation, the mesospheric CO_2 ice clouds will often simply be referred to as CO_2 ice clouds in this text.

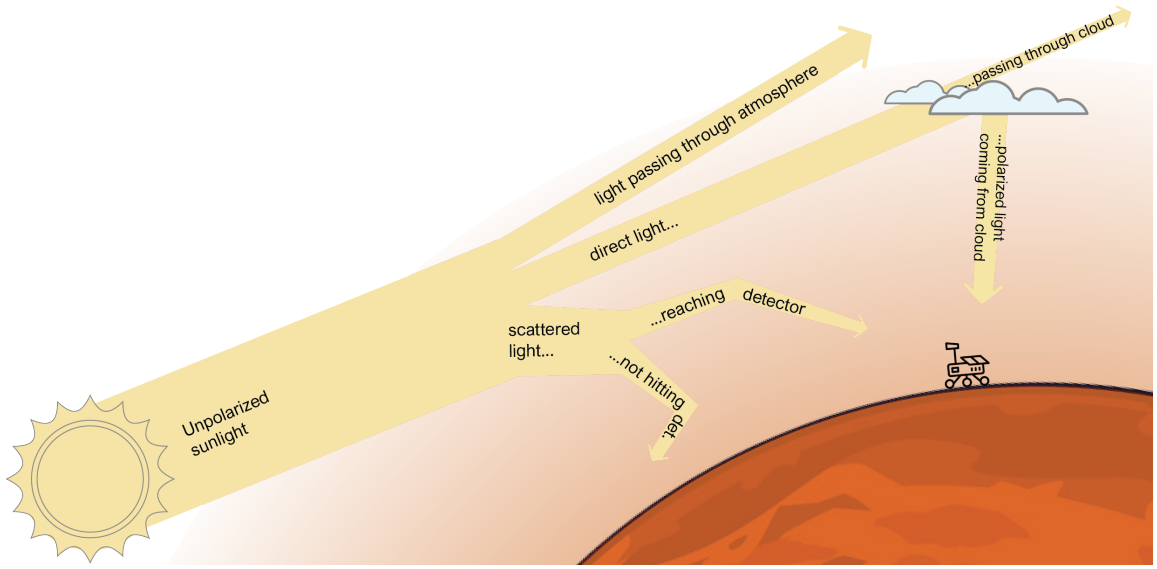

Figure 1.1: This figure illustrates the lighting conditions of the mesospheric clouds during twilight. Because the Sun is below the horizon, skylight reaching a surface-based instrument (mounted on a rover for example) is far weaker than during the day. During twilight the measured light has travelled a long way through the atmosphere and has been scattered by gas and dust, while the high-altitude clouds still receive some direct light that has travelled through the thin high atmospheric layers. Polarization of the light coming from the clouds will be distinct from the light polarized by the gas and dust. [credit: N. Hadzisejdic]

1.1. Current knowledge on mesospheric clouds

The presence of CO_2 ice clouds on Mars is a rare situation in our Solar System in which a major gas constituent of an atmosphere condenses into clouds. In contrast, on Earth, clouds are made of water droplets or water ice, instead of the main constituents of Earth's atmosphere: nitrogen and oxygen. Mesospheric CO_2 clouds are a distinct type of Martian CO_2 clouds that are found at equatorial latitudes and high-altitudes. See Figure 1.2 for a composite image confirmed to be a mesospheric CO_2 cloud detected from orbit by the CRISM instrument, and for a composite image of a cloud presumed to be a mesospheric CO_2 cloud, taken from the Martian surface by the Pathfinder lander. The latter could also be a picture of an H_2O ice cloud, which are much more common. The CO_2 ice clouds have been the subject of substantial research over the years, but the characteristics and formation processes of these clouds are not yet fully understood.

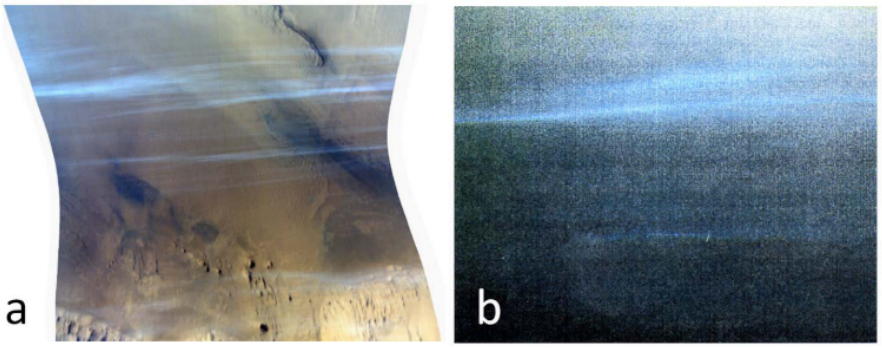

Figure 1.2: Figure from Vincendon et al. (2011). Left image is a RGB color composite of CRISM observations. The right image, also a composite image, is an observation by the Pathfinder lander camera of a cloud at sunrise, often thought to be a CO_2 cloud. The right image could also be a much more common H_2O ice cloud, the image is originally from Clancy and Sandor (1998). There seems to be a similarity in structure of the clouds, the similar blue colors of the clouds might be coincidental since the RGB coloring schemes have been done separately.

Surface and atmospheric temperatures were long considered to be too warm for CO_2 condensation conditions except at high latitudes during Martian fall/winter (Clancy and Sandor, 1998). However, in 1970 the occurrence of such clouds in the mesosphere (>40 km) at low latitudes was first suggested by Herr and Pimentel (1970) based on infrared spectra from Mariner 6 and 7, in which they observed an emission spike at 4.3 μm, suggestive of CO_2 ice. Montmessin et al. (2006) found the first direct observation of the clouds by analyzing stellar occultations recorded by SPICAM on board of the Mars Express. Most sources agree that the mesospheric clouds are composed of CO_2 ice (Clancy and Sandor, 1998; Gondet et al., 2007). Clancy et al. (2007) detected mesospheric clouds at 60-80 km altitudes primarily near the equator.

Seasonal and longitudinal variations in the number of occurrences of mesospheric CO_2 clouds were also found in the study by Clancy et al. (2007). Spiga et al. (2012) state that mesoscale gravity waves have an important part in forming mesospheric cold pockets where temperatures are sufficiently low for CO_2 to condense into clouds. They use a global circulation model to show that gravity waves originating in the troposphere can produce these cold pockets, see Figure 1.3 from Spiga et al. (2012). Figure 1.4 by Spiga et al. (2012), also generated with their model, illustrates a clear correlation between occurrences of mesospheric clouds and zones with gravity wave activity, possibly explaining the longitudinal variations showed by Clancy et al. (2007). Spiga et al. (2012) also state that presumed gravity wave sources, found only within $\pm$ 25° latitude in the troposhere by another study (Creasey et al., 2006), could explain the latitudinal constraints of the mesospheric clouds.

Analysis by Määttänen et al. (2010) suggests that it is very unlikely that the CO_2 clouds are formed by homogeneous nucleation (phase transition without preferred nucleation sites) and that heterogeneous nucleation is very likely. An important question then is which materials act as condensation nuclei at these high altitudes. Are very small dust particles lifted by some process high enough to form clouds at altitudes above 70 km, or are clouds formed around meteoric dust particles just like some high-altitude clouds on Earth? A recent study (Hartwick et al., 2019) states that when they include meteoric smoke

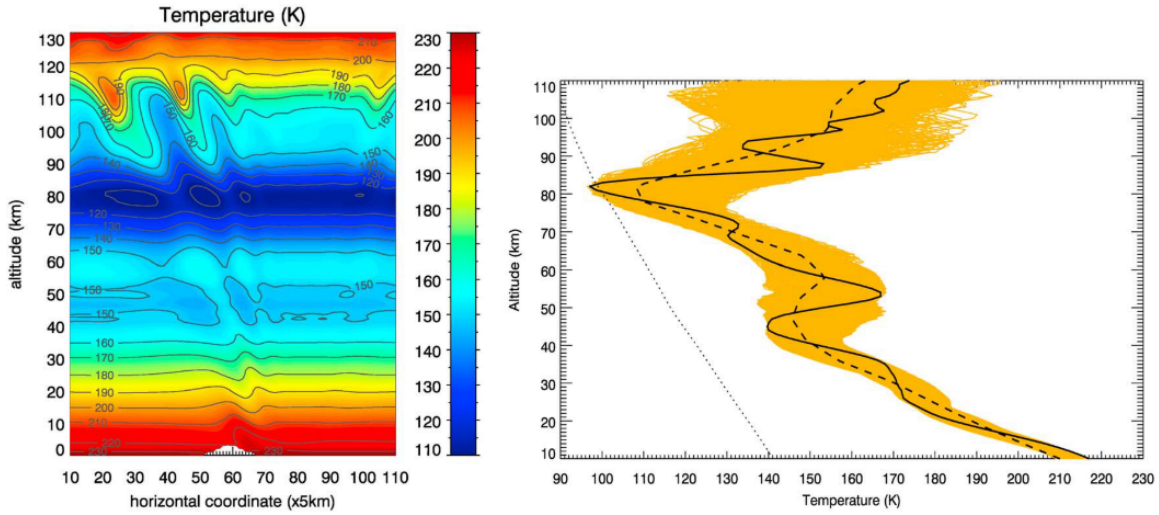

Figure 1.3: Figure from Spiga et al. (2012). The left plot shows a temperature profile of a slice of atmosphere at the equator generated with a global circulation model. The profile results from a simulated troposheric gravity wave. The right plot shows a slice of the left plot (near the center) at several moments in time. The dashed line represents starting conditions, the solid line is the predicted profile after 2 hours, the orange envelope is from several moments in a 3 hour interval after the start. The dotted line is the CO_2 condensation profile from Washburn and West (1948), it is visible that there are moments when condensation conditions are met.

in their general circulation model, they see water ice clouds forming above 30 km altitude. This result is consistent with observations (Smith et al., 2013), while other models have difficulty reproducing the occurrence of water ice clouds at altitudes above 30 km. According to Hartwick et al.: "The MAVEN (Mars Atmosphere and Volatile Evolution) satellite has detected pervasive ionized metallic layers due to meteor ablation at an 80–90 km altitude, which suggests a continuous supply of meteoric smoke particles that settle to lower altitudes." Possibly, mesospheric CO_2 clouds (above 70 km) also form around meteoric nuclei or other interplanetary dust particles.

Määttänen et al. (2010) state that most of the mesospheric CO_2 clouds are cirrus-like clouds, which are thin and sheet-like, in contrast to cumulus clouds which are fluffy. This study presents observations of the CO_2 clouds by two instruments on the Mars Express, OMEGA and HRSC. About 15% of OMEGA observations show large cumulus-like clouds, the rest are cirrus-like clouds. HRSC observation mostly showed cirrus-like clouds. The cumulus-type clouds are thought to possibly be up to 10 km in vertical extent, a value that matches analysis of data from stellar occultations with SPICAM by Montmessin et al. (2006) and analysis of cloud shadows by Montmessin et al. (2007). According to Määttänen et al. (2010), the presence of the cumulus-type clouds in the mesosphere points to the possible existence of mesospheric convection on Mars. They propose two explanations for the existence of the two cloud types. The first explanation is that the clouds are two different stages of the same cloud, cumulus clouds are young mesospheric clouds and cirrus clouds are their older remains. The second explanation is that the two cloud types are formed under different conditions, possibly also following a different nucleation process.

Various crystal sizes have been proposed for the CO_2 ice cloud particles. Isenor et al. (2013) reviewed several studies and found the size estimates presented in Table 1.1. According to Montmessin et al. (2007), the found crystal sizes are unexpectedly high for mesospheric altitudes, implying the presence of atmospheric updrafts in the mesosphere that are strong enough to prevent the particles from falling. These updrafts can be linked to the suspected existence of mesospheric convection and cumulus-type clouds mentioned earlier. All the size estimates in Table 1.1 have been derived assuming Mie theory: a theory that assumes spherical particles. However, there is no indication that the crystals are spheres. A recent study (Aoki et al., 2018) poses that the features they found in spectra of the CO_2 clouds, observed by the Planetary Fourier Spectrometer on the Mars Express, could not be reproduced with Mie theory.

Cubic, octahedral and cubo-octahedral crystal shapes are more likely according to Mangan et al.

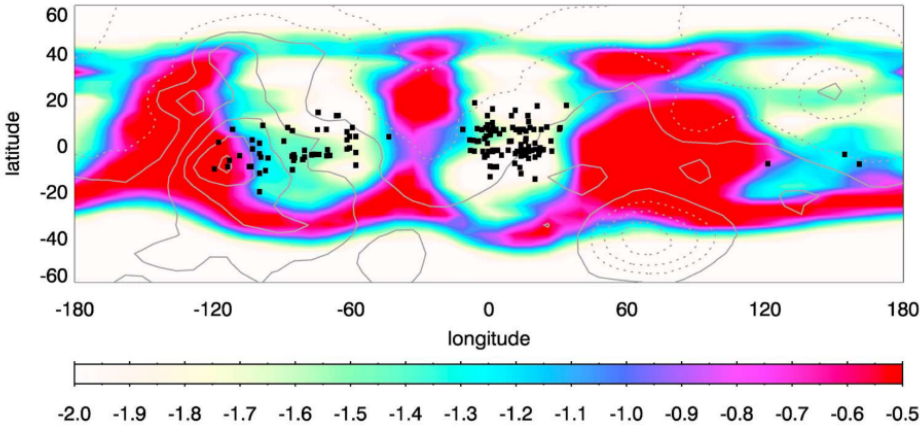

Figure 1.4: This figure is generated with a general circulation model of the Martian atmosphere by Spiga et al. (2012). The color coded quantity is $log_{10}(S)$, where S is the so-called saturation index, representing the ratio between the gravity wave amplitude and the amplitude at which the wave breaks (saturation amplitude). White-blue zones represent areas where S is small enough and therefore gravity wave activity is likely. In red-pink zones S is too large and gravity wave activity is unlikely. The zones are overlaid with black squares representing locations of real mesospheric cloud observations. A clear correlation is visible between the black dots and white-blue zones.

Table 1.1: Comparison of several size distributions of mesospheric cloud particles found in literature. All studies mentioned in this table assumed Mie theory is applicable, i.e the particles are homogenous spheres.

study	**size estimate**	**analyzed observations**
Montmessin et al., 2006	<100 nm	SPICAM UV spectrometer data
Vincendon et al., 2011	0.5–2 μm	CRISM and OMEGA near-IR data
Clancy and Sandor, 1998	0.1–0.3 μm	Pathfinder lander images, Mariner 6 and 7 IR data
Montmessin et al., 2007	1–2 μm	OMEGA visible and near-IR spectrometer data
Määttänen et al., 2010	1–3 μm	OMEGA visible and near-IR spectrometer data
McConnochie et al., 2010	0.1 or 1.5 μm	THEMIS-VIS (visible imaging subsystem) data

(2017). In this study, CO_2 crystals were created by depositing CO_2 gas in a temperature and pressure environment comparable to that of the mesosphere of Mars. The relationship between the three shapes is evident from Figures 1.6 and 1.7 by Mangan et al. (2017). According to the study, the crystal faces can be grouped into two families; the {111}-family and the {200}-family, see Figure 1.7. Different growth speeds of the faces lead to either cubes (sub-figures 5. and 6. in Figure 1.6) or octahedra (sub-figures 1. and 2.), similar growth speeds result in a cube-octahedron (sub-figures 3. and 4.).

Understanding the mechanism behind the condensation of the main component of the Martian atmosphere in high-altitude clouds will expand our knowledge of the CO_2 cycle and more broadly, the Martian climate. Figure 1.8 (Haberle et al., 2017) presents an overview of the radiation budget in the Martian atmosphere, showing the main interactions between light and atmospheric constituents, it is clear that clouds play a significant part in the radiation budget. According to Montmessin et al. (2007) ,the CO_2 cycle has a significant influence on the climate of Mars. For example, formation of CO_2 frost on the Martian surface can produce seasonal mean surface pressure variations of more than 30%, a part of this frost is due to direct deposition and some of it is caused by precipitation resulting from cloud formation. The exact contribution due to precipitation is unknown. Montmessin et al. (2007) also mention that the condensation of clouds particles from the main constituent of an atmosphere, results in microscopic pressure gradients, differing from the diffusion-driven growth that dominates on Earth, Titan, Venus and in the formation of Martian water ice clouds.

The mesospheric CO_2 clouds have exclusively been observed with limb measurements, which practically allows for detection at small scattering angles (forward-scattering) and large scattering angles (backward-scattering). Detection over a broad range of scattering angles is of interest because it is easier to deduce particle shapes (Hansen and Travis, 1974). In turn, information on particle shapes

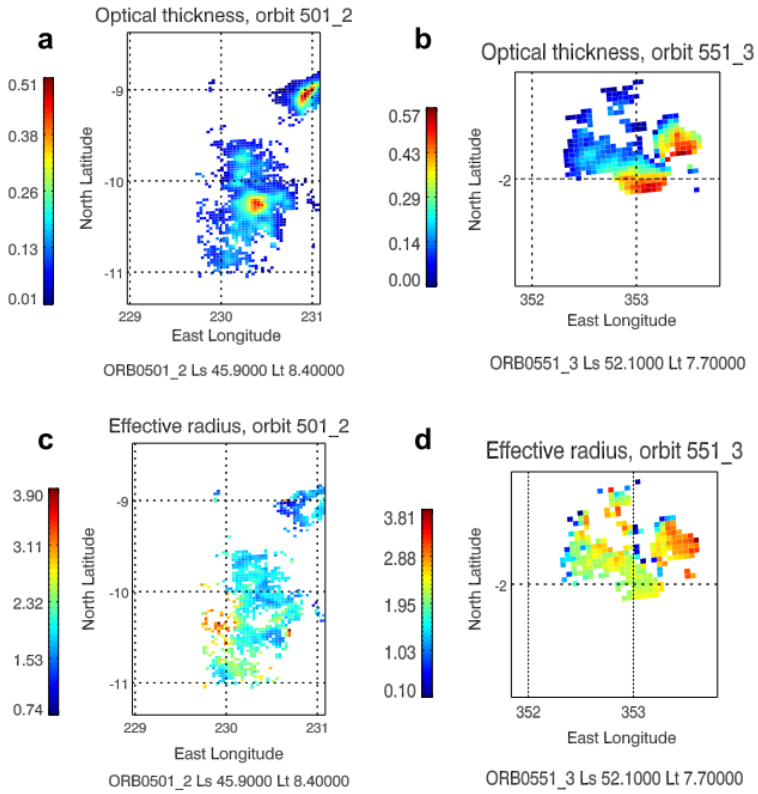

Figure 1.5: Figure from Määttänen et al. (2010) showing optical thickness (top) and effective particle radii (bottom) of two mesospheric CO_2 ice clouds, determined from two OMEGA observations on board of the Mars Express.

can shed light on cloud formation conditions and identification of condensation nuclei. Detection at a broader range of scattering angles from space is technically possible, but it is complicated by constraints an orbit might put on the viewing geometry and on illumination conditions. An option could be to place a satellite in an orbit over the twilight zone. However, this is very unusual and would probably require an orbit designed specifically for this purpose. Furthermore, from space, light reflected by the surface can obscure the cloud signal when the clouds are not observed in the limb. Unlike space-based observations, surface-based observations can detect the clouds from a broad range scattering angle more easily. This is possible when a cloud passes over or when a cloud large in horizontal extent is overhead. The mesospheric CO_2 ice clouds are usually stretched out in East-West direction (Haberle et al., 2017), meaning that the same cloud could potentially be detected at a broad range of scattering angles under the same lighting conditions. For this purpose, an instrument like FlySPEX (Snik et al., 2016) is especially interesting because it can detect most of the sky at once.

1.2. Research objectives and motivation

The aim of this research is to contribute to the current knowledge of the Martian atmosphere. Characterization of mesospheric CO_2 ice clouds could increase insight into the formation conditions and formation processes. Present-day strategies for characterization have shown to be insufficient. A different strategy is suggested: observing the flux and polarization signal of mesospheric clouds from the Martian surface during twilight. Particularly the polarization signal can offer insight into cloud particle morphology. Lighting conditions could be optimal during twilight because of the lack of strong atmospheric and surface signals, see Figure 1.1. This scenario is comparable to that of noctilucent clouds on Earth (thin high atmosphere clouds), which are only visible to the naked eye during twilight. An instrument like FlySPEX, developed as a collaborative effort by several Dutch organisations (Snik et al., 2016), could be an interesting candidate. This research investigates the feasibility of a surface-based approach and aims to supply data for proper adaptation of an instrument to such an observation strategy.

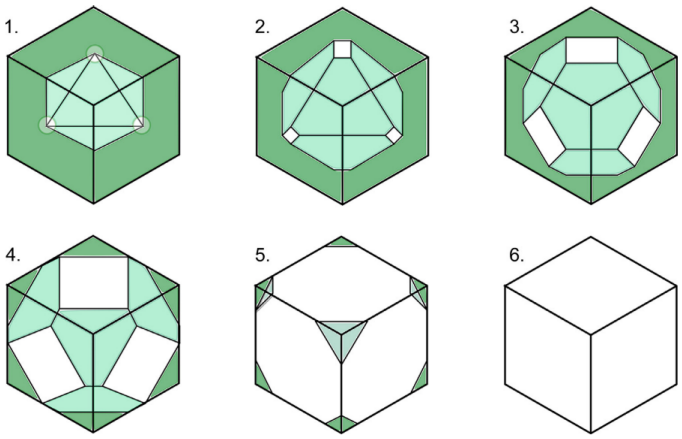

Figure 1.6: Figure from Mangan et al. (2017) depicting the relation between the three suggested CO_2 ice crystal shapes: cubic (5 and 6), octahedral (1 and 2) and cube-octahedral (3 and 4). Different growth speeds of the face families (see Figure 1.7) result in cubes or octahedra, roughly equal speeds result in cube-octahedra

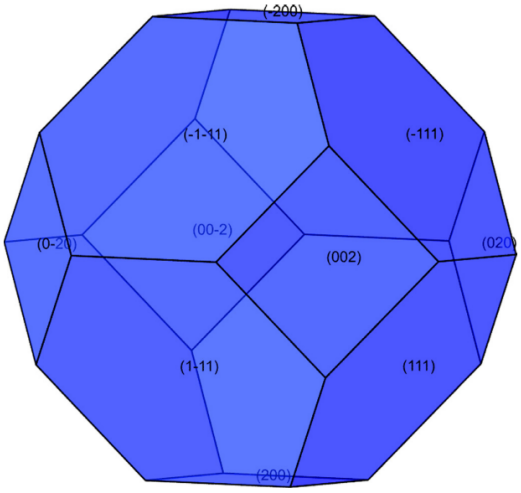

Figure 1.7: Figure from Mangan et al. (2017) showing the two families of faces, {111} and {200} on a crystal that currently has a cube-octahedron shape. Faster growth of the {111} family compared to that of the {200} family results in a cube shape (sub-figures 5. and 6. in Figure 1.6). In the reversed situation, the resulting shape is an octahedron (sub-figures 1. and 2. in Figure 1.6). Roughly equal growth rates of the faces produce cubo-octahedra (sub-figures 3. and 4.).

From this context the research objective arises. The objective of this research is to predict the flux and polarization signals of mesospheric CO_2 ice clouds as observed from the Martian surface during twilight for different atmospheric conditions, using a spherical shell radiative transfer code. The effects of the main constituents of the Martian atmosphere on the observations and on the skylight polarization in general during both day and twilight will also be investigated. As a secondary priority, this research aims to deliver a radiative transfer model that can adequately model the scattering of polarized light in atmospheres and/or lighting condition where sphericity is non-negligible.

The scope of the research will be limited to making predictions of the signals. No conclusions will be made on what various results could mean in terms of cloud formation conditions and formation processes. Consequently, no conclusions will be made regarding the influence of hypothetical formation conditions and processes on atmospheric models. The main goal is modelling skylight polarization signals that can indicate what kind of instrument and observation strategy could accurately characterize the mesospheric clouds. Our results can be used to investigate the required instrumental design. In this research, no *definite* conclusions will be made regarding the feasibility of a surface-based observation strategy and no conclusions will be made regarding the instrument design.

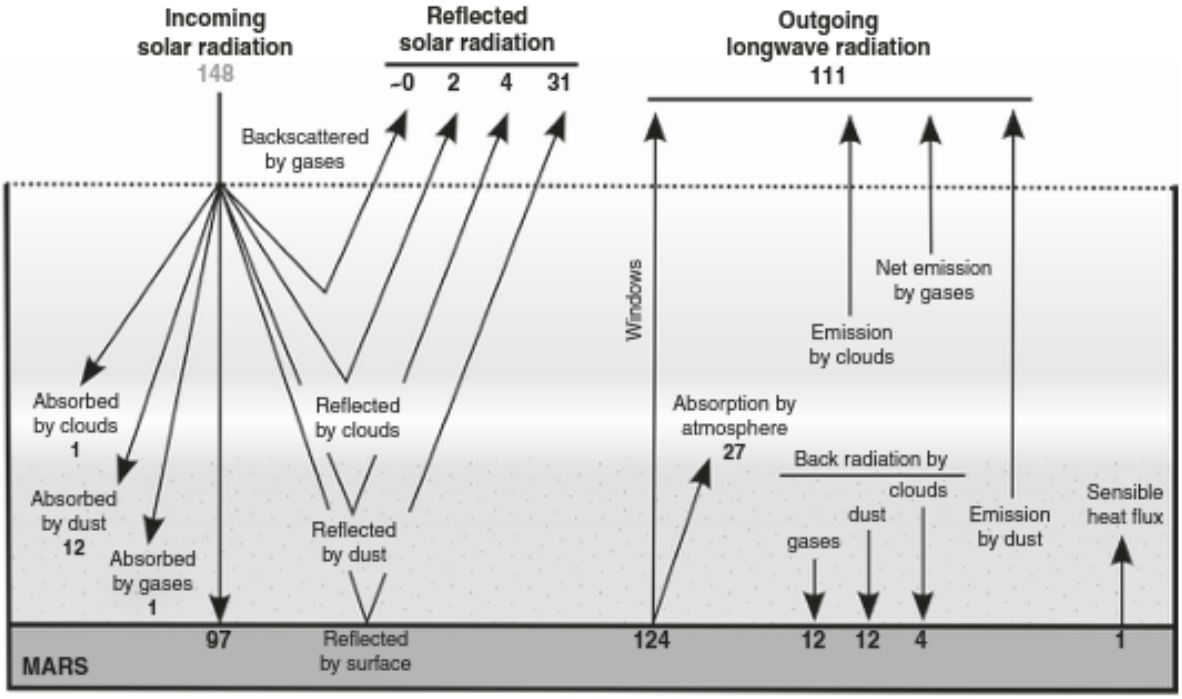

Figure 1.8: Figure from Haberle et al. (2017, p. 107) showing the radiation budget of the Martian atmosphere. Main constituents that influence temperature are CO_2 gas, dust particles and clouds.

1.3. Simulation approach

The code developed and used to simulate skylight during twilight on Mars is named PA3S (Polarized Atmospheric Spherical Shell Simulation) and is a Monte Carlo simulation. A Monte Carlo simulation repeats a stochastic experiment multiple times, constantly sampling from a probability distribution. The aim of such a code is to accurately simulate the underlying processes that shape the problem. In this case the experiment is a photon packet (often referred to as a photon) travelling through an atmosphere. The photon is released from a source, it propagates through the planetary atmosphere until it interacts with gas, dust or cloud particles. Interaction constitutes scattering or absorption, and this goes on until the photon escapes the atmosphere, is completely absorbed or arrives at a detector. We include numerical detectors on the Martian surface to store the photon's Stokes vectors. This experiment is repeated numerous times.

A drawback of a Monte Carlo approach is that a lot of experiments (photon paths) are necessary before strong fluctuations in the output due to random sampling errors are at an acceptable level. This large number of photon paths can result in long computation times. However, a huge advantage of this method is the flexibility. As mentioned earlier, for twilight illumination conditions, assuming a plane-parallel atmosphere is unacceptable since the Sun is below the horizon, see Figure 1.1. Introducing a spherical geometry would greatly increase the complexity of multiple scattering methods like the doubling or adding method (Hansen and Travis, 1974; de Haan et al., 1987). With a Monte Carlo simulation, a photon path can be seen as successive single scattering events. Furthermore, an arbitrary amount of layers, photon sources and detectors can be added and the sources and detectors can be moved around to simulate various lighting conditions. Also, the layers can be filled with a region containing atmospheric constituents differing from the otherwise homogeneous layer, simulating the presence of a cloud.

The code takes the full polarization state into account. It is possible that the clouds are not visible in the flux because of the presence of dust. However, they could still be visible in the polarization signal. Polarization by the mesospheric clouds will be distinct from the signal coming from light scattered by gas and dust. Also, the polarization signal of a cloud could be very useful for characterizing the morphology of the particles that constitute the cloud. This research focuses on scattered sunlight

and therefore visible wavelengths. A surface-based instrument will need to receive enough photons meaning that measuring in the infrared is not practical. Measuring in the infrared is further discouraged by the fact that the larger the wavelength is with respect to particle radius, the less useful information can be deduced from the scattered light. Simulations of the code are done at three wavelengths in the visible spectrum: 0.4, 0.6 and 0.8 μm.

1.4. Report structure

Chapter 2 deals with the basics of radiative transfer and single scattering theory in the Martian atmosphere. The chapter also describes the main scatterers and gives methods to determine the optical properties for two scatterers (CO_2 gas and dust) for implementation in the PA3S code. Next, Chapter 3 details the methodology for finding optical properties of the third scatterer, which is the main constituent of the mesospheric clouds: CO_2 ice. These are calculated with the ADDA software package. ADDA is not to be confused with the Monte Carlo radiative transfer PA3S code, which has been developed for this research. The PA3S code is the focus of Chapter 4. Features of the code are described and a high-level description of the algorithm is given. Also, the code output validation is detailed. Output is compared with features of the single scattering Rayleigh sky. The results for simulations of the mesospheric clouds in the Martian atmosphere are presented in Chapter 5 for different atmospheric conditions. Subsequently, advice is given for the observational strategy in Chapter 7. Also, applicability of the code to other situations is dealt with in this chapter and possibilities for future work are briefly discussed.

2

Radiative transfer in the Martian atmosphere

This chapter covers the radiative transfer theory implemented in the PA3S code. First, Section 2.1 describes how to consider and describe polarization and introduces the Stokes parameters. Next, Section 2.2 deals with single scattering theory and identifies the required optical properties that had to be determined for the scatterers in the Martian atmosphere. The choice for using three types of scatterers (CO_2 gas, dust and CO_2 ice) is justified in Section 2.3. Subsequently, Sections 2.4 and 2.5 present methods to find these optical constant for CO_2 gas and dust, respectively (CO_2 ice is detailed in Chapter 3). Finally, Section 2.6 describes how to combine multiple types of scatterers in one atmospheric layer. A visual introduction of some of the concepts featured in this chapter is presented in Figure 2.1. The chapter ends with Table 2.2, giving an overview of how the relevant optical properties have been derived in this research.

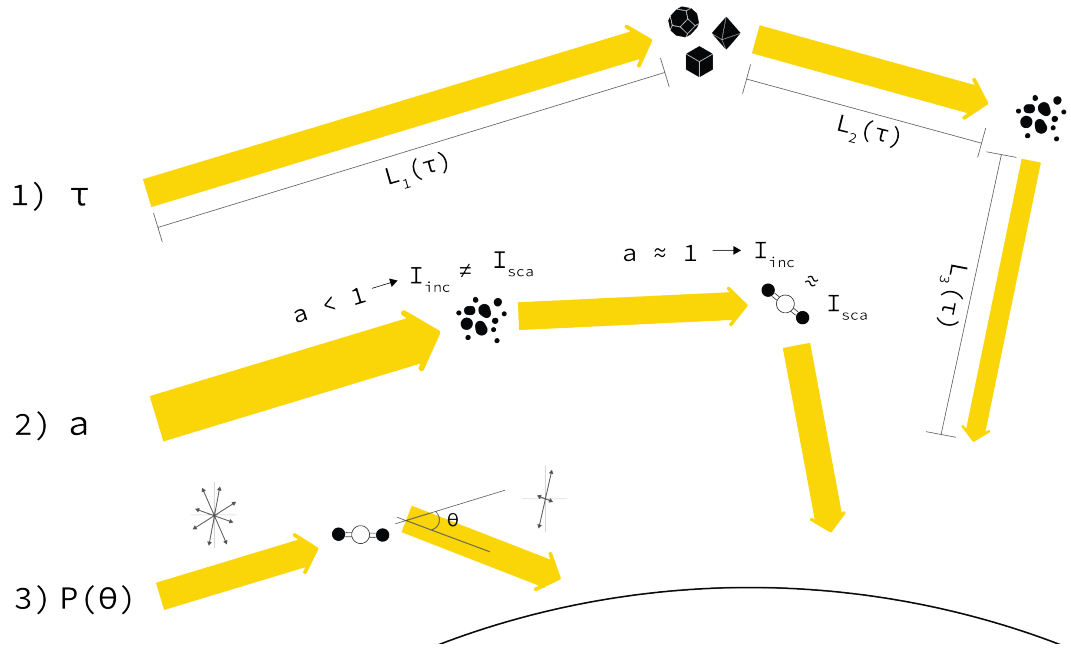

Figure 2.1: This figure schematically summarizes the main concepts described in this chapter that are fundamental for the functioning of the PA3S code. Yellow arrows represent photon packets, the width of the arrow represents the total amount of flux. The code takes the full polarization state of light into account described by the Stokes parameters (Section 2.1). Single scattering (Section 2.2) is dictated by three quantities: **1)** optical thickness, τ, influences the path lengths between interactions **2)** single scattering albedo, a, determines the ratio of light that is scattered vs. absorbed : **3)** scattering matrix, $P(\theta)$, determines the direction of scatter, θ (and ψ, not depicted) and the polarization state after scattering. Three different types of scatterers (justified in Section 2.3) are featured in the code: CO_2 gas (Section 2.4), Martian dust (Section 2.5) and CO_2 ice (Chapter 3).

2.1. Polarization and Stokes vectors

All notations in this section are based on Hansen and Travis (1974). Polarization describes the course of the electric field vector tip of a collection of electromagnetic waves. If this path is not completely random, the wave is polarized to some degree. If this path is a random movement, the wave is unpolarized. Natural light is unpolarized when leaving its source. In general, the electric field vector of a polarized electromagnetic wave traces a helix in 3D space (an ellipse when projected onto a plane). See the rightmost plot in Figure 2.2.

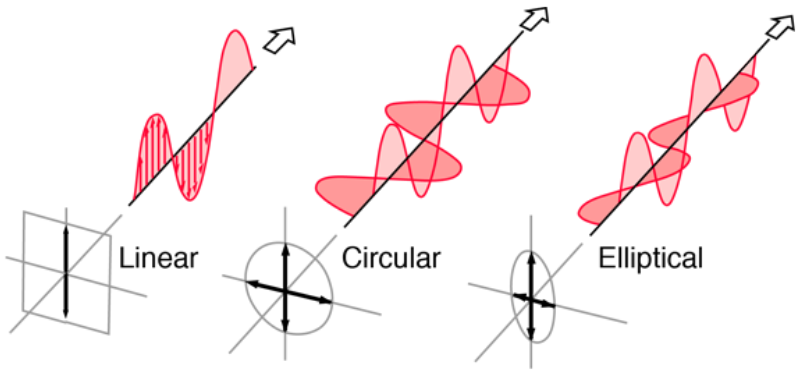

Figure 2.2: Depictions of linearly, circularly and elliptically polarized light waves. Figure from Nave, C. R. (2017).

The most intuitive way to express the polarization of light is with intensity (or flux), degree of polarization, shape of the polarization ellipse and angle of polarization. This set of quantities is useful for presenting observations or simulation output. Intensity represents the amount of energy coming from a specific direction, per area, per unit time, within some solid angle (units are [W m^{-2} sr^{-1}]). It is also common to describe the amount of energy in terms of flux, this quantity is used in this research. Flux is simply intensity integrated over the whole solid angle (units are [W m^{-2}]). The reason for using flux is that Monte Carlo methods naturally work with it[1]. Total flux is the sum of the polarized and unpolarized flux

$$I = I_{unpol} + I_{pol} \, . \tag{2.1}$$

Degree of polarization of the collection of waves is defined as

$$\frac{I_{pol}}{I} = \frac{I_{pol}}{I_{unpol} + I_{pol}} \, . \tag{2.2}$$

Special cases of the general elliptical case are pure linear and circular polarization (left and middle plots in Figure 2.2. The elliptical polarized intensity can be expressed as a combination of these two special cases:

$$I_{pol} = \sqrt{I_{lp}^2 + I_{cp}^2} \, . \tag{2.3}$$

The electric field vector of a beam can be split up into two mutually perpendicular components. Directions of these components are the unit vectors **r** and **l** and the propagation direction is $\mathbf{r} \times \mathbf{l}$. Subsequently, it is possible to denote the angle of polarization in the plane formed by **r** and **l** with angle χ. It is the angle between **l** and the semi-major axis of the polarization ellipse. In case of linear polarization the ellipse collapses into a line and χ is simply the angle between this line and **l**. In Figure 2.3 an isolated 2D view of the polarization ellipse with **r**, **l** and χ is presented. Figure 2.4 by Zhao et al. (2018) shows

[1] Nevertheless, the symbol I normally referring to intensity is used in this research to refer to flux because it is commonly used for one of the Stokes parameters (described later in this section).

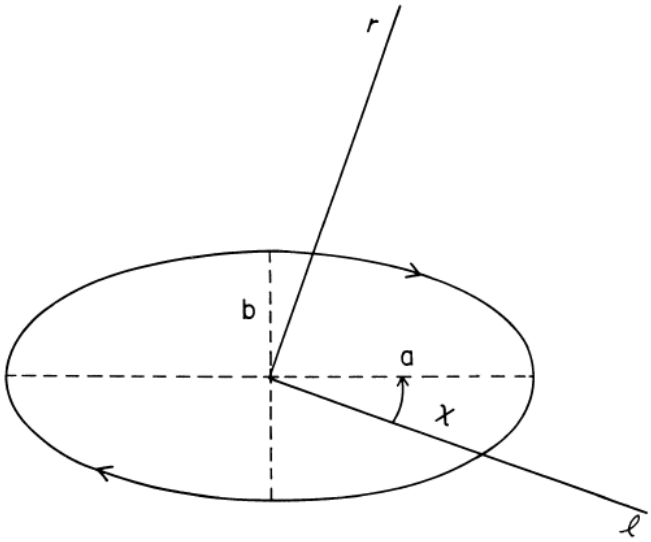

Figure 2.3: Geometric depiction of polarization from Hansen and Travis (1974). Values a and b are the semi-major axis and semi-minor axis, respectively. Angle χ is the orientation of the ellipse.

the electric field vector $\bar{E}$ and χ in the context of an observer receiving incoming light when looking at the sky-dome. In this figure, χ is with respect to the local meridian plane, which is the plane that contains the observed point (P), the observer (O) and zenith (Z)

For implementation of polarization in numerical methods it is often useful to apply another set of four parameters to describe the polarization. These parameters are called the Stokes parameters. Although they are less intuitive than the aforementioned description of polarization (intensity/flux, degree of polarization, shape of the polarization ellipse and angle of polarization) they are mathematically more convenient. The Stokes parameters (often written as the Stokes vector $\mathbf{l} = [I, Q, U, V]$) come in a handful of different varieties. The Stokes parameters as used in this research are the same as defined in Hovenier et al., (2004).

The Stokes parameters are defined with respect to a reference plane, often it is the plane containing **l** and the propagation direction, $\mathbf{r} \times \mathbf{l}$, though other conventions are possible. For example, in the context of Figure 2.4 it is possible to define the incoming Stokes vector with respect to each local meridian (plane OPZ) or with respect to the solar meridian (plane OSZ). Stokes parameter I represents the total flux. Q and U are the linearly polarized fluxes. Positive Q indicates polarization in the **l** direction (corresponding to $\psi = 0°$, parallel to the reference plane), negative Q indicate polarization in the **r** direction ($\psi = 90°$, perpendicular to the reference plane). U is similar but corresponds to $\psi = 45°$ (positive) and $\psi = 135°$ (negative). V is the circularly polarized flux. A right-handed V is positive values and a left-handed V is negative. Right-handed circular polarization means that when looking in the propagation direction the electric field vector is moving in the clockwise direction.

It is useful and straightforward to transform the Stokes parameters to the traditional description using intensity/flux, degree of polarization, shape of the polarization ellipse and angle of polarization (e.g. for presentation purposes and comparison with measurement). Looking at Equation 2.1 it easy to see that the total flux is always greater than or equal to the total polarized flux

$$I \geq \sqrt{Q^2 + U^2 + V^2}\,. \tag{2.4}$$

Thus, the total polarized flux in terms of Stokes parameters can be written as

$$I_{pol} = \sqrt{Q^2 + U^2 + V^2}\,. \tag{2.5}$$

Therefore, the degree of polarization (Equation 2.2) in terms of the Stokes parameters is

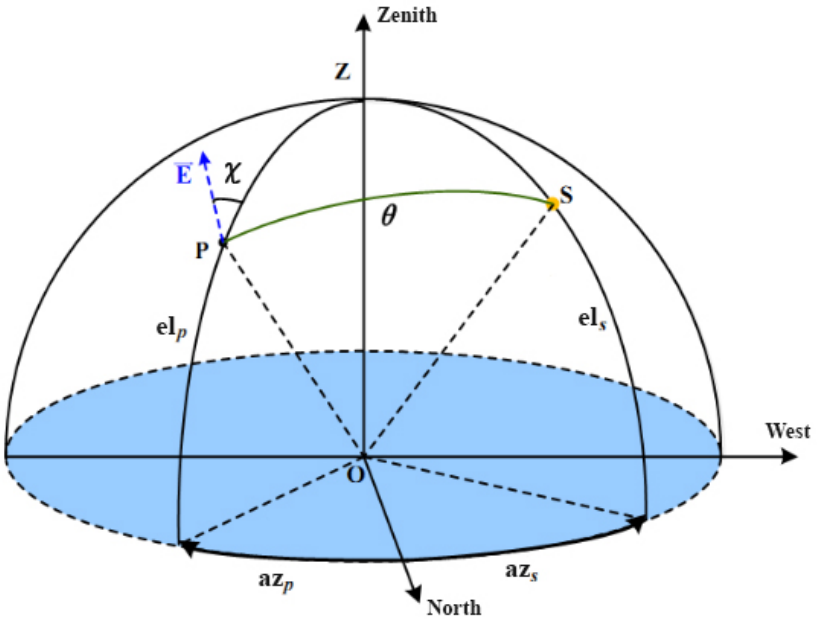

Figure 2.4: Figure adapted from Zhao et al. (2018) (a few variable and axis names have been changed), showing the electric field vector $\bar{E}$ and angle of polarization, χ, at one point observed in the sky. In this plot χ, is defined with respect to the local meridian of the observed point P. If the incoming light at P has scattered only once, the plane containing P and S is referred to as the scattering plane and θ is the scattering angle.

$$\frac{I_{pol}}{I} = \frac{\sqrt{Q^2 + U^2 + V^2}}{I} , \tag{2.6}$$

the linearly polarized flux equals

$$I_{lp} = \sqrt{Q^2 + U^2} \tag{2.7}$$

and the circularly polarized flux is

$$I_{cp} = V . \tag{2.8}$$

The angle of polarization can be found with

$$tan\, 2\chi = U/Q . \tag{2.9}$$

With Equation 2.9 two values for χ are found. The convention is to use the value of χ that results in $cos\, 2\chi$ and Q having the same sign.

Furthermore, it is often useful to express the Stokes parameters with respect to different planes. For instance, in the code developed for this study a photon can scatter and thus change direction. The Stokes parameters were defined with respect to the old propagation direction and unit vector $\mathbf{l}$. The Stokes parameters have to be rotated to the new reference plane after scattering. A rotation of Stokes vector $\mathbf{I}$ over an angle α to a new Stokes vector $\mathbf{I}'$ can be performed with a rotation matrix:

$$\mathbf{I}' = L(\alpha)\,\mathbf{I} = \begin{bmatrix} 1 & 0 & 0 & 0 \\ 0 & cos(2\alpha) & sin(2\alpha) & 0 \\ 0 & -sin(2\alpha) & cos(2\alpha) & 0 \\ 0 & 0 & 0 & 1 \end{bmatrix} \begin{bmatrix} I \\ Q \\ U \\ V \end{bmatrix} . \tag{2.10}$$

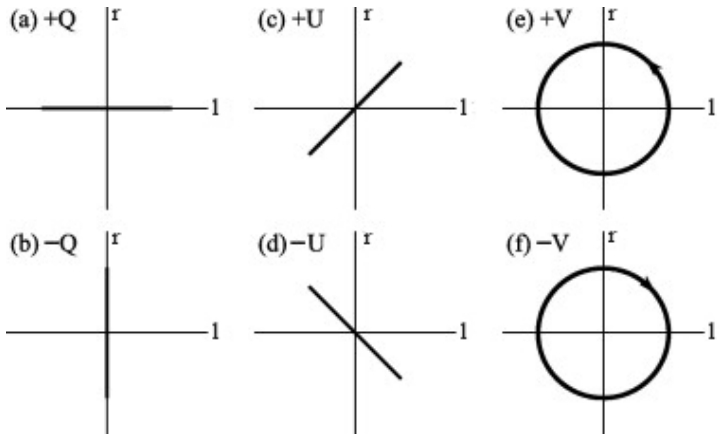

Figure 2.5: Figure from Kislat et al. (2015) showing the conventions for positive and negative Q, U and V.

According to Hovenier and Van der Mee (1983): "α is positive in the anti-clockwise direction, when looking in the direction of propagation". From Equation 2.10 it is clear that rotating over an angle π results in the same Stokes vector ($L(\pi)$ becomes the identity matrix).

2.2. Single scattering

When a photon packet interacts with the medium it will be absorbed, scattered or some combination of the two. In this research, photon packets are occasionally referred to simply as photons. It is assumed that light scatters without change of wavelength in the Martian atmosphere, an assumption known as elastic scattering. On Earth, approximately 97% of sky light is due to elastic scattering, only 3% is due to inelastic scattering, specifically due to a process called Raman scattering (Young, 1981). Invoking Raman scattering is more of a practical concern for atmospheres that are thicker than the Martian atmosphere (Haberle et al., 2017, p. 119). Also, considering the fact that the code for this study will serve mainly to predict observations from the surface for instrument design data, the above assumption is valid for the required precision of the solution.

The scattering particles are assumed to all be far enough from each other that no coherence in scattering occurs. Phrased differently, all particles are in each other's far-field zone and thus no coherent scattering behaviour occurs. Planetary atmospheres, like that of Mars, satisfy this condition (Hansen and Travis, 1974, Chapter 2).

Optical thickness or optical depth is a useful concept in atmospheric sciences to describe the transparency or opaqueness of a medium. Optical thickness, τ, over a given distance is the number of mean free paths of a photon in the medium. The mean free path is the average distance travelled by a photon between interactions. In general, τ is strongly wavelength dependent, photons of shorter wavelengths experience a higher optical thickness and thus scatter or absorb more often over the same distance. This phenomenon causes our daytime sky to be blue instead of red. The photons will not travel exactly the optical thickness between interactions. It is a stochastic quantity, the average number of mean free path lengths of a very large number of photons will approach the optical thickness of the medium. The total optical thickness is the sum of the scattering optical thickness and absorption optical thickness. Scattering optical thickness represents the mean free path between scattering interactions and absorption optical thickness the mean free path between absorption interactions:

$$\tau(\lambda) = \tau_{sca}(\lambda) + \tau_{abs}(\lambda) \ . \tag{2.11}$$

On average, after a photon packet has travelled the optical thickness, τ, it will interact with the atmosphere through scattering and/or absorption. In general, the scattered Stokes vector can be expressed in terms of the incident Stokes vector multiplied by some matrix that is a function of the scattering angle, the wavelength and the orientation of the scattering particle (Hansen and Travis, 1974, Section 2.3)

$$\mathbf{I}_{sca} = Z\left(\mathbf{n}_{inc}; \mathbf{n}_{sca}; \alpha, \beta, \gamma\right) \mathbf{I}_{inc} \,. \tag{2.12}$$

Here Z is the so-called 4×4 phase matrix. As mentioned in Section 2.1 the Stokes parameters are always defined with respect to some plane of reference. Phase matrix Z relates the incident and scattered Stokes parameters each defined with respect to their own plane of reference. The scattering matrix P relates incident and scattered light with respect to the scattering plane, the plane containing the incident and scattered directions. The distinction between P and Z is important because oftentimes the P matrix is measured experimentally or generated numerically.

The whole of P describes in what direction the incident radiation is scattered and what the polarization state will be of the scattered radiation. Element P_{11} is called the phase function and describes the probability incident radiation is sent in a certain direction. The probability that the direction of scatter is in any direction in a unit sphere is 1. Therefore, integrating the phase function over all solid angles and multiplying by the normalizing constant gives (Hansen and Travis, 1974)

$$\int_{4\pi} P_{11} \frac{d\Omega}{4\pi} = 1 \,. \tag{2.13}$$

Hansen and Travis (1974) state that with spherical particles *or* with randomly oriented irregularly shaped particles with half the particles being mirror images of each other, the scattering matrix can be simplified to six independent elements:

$$P(\theta) = \begin{bmatrix} P_{11}(\theta) & P_{21}(\theta) & 0 & 0 \\ P_{21}(\theta) & P_{22}(\theta) & 0 & 0 \\ 0 & 0 & P_{33}(\theta) & -P_{43}(\theta) \\ 0 & 0 & P_{43}(\theta) & P_{11}(\theta) \end{bmatrix}, \tag{2.14}$$

all the elements depend on the scattering angle θ and in general on the wavelength.

Z and P are related through

$$Z\left(\mathbf{n}_{inc}; \mathbf{n}_{sca}\right) = \frac{C_{sca}}{4\pi} L(\pi - \sigma_2) P(\theta) L(-\sigma_1) \,. \tag{2.15}$$

The angle σ_1 is the angle between the plane of reference of the incident beam and scattering plane. Similarly, σ_2 is the angle between scattering plane and the plane of reference of the scattered beam. C_{sca} is the scattering cross-section of a particle. The total energy scattered by a particle is equal to the incident radiation falling on the scattering cross-section, this is how the scattering cross-section is defined. The total extinction cross-section is the sum of contributions by scattering and absorption (Hansen and Travis 1974)

$$C_{ext} = C_{sca} + C_{abs} \,, \tag{2.16}$$

from this, the single scattering albedo, a, can be found. It is the ratio between the scattered radiation and the total removed energy from the incident radiation:

$$a = \frac{C_{sca}}{C_{ext}} = \frac{C_{sca}}{C_{sca} + C_{abs}} = \frac{\tau_{sca}}{\tau_{ext}} = \frac{\tau_{sca}}{\tau_{sca} + \tau_{abs}} \,. \tag{2.17}$$

Now, for a photon packet interacting with the atmospheric medium, taking into account absorption, the scattered Stokes vector becomes

$$\mathbf{I}_{sca} = a\, Z\left(\mathbf{n}_{inc}; \mathbf{n}_{sca}\right) \mathbf{I}_{inc} \,. \tag{2.18}$$

Particle size has a large influence on the scattering behaviour. Specifically, what matters is how large the particles are in comparison to the wavelength of the considered radiation. The size parameter $x = 2\pi r_{eq}/\lambda$ is often used to compare to different situations of particle size or wavelength. Here, r_{eq} represents the equivalent radius; the radius of a sphere that contains a volume equal to that of the particle. Several theories exist to find single scattering matrices P (see chapter 2 of Hansen and Travis (1974)) in three scattering regimes: 1) $x << 1$, Rayleigh scattering is applicable 2) $x \approx 1$, Mie scattering, particles are assumed to be homogeneous spheres 3) $x >> 1$, light-wave can be represented as a beam, ray-tracing is applicable in some cases in this regime.

The approach in this research was to find P, a and τ for the relevant Martian atmospheric constituents at the wavelengths of interest (visible spectrum). The relevant constituents are identified in Section 2.3.

2.3. Identifying relevant atmospheric constituents

Atmospheric scattering constituents are usually split up into molecules (gases) and aerosols (clouds and dust). However, in this research, the scatterers are grouped as gaseous constituents, dust and clouds. This distinction fits the way the code is built, gas and dust fill an entire layer homogeneously while the horizontal and vertical extent of a cloud is adjustable.

Gaseous constituents
Table 2.1 shows the gaseous constituents of the Martian atmosphere (Haberle et al., 2017, Table 4.3). CO_2 gas makes up 95% of the gases in the Martian atmosphere. Significant amounts of nitrogen (2%) and argon (2%) are also present. The most abundant trace gases are in order of decreasing abundance: oxygen, carbon monoxide and water vapor.

Clouds
Water vapor and CO_2 can condense to form thin clouds. Mars has a large variety of clouds in its atmosphere. An overview of the different varieties is given in Table 5.1 in Haberle et al. (2017, pp. 80-81). Unlike clouds on Earth, all clouds on Mars are ice clouds. Most clouds on Mars are cirrus clouds which are thin and sheet-like, in contrast to cumulus clouds which are fluffy.

Dust
The Martian atmosphere contains a high quantity of suspended dust particles. Dust is present throughout the whole year; this background dust has an optical thickness of approximately 0.2 in regions near the equator (Montmessin et al., 2007). There is also a strong seasonal dependence: the Martian dust cycle consists of a ”non-dusty season” and a ”dusty season”. During southern winter (aphelion) the dust optical thickness is relatively low and stable, during southern summer (perihelion) it is relatively high and variable (Lemmon et al., 2015). The seasonal dependence has a significant impact on the climate, as global temperatures can rise 10-15 K during perihelion (Clancy et al., 2000). Planet-wide dust storms occur once every few Martian years.

Constituents that will be taken into account in the code are CO_2 gas, CO_2 ice clouds and dust. The scattering of water vapor, argon, nitrogen and other trace gases is very similar to that of CO_2 gas: it is all Rayleigh scattering but with a slightly different depolarization factor (detailed in Section 2.4). Since these trace gases are not present in high amounts (except occasionally water vapor near areas where a lot of water ice evaporates) their effect is minimal and will not be considered.

As presented in Table 2.1, CO_2 gas constitutes 95% of the gases in the Martian atmosphere. CO_2 ice cloud particle shapes and sizes are not known are not definitely. Predictions and suggestions have been given (with references) in Section 1.1. As also mentioned before, dust plays a significant role in the transfer of electromagnetic radiation in the Martian atmosphere. Equivalent particle radii (radius of the particle if it were a sphere) of dust during low and medium dust loading have found to be in the range 1.4-1.7 μm (Haberle et al., 2017, p. 304). An overview of methods used to determine the optical properties of these constituents is given at the end of this chapter in Table 2.2.

Table 2.1: Table from Haberle et al. (2017, p. 57). Abundance of gaseous constituents is presented, ozone and water vapor vary greatly with location and season.

Gaseous species	Average abundance
CO_2	0.9532
N_2	0.027 / 0.019
Ar	0.016 / 0.019
O_2	0.0014
CO	800 ppm
H_2O	15-1500 ppm
H_2	15 ppm
Ne	2.5 ppm
Kr	0.3 ppm
Xe	0.08 ppm
O_3	10-350 ppb
H_2O_2	10-40 ppb
CH_4	0-40 / 0.7-7 ppb

2.4. CO_2 gas - Rayleigh scattering

Since CO_2 molecules are much smaller than visible wavelengths, Rayleigh scattering is applicable. All theory and equations from this section are from Hansen and Travis (1974) Section 2.2. The situation is modelled by small points (particles) that oscillate due to a dipole moment in an electric field (caused by the electromagnetic radiation). Isotropic polarizability of a particle means that the dipole moment and the applied electric field are in the same direction. Particles in the real world are usually not isotropic, this has to be corrected for with a depolarization factor, δ (Hansen and Travis, 1974). For CO_2 gas, $\delta = 0.09$. The scattering matrix is calculated with

$$P(\theta) = \Delta \begin{bmatrix} \frac{3}{4}(1+cos^2\,\theta) & -\frac{3}{4}\,sin^2\,\theta & 0 & 0 \\ -\frac{3}{4}\,sin^2\,\theta & \frac{3}{4}(1+cos^2\,\theta) & 0 & 0 \\ 0 & 0 & \frac{3}{2}\,cos\,\theta & 0 \\ 0 & 0 & 0 & \Delta'\,\frac{3}{2}\,cos\,\theta \end{bmatrix} + (1-\Delta) \begin{bmatrix} 1 & 0 & 0 & 0 \\ 0 & 0 & 0 & 0 \\ 0 & 0 & 0 & 0 \\ 0 & 0 & 0 & 0 \end{bmatrix}, \tag{2.19}$$

where

$$\Delta = \frac{1-\delta}{1+\delta/2}$$
$$\Delta' = \frac{1-2\delta}{1\delta}\,. \tag{2.20}$$

There is a slight wavelength dependence of the scattering matrix through δ, but it has not been measured well. This dependence is not taken into account in this research. The CO_2 gas scattering matrix elements are shown in Figure 2.6 (along with the dust scattering matrix elements).

CO_2 gas shows very small absorption at visible wavelengths, therefore the single scattering albedo can simply be taken as 1. The optical thickness of the CO_2 gas depends on the number of particles (through pressure and temperature) and the wavelength. Since the single scattering albedo is taken as 1.0, only τ_{sca} from Equation 2.11 has to be considered:

$$\tau_{sca}(\lambda) = N_{gas} C_{sca}(\lambda)\,. \tag{2.21}$$

N_{gas} is the gas column number density (m^{-3}) and describes the dependence on the number of particles

$$N_{gas} = \frac{P_{bottom} - P_{top}}{m_{gas} g} \,. \tag{2.22}$$

Here P_{top} and P_{bottom} are the pressure in Pa at the top and bottom of a layer, respectively, m_{gas} is the molecular mass value in kg and g is the gravitational acceleration value in m/s^2.

The wavelength dependence of $\tau_{sca}(\lambda)$ is due to the scattering cross-section, $C_{sca}(\lambda)$:

$$C_{sca}(\lambda) = \frac{24\,\pi^3}{N_L^2} \frac{(n_r^2 - 1)^2}{(n_r^2 + 2)^2} \frac{(6 + 3\delta)}{(6 - 7\delta)} \frac{1}{\lambda^4} \,, \tag{2.23}$$

here n_r is the real refractive index, N_L is Loschmidt's number (2.54743 $\cdot 10^{25}$ m^{-3}) and δ is the depolarization factor mentioned earlier in this section. In reality n_r shows a wavelength dependence but across the visible spectrum this variation is very small, therefore in this study $n_r = 1.00045$ is taken for CO_2 gas. Using a pressure profile, optical thicknesses for an arbitrary number of layers can be calculated with Equations 2.21-2.23.

2.5. Martian dust

The scattering matrix elements of the Martian dust are from the Amsterdam-Granada light scattering database (Muñoz et al., 2012). The data was experimentally determined by Laan et al. (2009). P is plotted in Figure 2.6 next to the CO_2 gas scattering matrix elements. The dust phase function (P_{11}) shows strong forward-scattering behaviour and a weak linear polarization signal (P_{12}) compared to the CO_2 gas.

Optical thickness and single scattering albedo for the Martian dust are based on findings by Smith et al. (2013). This study used CRISM limb observations and a radiative transfer model (accounting for the slanted observation geometry) to derive vertical profiles of dust opacity. The output is presented as 18-layer plots of mixing ratios. The mixing ratio represents the ratio of the dust mass in a layer relative to the total mass in that layer. In this way they remove the dependency on pressure, which allows them for easier representation. They have constructed vertical distributions for a number of sols (Martian days) throughout the Martian year. Two of such mixing ratio profiles are shown in Figure 2.7 from Smith et al. (2013). The dust mixing ratios are transformed to a total dust optical thickness with

$$\tau(\lambda) = \sum_{i=1}^{layers} n_i \, Q_{ext}(\lambda) \, \Delta p_i / p_{surf} \,. \tag{2.24}$$

All quantities in Equation 2.24 are dimensionless. The mixing ratio is represented by n_i, $\Delta p_i / p_{surf}$ is the ratio of the layer pressure and the surface pressure and $Q_{ext}(\lambda)$ is the extinction coefficient. Through $Q_{ext}(\lambda)$, the dependency of the optical thickness on the wavelength is expressed. Values for $Q_{ext}(\lambda)$ across the considered spectrum are presented in Figure 2.8 from Smith et al. (2013). The figure also shows the dust single scattering albedo $a_{dust}(\lambda)$ which they call $\tilde{\omega}_0$ (along with data for water ice). Instead of calculating the total atmospheric optical thickness, each part of the sum can be taken as the optical thickness of a layer. With this strategy, dust loading for a set of scenarios can be simulated by inserting pressure distributions into Equation 2.24 of an arbitrary number of layers and taking mixing ratios (from Figures by Smith et al. (2013) such as 2.7) at appropriate heights. The sum of Equation 2.24 is compared with Figure 2.9 from Montabone et al. (2011) to assure the values for total optical thickness are not greatly underestimated or overestimated. The figure shows total atmospheric optical thickness in the visible spectrum at the Meridiani Planum region (low latitude) for five data sets. Infrared observations have been converted into equivalent values in the visible spectrum. According to Smith et al. (2013), the vertical spread of the Martian dust shows a seasonal dependency: "Dust typically extends to higher altitudes (40–50km) during the perihelion season than during the aphelion season (<20km)."

From Figure 2.8 values for the single scattering albedo, a, at wavelengths 0.4, 0.6 and 0.8 μm are taken as: $a_{0.4} = 0.81$, $a_{0.6} = 0.92$ and $a_{0.8} = 0.97$.

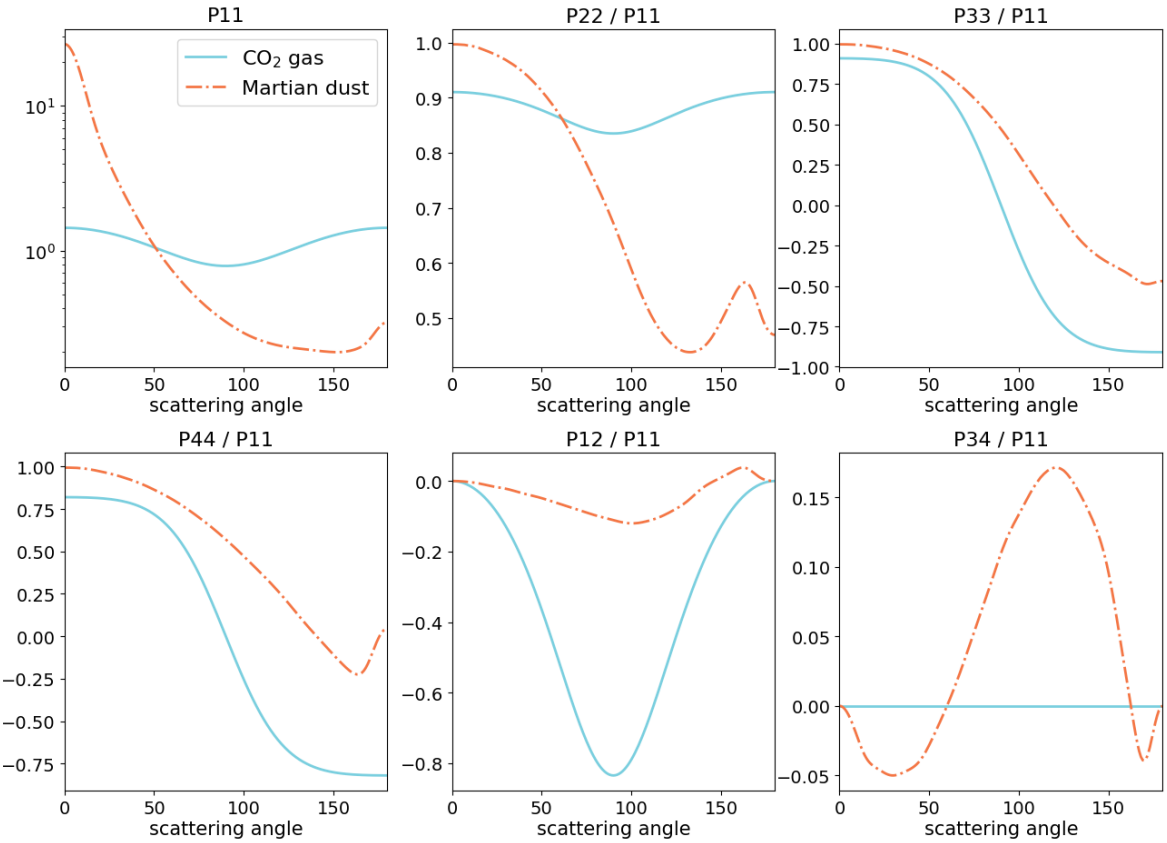

Figure 2.6: Scattering matrix elements of CO_2 gas and Martian dust. The near isotropic scattering behaviour of Rayleigh scattering is visible in the phase function (P_{11}) of the CO_2 gas. In contrast, the Martian dust phase function exhibits very strong forward scattering. Elements P_{22}, P_{33}, P_{44}, P_{12} and P_{34} are normalized by P_{11}. Element P_{12} represents the single scattering degree of linear polarization. For CO_2 gas the well-known Rayleigh linear polarization pattern is visible in P_{12}. This pattern results in the single scattering Rayleigh sky in an atmosphere dominated by gas scattering with little multiple scattering, see Figures 4.14 and 4.15 for a visual of this pattern in the sky. The pattern is used for validation of the code, detailed in Section 4.6. Ten elements of the scattering matrices are not plotted, two of these are not independent ($P_{21} = P_{12}$ and $P_{43} = P_{34}$) and eight are zero (P_{13}, P_{14}, P_{23}, P_{24}, P_{31}, P_{32}, P_{41} and P_{42}, see Equation 2.14).

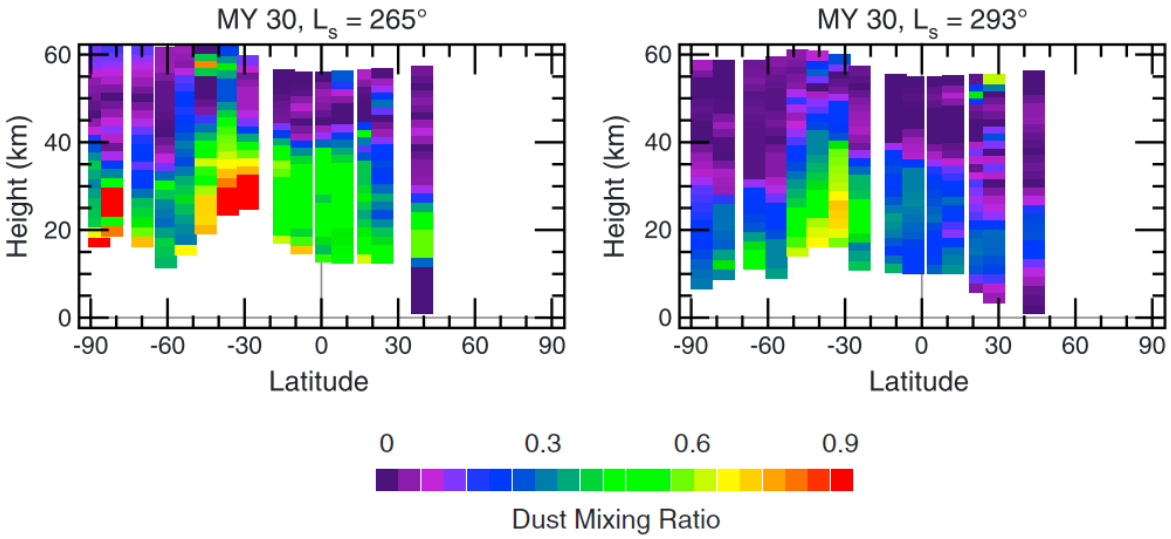

Figure 2.7: Figure from Smith et al. (2013) showing the vertical distribution of dust in terms of mixing ratios, n_i. Optical thicknesses have been calculated from mixing ratio profiles with Equation 2.24. The observations were done by the CRISM instrument on board the Mars Reconnaissance Orbiter.

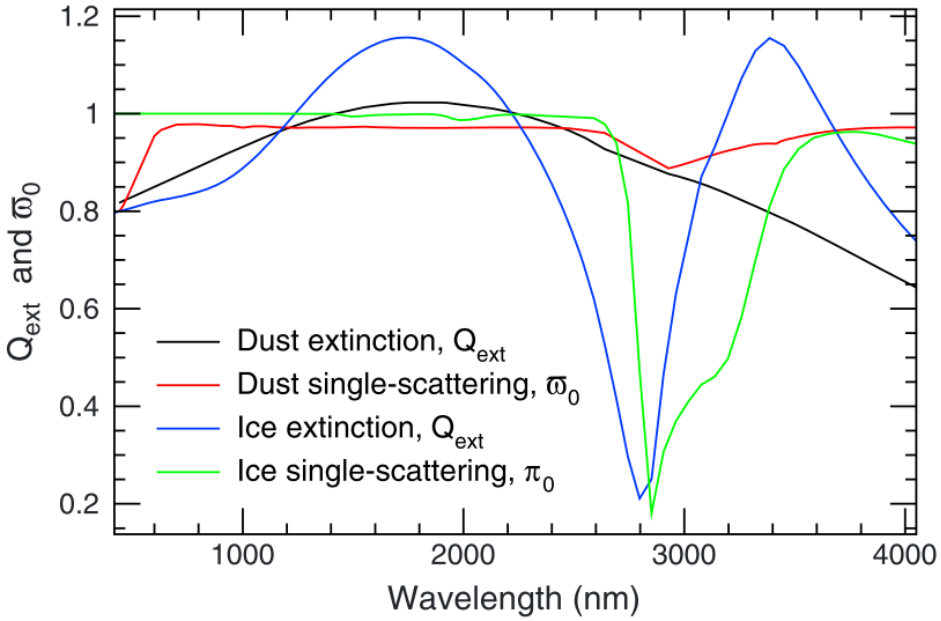

Figure 2.8: Extinction coefficient Q_{ext} and single- scattering albedo $\tilde{\omega}_0$ (a_{dust} in this research) for dust (water ice also given) in part of the visible and near infrared. Leftmost values are at 400 nm. Unlike for CO_2 gas, absorption by Martian dust is not negligible and is therefore taken into account in the code. Values for a at wavelengths 0.4, 0.6 and 0.8 μm are taken as: $a_{0.4} = 0.81$, $a_{0.6} = 0.92$ and $a_{0.8} = 0.97$. Figure is taken from Smith et al. (2013).

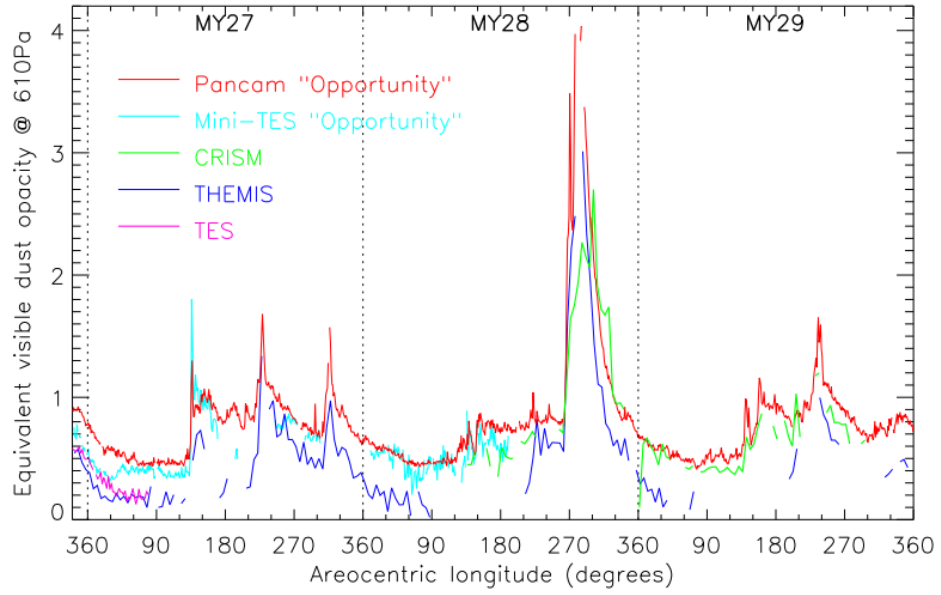

Figure 2.9: Figure from Montabone et al. (2011). Total dust optical thickness (vertical) of the atmosphere from five data sets at Meridiani Planum on Mars. Infrared observations were converted to their visible equivalent.

2.6. Combining multiple constituents in one layer

A model of the Martian atmosphere is implemented in the code by defining homogeneous shell layers. In general, a certain layer will have multiple atmospheric constituents. Scattering by this mix of particles can be simulated by combining their relevant scattering matrices weighted by their optical thicknesses. The contribution of each of these constituents to the scattering and absorption in a layer is weighted by the scattering and absorption coefficients. The optical thickness, single scattering albedos and the scattering matrix for a combination of atmospheric constituents are calculated in the following ways:

$$P_{layer}(\theta,\lambda) = \frac{\tau^m_{sca}(\lambda)P^m(\theta,\lambda) + \tau^a_{sca}(\lambda)P^a(\theta,\lambda)}{\tau^m_{sca}(\lambda) + \tau^a_{sca}(\lambda)} , \tag{2.25}$$

$$a_{layer}(\lambda) = \frac{\tau^m_{sca}(\lambda) + \tau^a_{sca}(\lambda)}{\tau^m_{sca}(\lambda) + \tau^m_{abs}(\lambda) + \tau^a_{sca}(\lambda) + \tau^a_{abs}(\lambda)} , \tag{2.26}$$

$$\tau_{layer}(\lambda) = \tau^m_{sca}(\lambda) + \tau^m_{abs}(\lambda) + \tau^a_{sca}(\lambda) + \tau^a_{abs}(\lambda) . \tag{2.27}$$

The superscripts in the above equations refer to molecule and aerosol. In the PA3S code, these are CO_2 gas and dust, respectively. A cloud in the code is simulated as a region that breaks the homogeneity of a layer. In that region, the optical properties of the cloud particles are also included when calculating the combined optical properties (of the cloud region) with Equations 2.26-2.27.

An overview of the methods used in this research to determine the relevant optical properties of the main constituents is given in Table 2.2. The cloud CO_2 ice properties are also mentioned for completion, even though the methods are described in Chapter 3.

Table 2.2: Overview of the methods used to determine the optical properties of the relevant constituents of the Martian atmosphere. Properties of the cloud CO_2 ice particles are also mentioned, these will be discussed in Chapter 3. ADDA is a software package that is also detailed in Chapter 3. The numbered subscripts in the dust single scattering albedo refer to the respective wavelengths: 0.4, 0.6 and 0.8 μm.

constituent	τ	P	a
CO_2 gas	Equations 2.21-2.23	Rayleigh scattering, Equation 2.19	1.0
dust	Equation 2.24	experiments by Laan et al. (2009)	$a_{0.4}$=0.81, $a_{0.6}$=0.92, $a_{0.8}$=0.97, Figure 2.8 by Smith et al. (2013)
cloud CO_2 ice	0.01-0.6, analysis by Määttänen et al. (2010)	calculated with ADDA	1.0, derived with ADDA

3

Calculating cloud particle scattering matrices with ADDA

The shapes and sizes of the CO_2 ice crystals that constitute the Martian mesospheric clouds are not known. Several size distributions are suspected from previous studies, see Table 1.1 in Chapter 1. In this research, we decided to calculate the scattering matrices (P) and scattering and absorption cross-sections (C_{sca} and C_{abs}) with the software package ADDA. This was done for a set of size parameters ($x = 2\pi\, r_{eq}/\lambda$) corresponding to the size distribution found by Määttänen et al. (2010) and the three considered wavelengths: 0.4, 0.6 and 0.8 μm. Subsequently, the scattering matrix (P_{SD}) for particles distributed in size according to a size distribution was calculated, for each wavelength.

ADDA (Yurkin and Hoekstra, 2011) has been developed by Dr. A. G. Hoekstra and colleagues at the University of Amsterdam and is an implementation of the Discrete Dipole Approximation method (Draine and Flatau, 1994). Both ADDA and DDA simulate scattering by 3D objects of various shapes by approximating the objects with a finite amount of dipoles. A brief overview of the ADDA software and its main input parameters is given in Section 3.1. Next, the importance of using a sufficient number of dipoles for convergence is detailed in Section 3.2. Normalization of the scattering matrix is discussed in Section 3.3. For validation of proper use of the software, ADDA results for a sphere are compared with results of a Mie code in Section 3.4. The refraction index of the material is required input, picking adequate values is detailed in Section 3.5. Subsequently, combining ADDA results to create scattering matrices of size distributions is considered in Section 3.6. Two out of the three suspected crystal shapes mentioned in Subsection 1.1 were not readily available in ADDA, generating these shapes is discussed briefly in Section 3.7. In Section 3.8, results are given and discussed for cubes, octahedra and cube-octahedra shapes. Finally, a comparison of results for a size distribution of cubes with results of a size distribution of spheres is performed in Section 3.9. This comparison is of interest because Mie scattering is often assumed in literature concerning the mesospheric clouds.

3.1. Overview of software and main parameters

The ADDA software has many options but only the most important features used in this research are discussed in this section. The purpose of ADDA is to calculate P, C_{sca} and C_{abs} in situations where Rayleigh scattering (small size parameter) and Mie scattering (homogeneous spheres) are not applicable. In ADDA, a particle shape is defined within a 3D computational grid containing an adjustable number of boxes (grid size). A shape is created by putting dipoles in certain boxes while leaving others empty, see Figure 3.1 (Yurkin and Hoekstra, 2011) for a 2D projection. In this way, various finite shapes can be approximated, a shape needs a certain number of dipoles to be accurately approximated. The accuracy of ADDA results in terms of grid size is further considered in Section 3.2.

A few built-in shapes are readily available, among these is the box shape (a 3D cube). The particle size parameter ($x = 2\pi\, r_{eq}/\lambda$, with r_{eq} the radius of a particle if its volume were contained in a sphere) is adjustable by manipulating the number of dipoles and the incoming wavelength. The most straightforward way to do this is by giving the grid size and the wavelength as input through the command

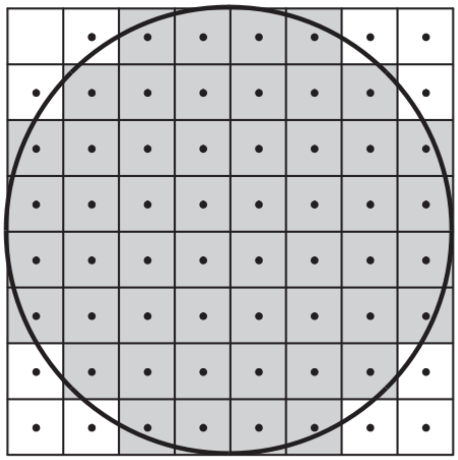

Figure 3.1: Figure from Yurkin and Hoekstra (2011) schematically showing the computational grid. In this 2D projection of the grid, a sphere is approximated with boxes containing dipoles, boxes with dipoles are gray, void boxes are white.

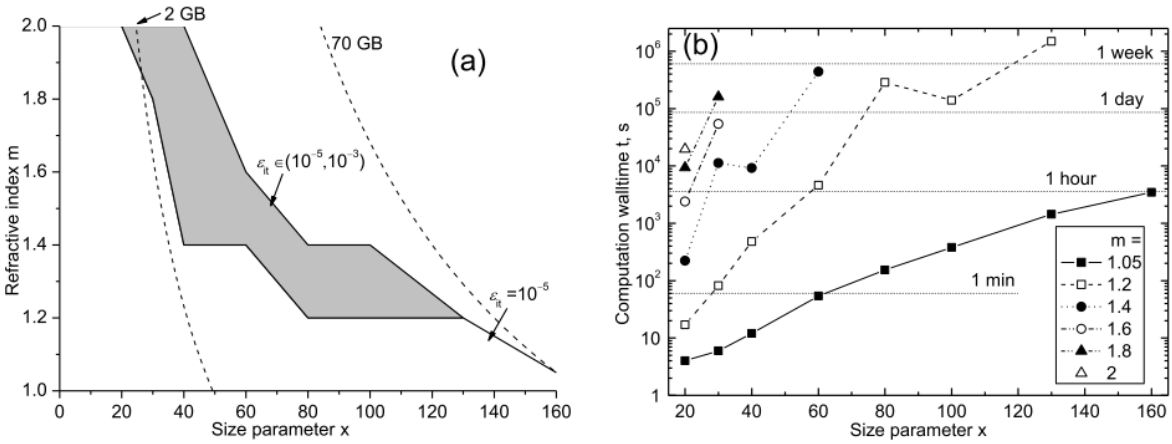

Figure 3.2: Figure from Yurkin and Hoekstra (2014) showing the applicability of ADDA for spheres of different size parameter x and refractive index m. (a) The gray region signifies a region of incomplete convergence, lower left region is complete convergence, dashed lines represent memory requirements. The simulations we ran were done for fifteen x values ranging uniformly between 7.8 and 47.3 with $m = 1.41$ (justified in Section 3.5) for nearly all runs, mostly fitting well within the convergence region. To assure convergence for simulations with size parameters 42.3 and 47.3 a slightly lower m was taken: 1.38. (b) Approximate total walltime (elapsed real time) for different combinations of x and m using 64 processors. The simulations we performed for $m \approx 1.4$ (black dots) matched quite well with the estimates in this figure.

line. There are other combinations of inputs to setup the simulations, for more information the reader is referred to the ADDA manual (Yurkin and Hoekstra, 2014). One of the most important features is the ability to integrate the results over all possible orientations of the particle. Theoretically, arbitrarily large size parameters are possible, but these will result in computational times that are unpractical and will have a higher chance of not converging. See Figure 3.2 from Yurkin and Hoekstra (2014), where the convergence region and computation times are presented in terms of the size parameter, x, and the refractive index, n (m in the figure).

3.2. Accuracy and grid size

A sufficient number of dipoles is required to accurately calculate the scattering matrix of any shape. The effect of grid size on convergence is not the same for every shape. For instance, approximating the shape of a sphere with a grid of cubes is more difficult than approximating a cube. See Figure 3.3, where a sphere approximated with a grid-size of 20×20×20 has been presented. It is required to check for the shape you are using whether or not the results have converged. A too large grid size is also not desirable because of long computation times. According to the ADDA manual (Yurkin and Hoekstra,

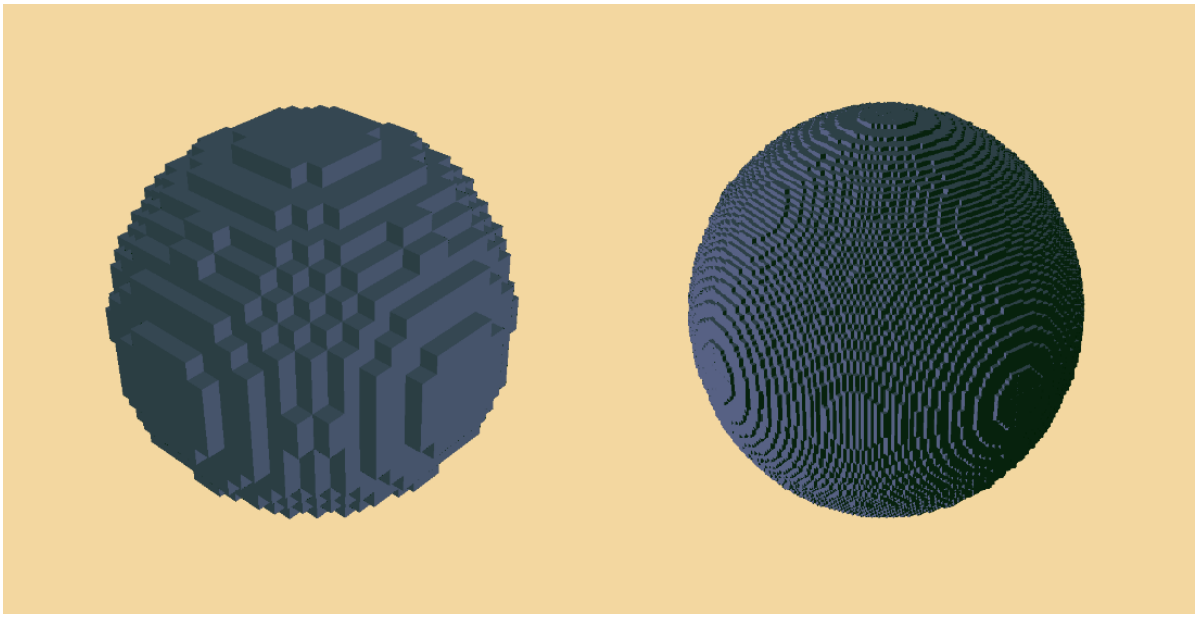

Figure 3.3: Approximation of a sphere with boxes containing dipoles, left plot is for grid size $20 \times 20 \times 20$, right plot for $100 \times 100 \times 100$. Larger grid sizes approximate the shape more accurately. Figure generated with LiteBil software developed at the Laboratory of Paper Coating and Converting at Åbo Akademi University (Laboratory of Paper Coating and Converting at Åbo Akademi University).

2014), a good rule of thumb to assure convergence is to choose a grid size in such a way that the amount of dipoles per wavelength is equal to or larger than 10. For the cubes, this notion was tested for smaller size parameters (shorter simulation times) by increasing the grid size until convergence while tracking the number of dipoles per wavelength. In the ADDA manual it is also stated that the rule of thumb is applicable to size parameters $x > 10$. For the octahedral and cube-octahedral crystal shapes it was not possible to keep the number of dipoles per wavelength at 10. This was because the grid size was constrained by the CAD models used for creation of the shape files (see Section 3.7). The number of dipoles a light wave "sees" will be comparatively low, sharp edges of the particle will not be well represented and errors will be introduced, causing the results to be more akin to those of smoother shapes, like spheres or ellipsoids.

3.3. ADDA conventions and normalization of the scattering matrix

The output of ADDA is not readily applicable as scattering matrix P (Equation 2.15 from Chapter 2) for application in the PA3S code. The ADDA manual (Yurkin and Hoekstra, 2014) states that multiplication by k^2 (the free wave number $k = 2\pi/\lambda$) converts ADDA output into the Stokes phase matrix (Z). Multiplying again by $4\pi/C_{sca}$ (total multiplier $\lambda^2/\pi/C_{sca}$) results in the normalized Stokes scattering matrix, in the research denoted by P. However, this approach is sensitive to C_{sca} which is also ADDA output. There is a more robust way of normalizing ADDA output. Scattering matrix P input into PA3S code should conform to the following normalization (based on Hansen and Travis, 1974):

$$\int_{4\pi} P_{11} \frac{d\Omega}{4\pi} = 1 \,. \tag{2.13}$$

When the phase function is integrated over the entire solid angle, the result should equal 1. The approach is to simply perform this integration and divide the ADDA scattering matrix output (P^{ADDA}) by the result

$$P = \frac{P^{ADDA}}{\frac{1}{2}\int_0^{\pi} P_{11}^{ADDA}\, sin\,\theta\, d\theta} \,. \tag{3.1}$$

This normalization has been applied to all ADDA results before the comparison with Mie code in Section 3.4 and before using the matrices as input into the PA3S program.

ADDA uses a $exp(-\omega t)$ convention for the time dependent part of the harmonic electric field in their derivations, the same convention is used in the work of Mishchenko (for details see e.g. (Mischenko et al., 2000)). Care should be taken when comparing or concurrently using results acquired with methods that use $exp(+\omega t)$ (e.g. methods based on Hansen and Travis (1974) or Hulst (1981). The P_{34} and P_{43} elements can be of opposite sign. It was made sure that all scattering matrices were in the ADDA/Mishchenko convention before input into PA3S

3.4. Comparison with Mie code

Several benchmark studies for ADDA have been published, see for example (Yurkin et al., 2007), (Ayranci et al., 2007) and (Penttilä et al., 2007). For validation of proper use of the software, ADDA output for a sphere has been compared to results from Mie computations using a well-tested code based on De Rooij and Van der Stap (1984). Both results are shown in Figure 3.4. ADDA results were generated with a grid size of $16 \times 16 \times 16$ and both sets of results were for a size parameter of $x = 4.7$ with real refractive index $n_r = 1.33$ (imaginary part of refractive index was set to zero). The results match very well after normalization of the ADDA output over the full solid angle as described in Section 3.3. Note in Figure 3.4 how the different time factor conventions mentioned in Section 3.3 ($exp(-\omega t)$ by Mishchenko in ADDA vs $exp(+\omega t)$ by van de Hulst in Mie code) result in an opposite sign of P_{34}.

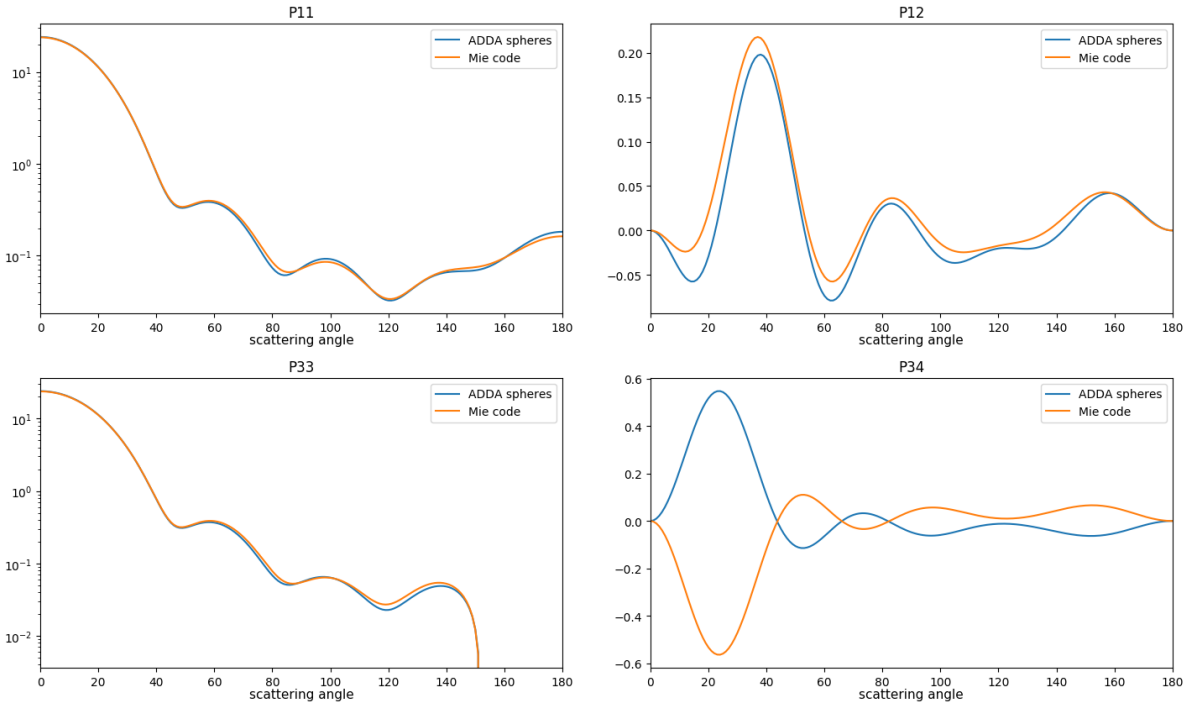

Figure 3.4: Comparison between an ADDA run using spheres and Mie computation based on De Rooij and Van der Stap (1984). The ADDA run was with a $16 \times 16 \times 16$ grid size, both plots are for a size parameter of 4.7 and a real refractive index of 1.33 (imaginary refractive index is zero). These results were used to test for proper use of the ADDA software. The results show a good match, note the opposite sign of P_{34} caused by different conventions for the time dependent part of the harmonic electric field, explained in Section 3.3.

3.5. Complex refractive index of CO2 ice

The real and imaginary parts (n_r and n_i) of the complex refractive index (n) of CO_2 ice are necessary input for the ADDA simulations. In general, the refractive index exhibits a dependence on the wavelength and the temperature. Nevertheless, a high resolution profile of the refractive index in the visible spectrum is not necessary. This is because this research is concerned with simulating scattering by cloud particles of which the exact morphology and optical properties are still uncertain, not with the interpretation of actual measurements.

This whole section is based on Warren (1986) who reviewed several experiments measuring the complex refractive index of clear CO2 ice in several parts of the electromagnetic spectrum. Warren states that the temperature of atmospheric Martian CO2 ice is probably around 150 K and therefore his review focuses on experiments at similar temperatures. According to Schulze and Abe (1980), the real refractive index is relatively independent of the temperature at temperatures above 75 K. This indicates that measurements at lower temperatures compiled by Warren are valid results for application in the 150 K situation.

In the left plot in Figure 3.5 from Warren (1986), the measurements have been summarized. It is clear that there is a wide range in measurement results probably caused by conducting the experiments at different temperatures and the presence of measurement uncertainties. The measurements by Seiber et al. (1971), Tempelmeyer and Mills (1968) and Egan and Spagnolo (1969) cover a wide enough range of the visible spectrum. Measurements by Egan and Spagnolo (1969) give constant n_r over the visible spectrum but with a large measurement uncertainty. Results by Tempelmeyer and Mills and Seiber et al. both show n_r decreasing with increasing wavelength, but with different steepness. The measurements by Seiber et al. were performed at a slightly higher temperature than those by Tempelmeyer and Mills.

In this research we used $n_r = 1.41$. ADDA is sensitive in terms of convergence and computation time to the refractive index and size parameter as shown in Figure 3.2. For a few combinations of size parameter and refractive index the settings entered the non-convergence zone in Figure 3.2. For these runs the refractive index was set to $n_r = 1.38$ to stay clear from the non-convergence zone. This choice is based on the measurements by Seiber et al. (1971) at 82 K and $\lambda = 0.6$ μm, even though Egan and Spagnolo (1969) conducted experiments at 195 K, closer to the suggested 150 K of Martian atmospheric CO2 ice. This is motivated by the large measurement uncertainty (± 0.05) in the Egan and Spagnolo data.

The value of n_r is assumed to be constant in the visible spectrum, despite the fact that the data generated by Seiber et al. is clearly not constant across the visible spectrum. However, based on the required accuracy in this research, such an assumption is deemed appropriate. This decision is also supported by the large spread shown by the experimental data, even at similar temperatures.

Absorption properties of a material are defined by the imaginary part of the complex refractive index (n_i). The right plot in Figure 3.5 shows measurements performed by Egan and Spagnolo (1969) as presented by Warren (1986). From the figure can be concluded that n_i is very small in the visible spectrum. ADDA runs with n_i set to zero and n_i set to values taken from the right plot in Figure 3.5 were compared to check if n_i could be simply set to zero. This was indeed the case, see Figure 3.6 for an example of such a comparison.

The assumption of constant real and imaginary refractive indices in the visible spectrum allows for simplifications when generating the scattering matrix of a size distribution of cloud particles, detailed in Section 3.6: Scattering matrices now only depend on the size parameter x. This means that scattering matrices do not have to be calculated separately for every wavelength but simply for a set of different x (spanning at least the range of the distribution), scattering matrices of intermediate values of x can subsequently be generated with interpolation. Assuming the size distribution derived by Määttänen et al. (2010) with cloud particle equivalent radii of 1-3 μm, results in the minimum and maximum x-values shown in Table 3.1 for the three considered wavelengths.

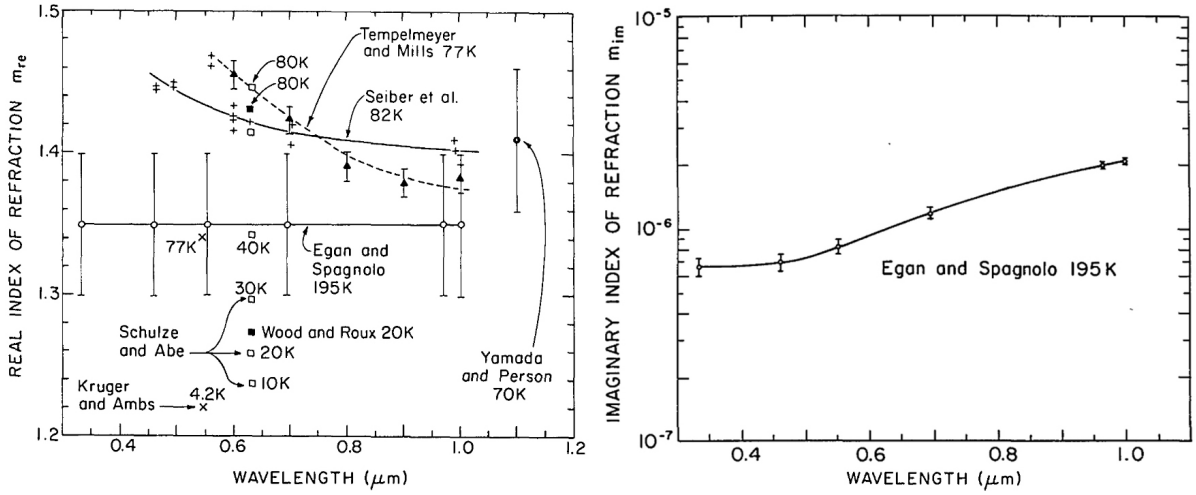

Figure 3.5: Left: Measurements of the real refractive index of CO_2 ice at visible wavelengths from several studies compiled by Warren (1986). Right: Measurements of the imaginary refractive index of CO_2 ice at visible wavelengths found by Egan and Spagnolo (1969), figure is presented in Warren (1986).

Table 3.1: Minimum and maximum size parameters $x = 2\pi\, r_{eq}/\lambda$ for the three considered wavelengths assuming the real and imaginary refractive index are constant in the visible spectrum, with a range of r_{eq} (1-3 μm) based on analysis by Määttänen et al. (2010).

wavelength	x_{min}	x_{max}
0.4 μm	15.7	47.3
0.6 μm	10.5	31.4
0.8 μm	7.8	23.6

3.6. Scattering matrices of size distributions

In general, particle sizes vary according to a size distribution. A scattering matrix of a size distribution is generally much smoother than the scattering matrix of a single particle size. With a size distribution, many notable features (peaks and valleys) of the scattering matrix are evened out. These could otherwise cause very distinct signals in flux or degree of polarization simulated with the PA3S code. There is no reason to assume the mesospheric cloud particles are of a single size. Analysis of OMEGA observations onboard Mars Express by Määttänen et al. (2010) indicates that the particle sizes form a size distribution with effective radii between 1 and 3 μm and median values of 2.0-2.3 μm. Their analysis was performed under the assumption that the particles where homogeneous spheres.

The procedure for generating the scattering matrix of the size distribution (from now on indicated by P_{SD}) consists of several steps which will be explained in this section. Summarized these are:

1) Assume a size distribution based on minimum and maximum particle radii from literature.

2) Determine the Gauss-Legendre weights w_{xi} and abscissae x_i in the interval [-1,1] to some degree N, which is the number of weights and abscissae in the interval.

3) Map w_{xi} and x_i to their relevant counterparts w_{ri} and r_i in size interval $[r_{min}, r_{max}]$ found in literature, find the number of particles $n(r_i)$ at each r_i.

4) Use ADDA to calculate the scattering matrices P^{ADDA} and the scattering cross-sections C_{sca}^{ADDA} for a reasonable number of size parameters (enough to capture the size distribution) (C_{abs}^{ADDA} were all zero because the imaginary refractive index was set to zero, justified in Section 3.5).

5) Use linear interpolation between P^{ADDA} and C_{sca}^{ADDA} from step 2 to find their respective interpolant functions. From these two interpolant functions sample the scattering matrices P_i and corresponding $C_{sca,i}$ at size parameters $2\pi\, r_i/\lambda$. Do this for every wavelength of interest by taking appropriate minimum and maximum values of the size parameters, see Table 3.1.

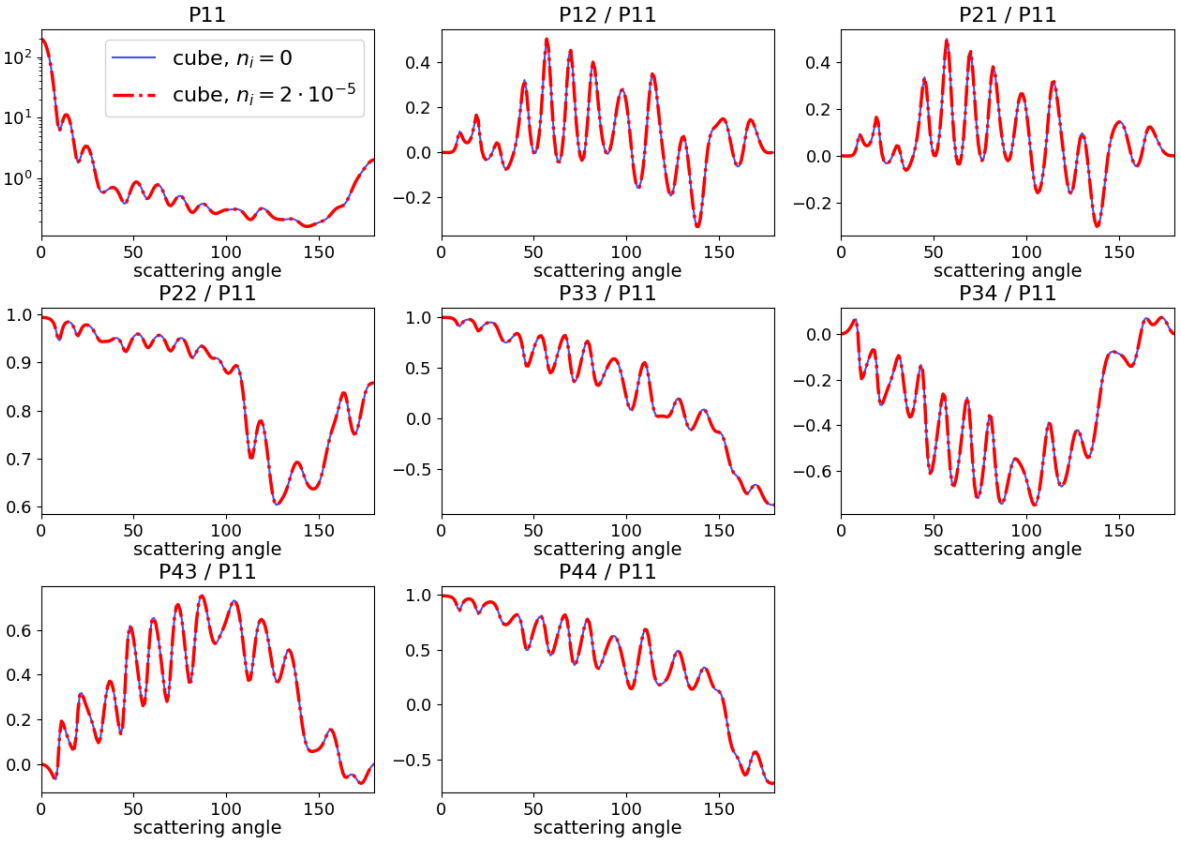

Figure 3.6: Comparison of ADDA runs for cubes, $x = 17.5$, with n_i set to zero and with a small n_i corresponding roughly to the value ($2 \cdot 10^{-5}$) measured at a wavelength of 1 µm by Egan and Spagnolo (1969), see the left plot in Figure 3.5. The two sets of plots completely overlap, this indicated that n_i could be set to zero in the visible spectrum.

6) Combine the matrices P_i, resulting in matrix P_{SD} of the size distribution for a certain wavelength.

Equations step 1
For particle size distributions usually a log-normal distribution is assumed. This is also the case in this research. From De Rooij and Van der Stap (1984) the log-normal distribution is

$$n(r) = \frac{1}{r\ ln\,\sigma\sqrt{2\pi}}\ exp\left[-\frac{1}{2}\left(\frac{ln\,r - ln\,r_g}{ln\,\sigma_g}\right)^2\right], \tag{3.2}$$

where r_g is the distribution median and σ_g is the geometric standard deviation. The σ_g of a set of numbers $\{x_1, x_2, \ldots, x_n\}$ is calculated with

$$\sigma_g = exp\left(\sqrt{\frac{\sum_{i=1}^{n}\left(ln\,x_i / \mu_g\right)^2}{n}}\right), \tag{3.3}$$

where μ_g, the geometric mean is

$$\mu_g = \sqrt[n]{x_1\,x_2 \ldots x_n}\,. \tag{3.4}$$

Equation step 2
Now, $n(r)dr$ is the number of particles with radius r to $r + \Delta r$. The size distribution is integrated with

Gauss-Legendre quadrature. First, in the interval [-1, 1] the abscissae x_i and weights w_{xi} were found with the numpy function "leggaus". On the [-1, 1] interval it holds that

$$\int_{-1}^{1} f(x)\,dx \approx \sum_{i=1}^{N} w_i f(x_i)\,, \tag{3.5}$$

where the degree N is the number of abscissae and weights in the interval.

Equations step 3
Next, the abscissae and weights were mapped to the interval of effective radii found by Määttänen et al. (2010) using

$$r_i = \frac{1}{2}(x_i + 1)(r_{max} - r_{min}) + r_{min}\,, \tag{3.6}$$

$$w_{ri} = \frac{1}{2} w_{xi}(r_{max} - r_{min})\,, \tag{3.7}$$

Steps 4 and 5
Scattering matrices P^{ADDA} were generated with ADDA for enough size parameters in the size distribution to capture the shape of the distribution. Because the real refractive index was assumed to be constant across the visible spectrum and the imaginary refractive index was assumed to be zero across the visible spectrum (see Section 3.5), scattering matrices, P_i, only change with the size parameter. This meant that P_i, at size parameters $2\pi\, r_i/\lambda$, could be calculated by finding a linear interpolant of the ADDA scattering matrices P^{ADDA} and evaluating the interpolant function it at each $2\pi\, r_i/\lambda$. $C_{sca,i}$ were calculated in a similar fashion (absorption cross-section results were all zero).

Equation step 6
Finally, P_{SD} was found with

$$P_{SD} = \frac{\sum P_i\, C_{sca,i}\, n(r_i)\, w_{ri}}{\sum C_{sca,i}\, n(r_i)\, w_{ri}}\,. \tag{3.8}$$

3.7. Generating octadrons and cube-octahedrons shapes for ADDA

According to Mangan et al. (2017), the CO_2 ice particles are probably cubes, octahedrons or cube-octahedrons. ADDA has a built-in option for a cubic scatterer, the other two shapes were not readily available. So-called shape-files can be read in by ADDA and these had to be generated. For this purpose a software called PIP (point-in-polyhedron) by Schuh (2007) has been added to the ADDA software-package. This program can convert the commonly used .obj file format (although some other common CAD-file formats are supported as well) into a data format that is usable by ADDA. CAD-files for common polyhedrons are freely available on the internet for non-commercial purposes, in this research they were downloaded from GrabCad (2019). With software called LiteBil, the shape files generated with PIP were visualized to verify that the conversion from .obj format to ADDA shape-file was done correctly. Visualisations of the octahedron and cube-octahedron shape files by LiteBil are presented in Figure 3.7.

3.8. ADDA results

Results for the size distribution scattering matrix elements are given for the cubes, octahedra and cube-octahedra, shapes that have been predicted by Mangan et al. (2017). Scattering matrix elements for size distributions of cubes are presented in Figure 3.8, octahedra in Figure 3.9 and cube-octahedra in Figure 3.10. For each shape, the plots are given for three wavelengths: 0.4, 0.6 and 0.8 μm. See Table 3.1 for the ranges of size parameters for each wavelength.

All three figures show that with increasing size parameter, the scattering matrices become increasingly complex. Since the size parameter is $x = 2\pi\, r_{eq}/\lambda$, this complexity increases when the wavelength

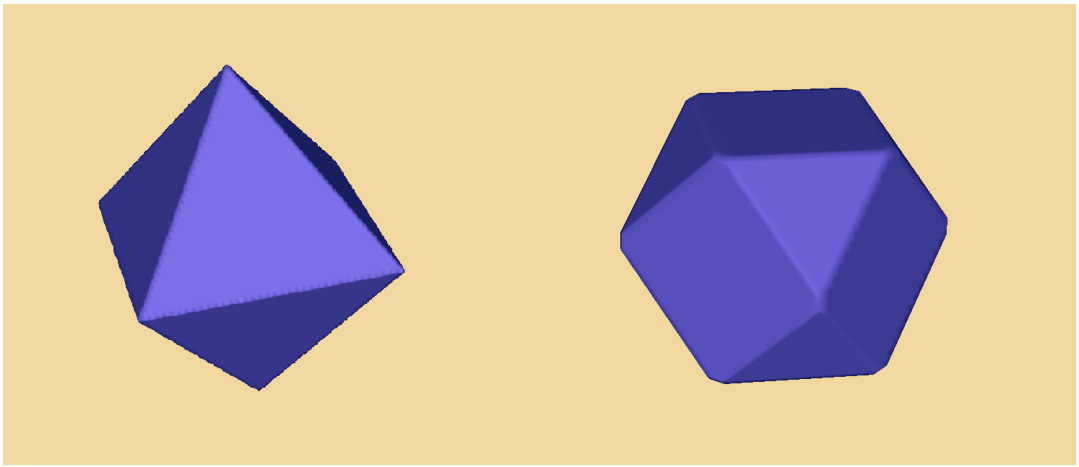

Figure 3.7: Cube-octahedron shape, downloaded shape object file from GrabCad (2019), shape file created with pip and plot generated with LiteBil software (Laboratory of Paper Coating and Converting at Åbo Akademi University).

decreases with respect to the particle size. For all three shapes the scattering matrix elements become smoother with increasing wavelength. For size-distributions of cube-octahedra, the features seen in blue (especially in P_{11}) seem relatively smooth compared to the those seen for the other two shapes in blue. This could be caused by the lower number of dipoles per wavelength (smaller grid sizes) at which these simulations were performed which introduces errors, especially at larger size parameters (smaller wavelengths). A cube-octahedron's sharp edges are not represented correctly and the results start to somewhat resemble those of a sphere. Looking at the single scattering degree of linear polarization (P_{12}) it is clear that distinct patterns are exhibited for each shape and every wavelength. This is in accordance with the notion in literature that the degree of polarization is very useful for determination of particle shape (Hansen and Travis, 1974).

3.9. Comparison of size distributions of cubes and spheres

The results of the cube, octahedron and cube-octahedron size distributions are compared with the same size distribution of spheres (particle sizes between 1 and 3 μm with median of 2.2 μm). This information is useful since Mie codes are more readily available and often much faster. If results for size distributions of cubes, octahedra and cube-octahedra result in scattering matrices that are very similar to those of size distributions of spheres, it would be more practical choice to just use the latter. The comparison over a broad range of scattering angles is of interest because surface-based observations can potentially detect the same cloud from a broad range of scattering angles. For space-based observations this is more difficult; in general, the orbit puts constraints on the viewing geometry and illumination conditions. From Figure 3.11 it is clear that the scattering matrices exhibit roughly the same forward-scattering and back-scattering behaviour in the phase function (P_{11}). This makes sense because this behaviour is mainly dictated by particle sizes (Hansen and Travis, 1974), which are the same for each shape. However, the sphere scattering matrix shows more distinct peaks and valleys for values of θ between roughly 50° and 130°. Moreover, the sphere size distribution P_{12} shows a very sharp negative and positive peak at small scattering angles and a clear valley at high scattering angles. These features are not present for a cube size distribution.

In conclusion, using spheres as constituents of the mesospheric clouds is not appropriate in this research because simulation results of PA3S would show distinct features in the flux and degree of polarization that are probably not present in reality. Such results would be too optimistic. For eventual analysis of real measurements, the approach described in this chapter should be repeated for various size distributions, with variable real and imaginary refractive indices in the visible spectrum and perhaps for combinations of cubes, octahedra and cube-octahedra. Also, experimental measurements under atmospheric conditions similar to the Martian mesosphere could be conducted.

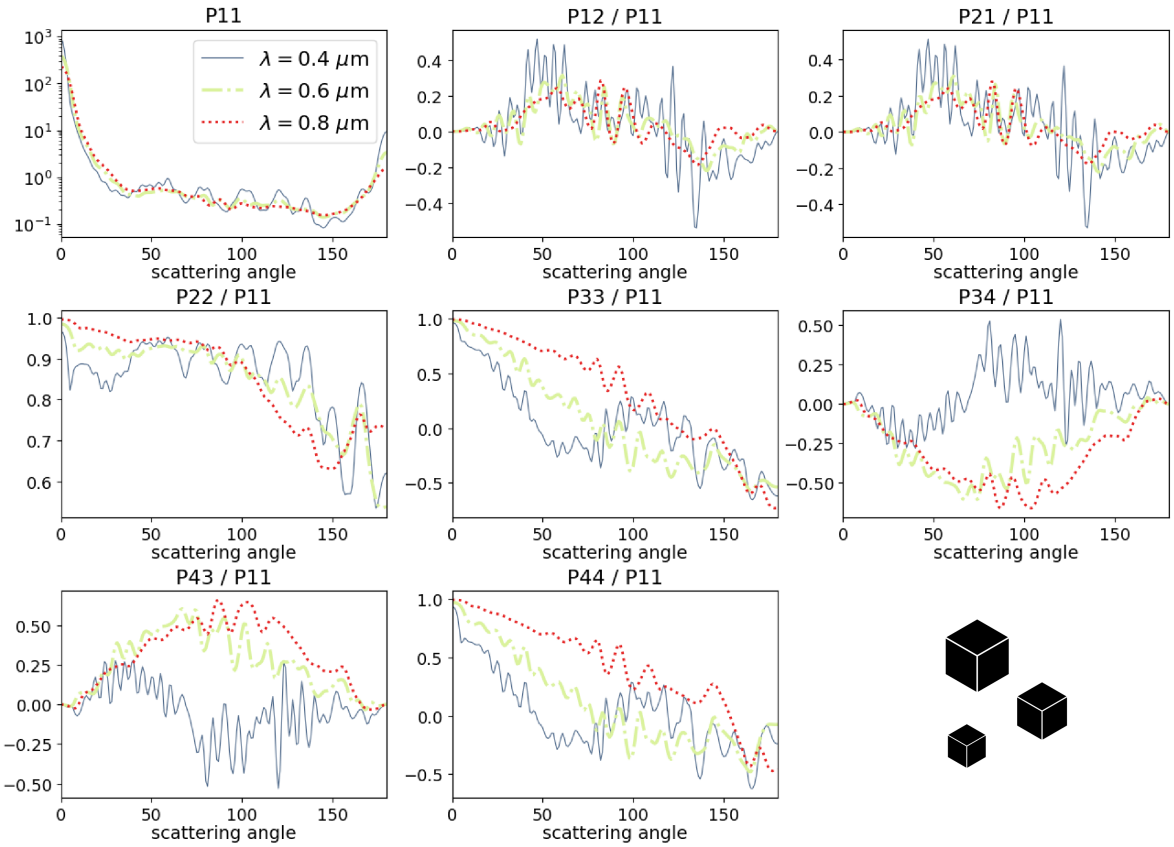

Figure 3.8: Scattering matrix elements for a size distribution of cubes. Results were generated by interpolating between sets of ADDA outputs for cubes calculated at different size parameters and applying Equation 3.8, explained in Section 3.6. Range of equivalent particle radii of the distribution is 1-3 μm. Wavelengths considered are 0.4, 0.6 and 0.8 μm. Corresponding size parameter ranges are 15.7-47.3 (0.4 μm, blue), 10.5-31.4 (0.6 μm, green) and 7.8-23.6 (0.6 μm, red).

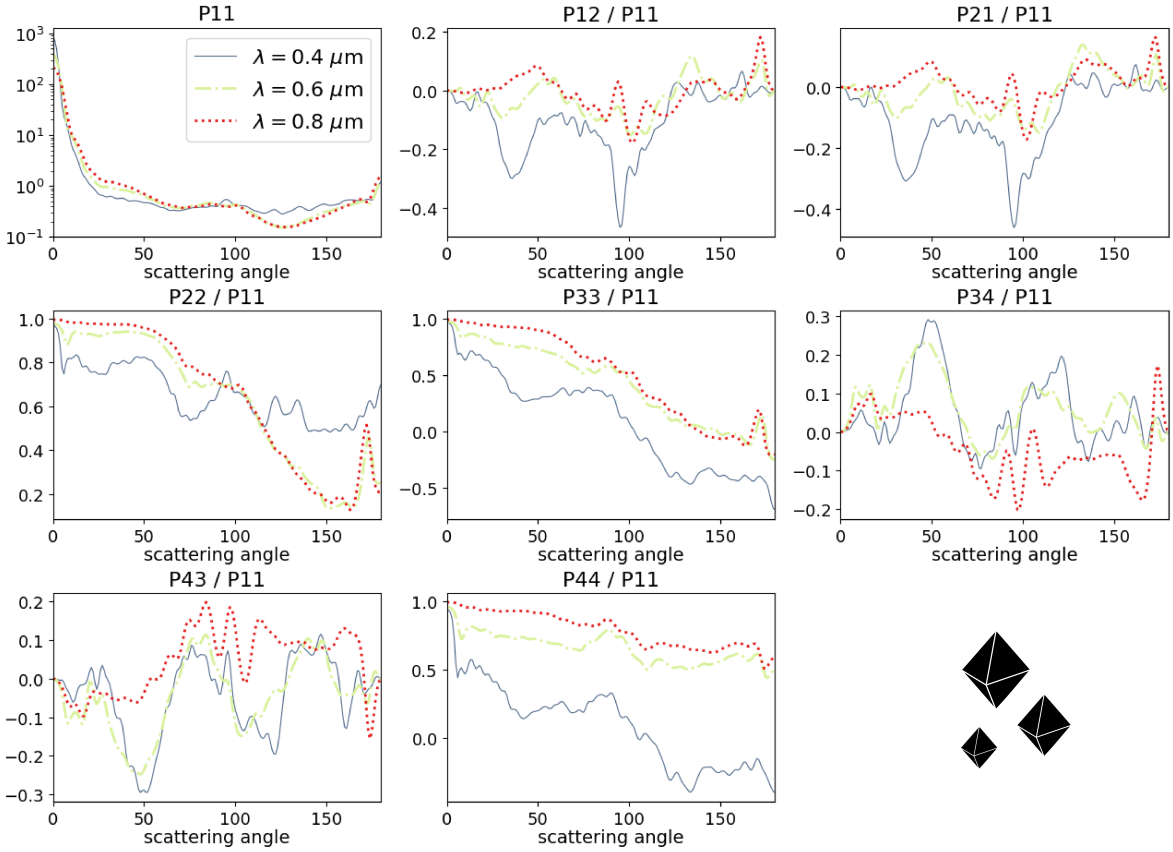

Figure 3.9: Same as Figure 3.8 but for a size distribution of octahedra.

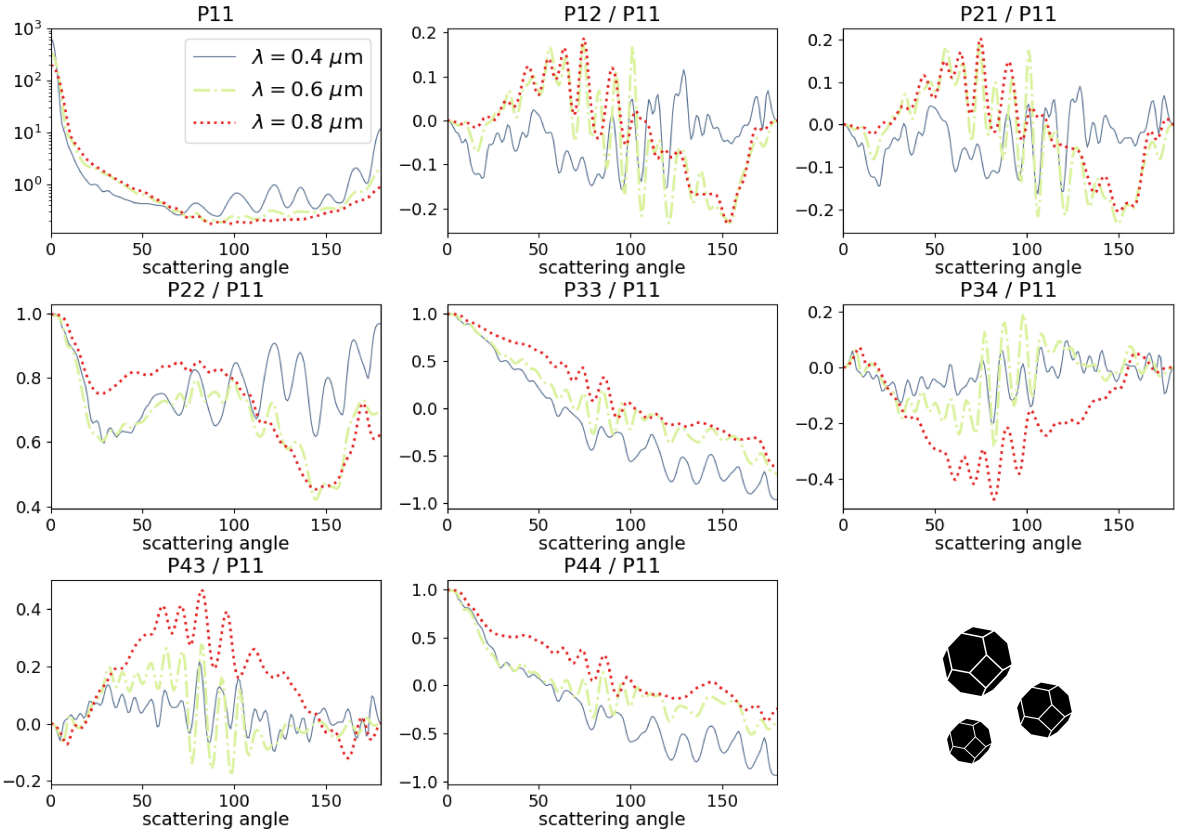

Figure 3.10: Same as Figure 3.8 but for a size distribution of cube-octahedra.

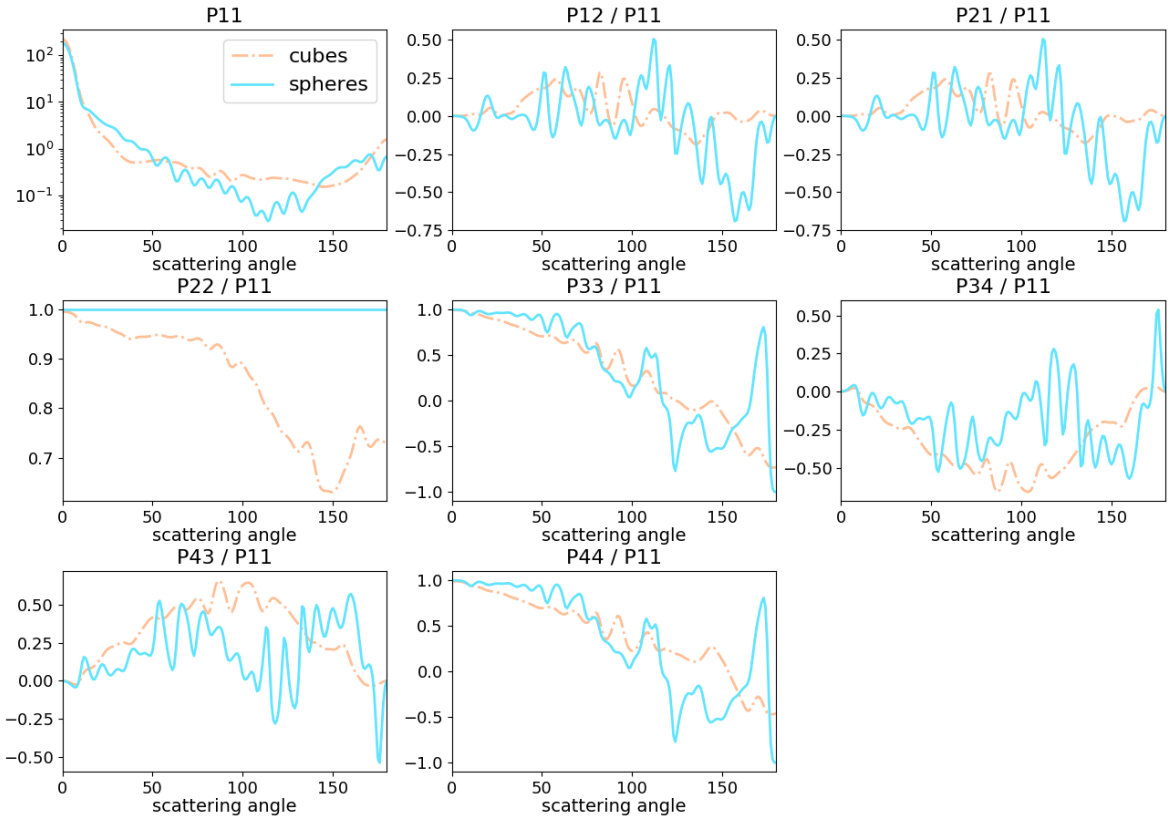

Figure 3.11: Comparison of scattering matrix elements for log-normal size distributions of spheres and cubes for equivalent volume radii between 1 and 3 µm, median radius 2.2 µm. Results are for a wavelength of 0.8 µm, corresponding to size parameters x between 7.8 and 23.5. Results for several size parameters were generated with ADDA, the detailed method is described in Section 3.6. Cubes are represented by the blue lines and spheres by the red lines. Both shapes show strong forward scattering and weaker back-scattering, however, spheres exhibit clearer peaks in the phase function whereas cubes results in a smoother phase function for θ between 50° and 130°. Also spheres show a sharp valley and peak at low scattering angles in the linear polarization (P_{12}).

4

PA3S code

This chapter discusses the Monte Carlo code that has been developed for this research, named PA3S (Polarized Atmospheric Spherical Shell Simulation). Section 4.1 starts with a brief overview of some important features. Section 4.2 explains the coordinate systems used in the code. In Section 4.3 a photon is followed conceptually along its path to explain the main steps in the algorithm. The chapter ends with a note on CPU-times in Section 4.4. This is relevant since Monte Carlo simulations are known for long computing times.

4.1. Code overview and main features

The most important feature of PA3S are the spherical shells used to represent the atmosphere. This feature allows for simulation of twilight lighting conditions, a feature that is not possible with plane-parallel radiative transfer codes. Other notable features are (some of which are possible with a plane-parallel code):

- adjustable size of planet and planetary atmosphere
- arbitrary number of layers
- arbitrary number and size of detectors placed on the surface or in the atmosphere, giving results for multiple solar elevations in one run
- the possibility of three types of scatterers: gas, dust and cloud
- control of the maximum order of scattering

4.1.1. Adding different constituents

All atmospheric constituents are defined beforehand by giving their scattering matrices as input. For each layer a different combination of gas and dust is generated by setting their relative optical thicknesses. The distinction of the two in the code is that optical thickness of the gaseous constituent is set by adjusting its pressure for each layer, for dust the optical thickness is set directly. Clouds are handled differently from the gas and dust because they add a non-homogeneity to a layer, whereas the gas and dust are homogeneous within a layer. This distinction in terminology is important because clouds are technically just another aerosol, but in the context of the code they are considered different. Currently the code includes one type of gas, one type of dust and one cloud. An arbitrary mixture of gases and dust (or other aerosols) could be used by adding up the scattering matrices of the gases and aerosols using Equation 2.25. Another option would be to read in more scattering matrices with the subroutines that are present. Note that scattering matrices used as input to the program should be normalized over the solid angle (P11 integrated over the full solid angle should equal 1, see Section 3.3), as no normalization of the scattering matrix is performed by the code.

4.1.2. Layers

Because twilight illumination conditions cannot be simulated assuming a plane parallel atmosphere, the simulation uses a spherical atmosphere. This spherical atmosphere consists of spherical shell layers, similar to the layers of an onion. Each layer is homogeneous and contains a gas (mixture) and (optionally) aerosols in varying fractions. This means that the scattering cross-sections, absorption cross-sections, optical thicknesses of all the constituents and the total optical thickness are all constant in a single layer.

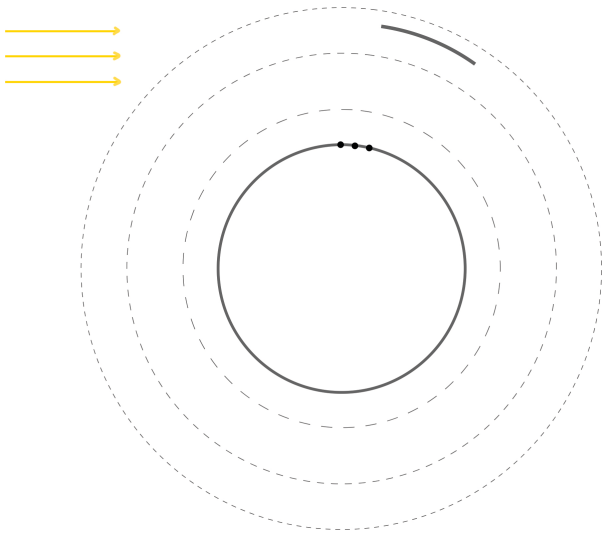

Figure 4.1: Schematic 2D depiction of a code setup with three layers and a cloud present. The cloud is represented by the thick black arc in the third layer. Three detectors (black dots) have been placed on the planet surface. The incident sunlight is shown in the top left.

4.1.3. Point sources disk

Illumination by the Sun is simulated by placing point sources in a disk and releasing photons, all in the same direction. This disk is formed by dividing up a square that covers the entire disk into an arbitrary number of cells. Photons are released from the midpoints of each cell. This ensures that each source represents the same amount of solar flux because the cell areas are all equal. If photons from a source do not hit the atmosphere (i.e. the source falls outside of the radius of the planetary disk), the source is discarded. Errors in incoming flux are introduced since a circle is approximated with squares. Decreasing the distance between the sources reduces these errors. See Figure 4.2 for a graphical representation of the sources. The sources plane can be constrained to exclude certain sources, which is used to reduce computation times. If for instance the northern hemisphere with an optically thin atmosphere is of interest, there is no need to emit photons from sources that cover the southern hemisphere since virtually none of them will have an effect in the northern hemisphere.

4.1.4. Detectors

Detectors are placed on the surface to store the Stokes parameters of photons that reach them. At a detector, flux from various directions is stored in four matrices that represent each Stokes parameter. Every element in the 2D matrix represents the discretized elevation-azimuth. Each detector area must be equal to properly compare the flux they receive. To achieve this, a congruent, equal-area mesh is formed on a sphere representing the detector radius, see Figure 4.3. Each cell in this mesh has constant $cos\,\phi$ and constant λ. A disadvantage of this approach is that cells do not have constant aspect ratio.

The mesh can be constrained by defining a detector latitude and longitude range, and the number of latitude and longitude nodes is adjustable. See Figure 4.3. In this research only a small area on the surface in the twilight-zone is of interest, but detectors can be placed at arbitrary locations in the atmosphere. Only storing photons near the twilight zone improves run times and reduces memory storage of the output data. Photon directions are stored as elevations and azimuths at detectors.

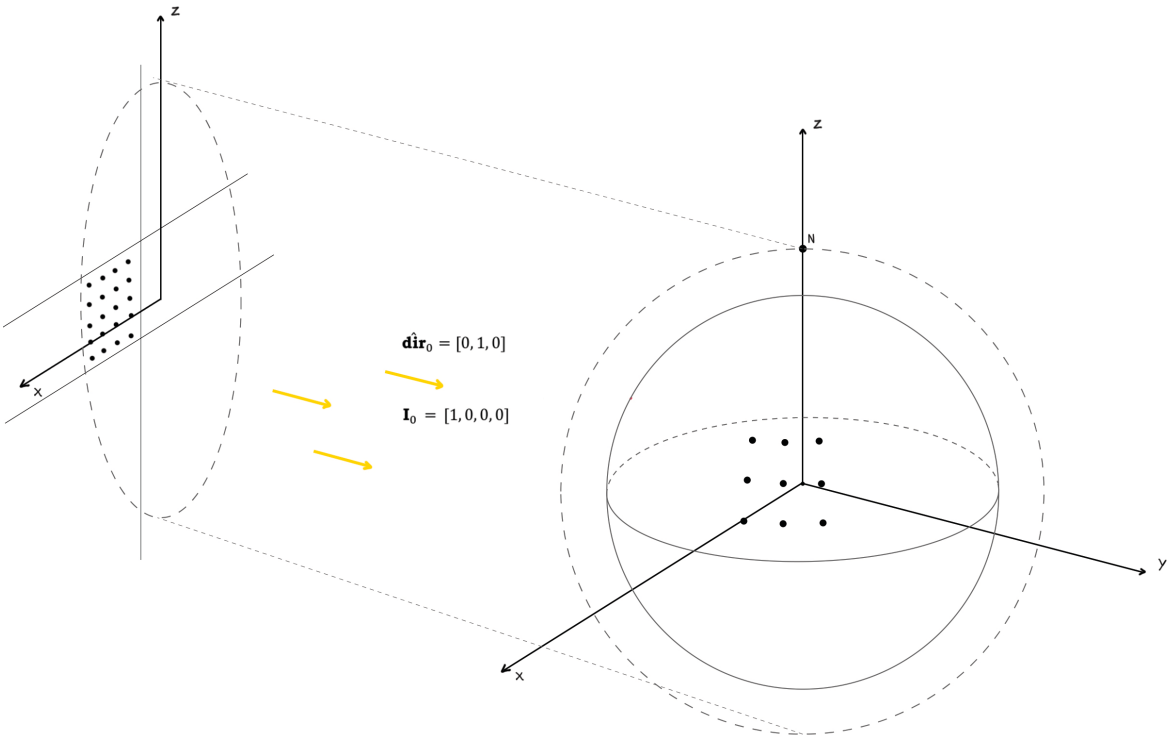

Figure 4.2: Figure showing the setup of the disk containing the point sources representing sunlight. Number and location of sources is adjustable by constraining their allowed x- and z-coordinates in the sources disk. This is to shorten run-times when only a select number of detectors is of interest. In this figure nine detectors are visible on the planet. The sources disk can be thought of as the 2D projection of the planet sphere (with atmosphere). Photons are by default released in a direction parallel to the y-axis: $\hat{\mathbf{dir}}_0 = [0, 1, 0]$. Released photons are unpolarized: $\mathbf{I}_0 = [1, 0, 0, 0]$.

When a photon falls within a detector's borders, the photon is counted as if it intersected the center of the detector. In other words it is shifted to the middle of a detector cell, see Figure 4.4. The spatial resolution of the code is thus the size of a detector cell.

4.2. Coordinate Systems

The code uses a planetocentric reference frame for photon propagation and scattering. The reference frame is inertial, rotation of the planet is not considered. A run of PA3S simulates lighting conditions at one instant in time, therefore planetary rotation is not relevant. Lighting conditions for different solar elevations can be analysed simply by placing detectors on different locations on the planet. See Figure 4.5, photon positions ($\mathbf{p}$) are tracked by their Cartesian coordinates in the planetocentric reference frame, directions ($\hat{\mathbf{dir}}$) are Cartesian unit vectors in a photon's reference frame. In the context of rotation of Stokes vectors at photon scattering (Subsection 4.3.4) it is useful to express the photon's direction in spherical coordinates in the photon reference frame, φ and ϑ in Figure 4.5.

In Figure 4.6, the planetocentric reference frame is also depicted but with the planet's surface included. The x-axis goes through the planets meridian that divides the day-side and night-side, the y-axis is aligned with the incoming direction of the solar flux and the z-axis passes the planet's North pole. Detector positions are defined by their latitude and longitude on the planet. The x-axis of the Cartesian frame goes through the prime meridian (where longitude is zero), latitude is zero at the equator.

Each detector has it own East-North-Up (ENU) directions. Photon directions are stored as elevations and azimuths relative to a local horizontal reference at a detector consisting of the ENU directions. Azimuth is zero in North direction and is positive counter-clockwise when looking towards the zenith, elevation is zero at the horizon and 90 degrees at zenith. Negative elevations are possible in the program, but in this research the detectors are on the surface and negative elevations are therefore never encountered. See the depiction of the sky-dome, relevant angles and unit vectors at a detector

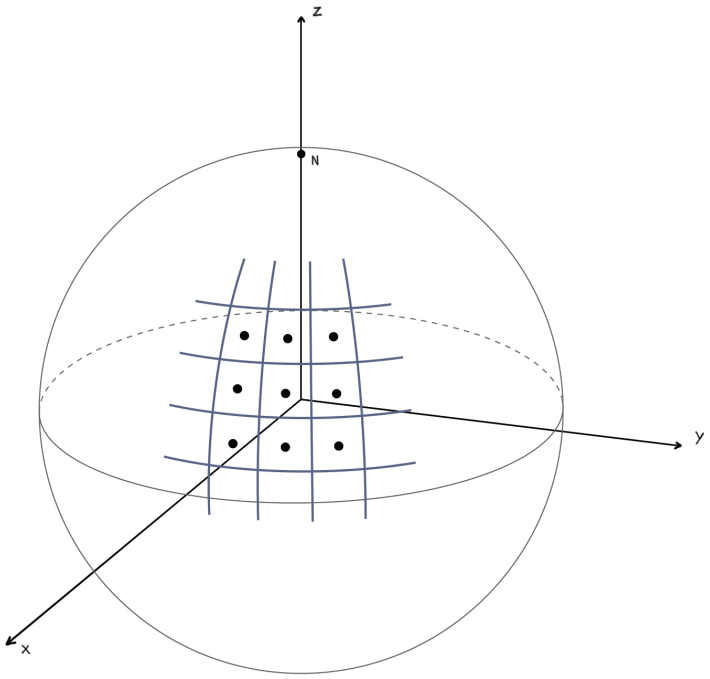

Figure 4.3: Depiction of nine detector cells on the planet surface. In the congruent detector mesh, each cell area is equal because cell heights gradually stretch towards the poles.

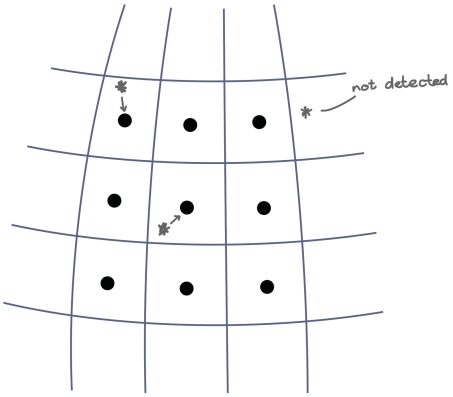

Figure 4.4: Zoomed in part of Figure 4.3 showing three photon packets (grey stars). Two of them land within detector cells, their detection location is moved to the middle of the cell. One photon packet lands outside of the detector range and is not detected.

position in Figure 4.7. Note that the ENU-vector in Figure 4.7 are the same as in the planetary frame in Figure 4.6.

Summarized, when a photon is detected, its Cartesian position and direction (w.r.t. a planetary frame) are converted into a latitude-longitude position (w.r.t. a planetary frame) and a local elevation-azimuth direction (w.r.t. the local horizontal plane at a detector). The local ENU-vectors of a detector latitude-longitude position are found with an algorithm described by Subirana et al. (2011).

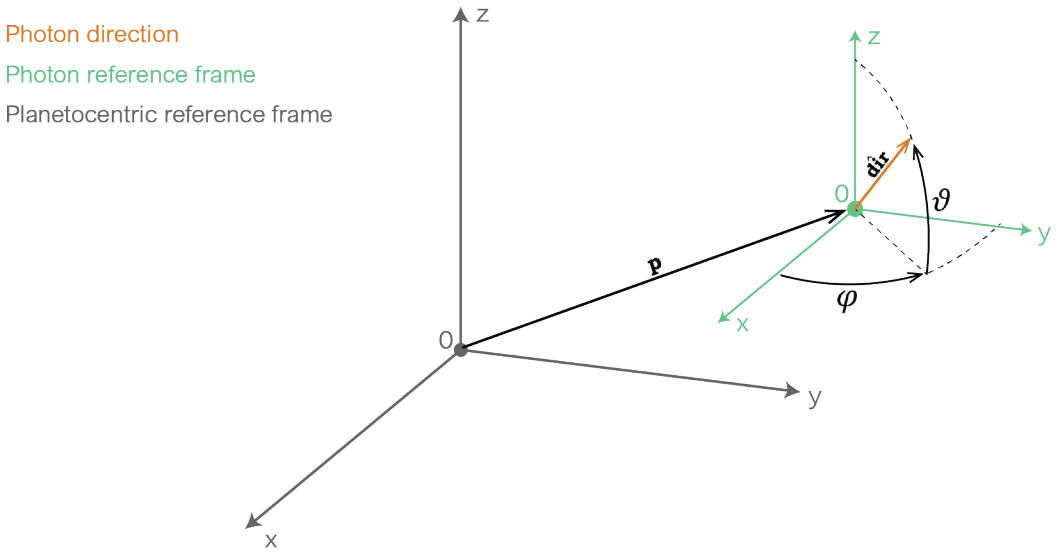

Figure 4.5: Figure showing the planetocentric reference frame used to track photon positions, $\mathbf{p}$. The photon's direction is expressed in the photon reference frame in Cartesian coordinates, $\hat{\mathbf{dir}}$. The photon direction is expressed in spherical coordinates, φ and ϑ, in the case of Stokes vector rotation at scattering, detailed in Subsection 4.3.4. This is done to be able to use spherical trigonometry.

$$\begin{aligned}\hat{\mathbf{e}} &= (-sin\,\lambda,\, cos\,\lambda, 0)\\ \hat{\mathbf{n}} &= (-cos\,\lambda\, sin\,\phi,\, -sin\,\lambda\, sin\,\phi,\, cos\,\phi)\\ \hat{\mathbf{u}} &= (cos\,\lambda\, cos\,\phi,\, sin\lambda\, cos\,\phi,\, sin\,\phi)\end{aligned} \tag{4.1}$$

where ϕ is latitude and λ is longitude. With the ENU-vectors of a local detector, the Cartesian direction-vector $\hat{\mathbf{dir}}$ of a photon can be transformed into a local elevation, el, and azimuth, az, as follows (Subirana et al., 2011).

$$\begin{aligned}el &= arcsin\left(-\hat{\mathbf{dir}} \cdot \hat{\mathbf{u}}\right)\\ az &= arctan\left(\frac{-\hat{\mathbf{dir}} \cdot \hat{\mathbf{e}}}{-\hat{\mathbf{dir}} \cdot \hat{\mathbf{n}}}\right)\end{aligned} \tag{4.2}$$

4.3. Algorithm

PA3S has two main phases: the setup phase and the photon propagation phase. After the setup phase the user can review the settings and cancel the program or start the propagation phase. Photon propagation is done in parallel for better performance. See Figure 4.8 for a flow chart of the PA3S algorithm. Key elements of the program are explained in the following subsections.

4.3.1. Setup - initial values

During the setup phase, the sources, detectors and layers are initialized. Input scattering matrices and optical thicknesses of the gas, dust and clouds are read and combined into one scattering matrix for each layer with Equation 2.25. The single scattering albedo of each layer is calculated from the scattering and absorption optical thicknesses of the constituents with Equation 2.26. The total optical thickness is found for each layer with Equation 2.27. If enabled, the extent and thickness of the cloud's spherical shell segment is initialized. The photons are all moved from the source disk to the top of the atmosphere where initially the direction is $\hat{\mathbf{dir}}_0 = [0, 1, 0]$ (parallel to the y-axis, see Figure 4.2). The initial Stokes vector of the photon packet $\mathbf{I}_0 = [1, 0, 0, 0]$ represents unpolarized light. This initial Stokes vector is defined with respect to the plane containing the propagation direction and the local vertical.

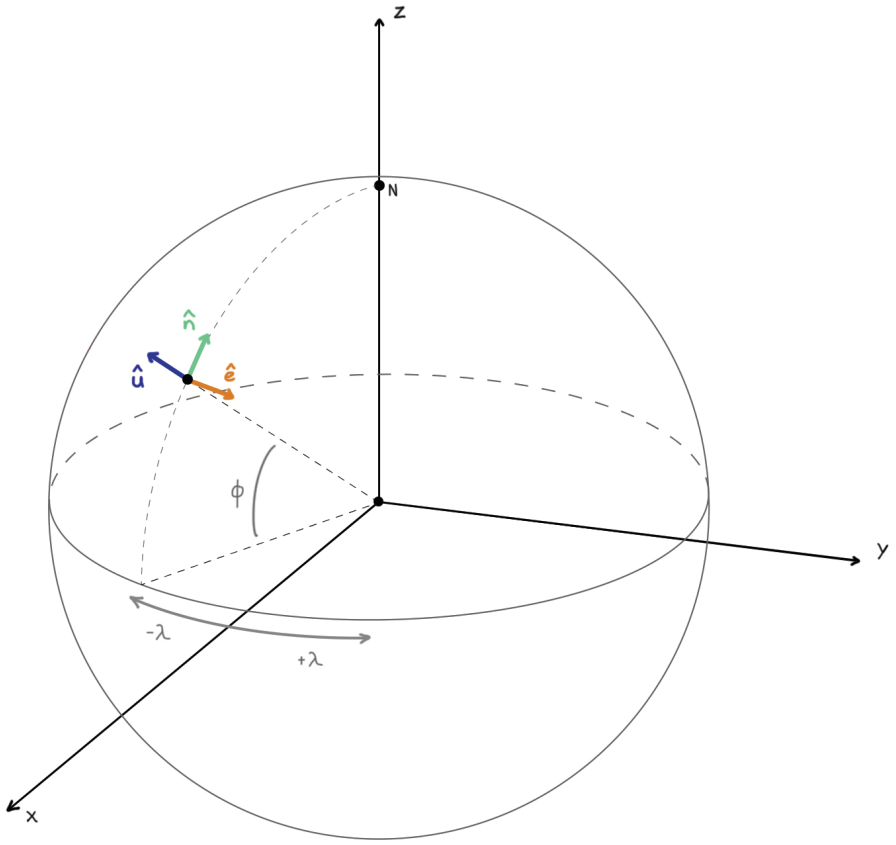

Figure 4.6: Overview of the planetocentric coordinate system used in the code. Photon propagation is done using Cartesian coordinates, the x-axis splits the planet in day-side and night-side, the z-axis goes through the North pole. Detector locations are defined with longitudes (zero at x-axis) and latitudes (zero at equator). At detectors, auxiliary East-North-Up unit vectors are used to transform an incoming Cartesian direction to an azimuth and elevation in a local horizontal detector frame, see Figure 4.7 for a sky-dome centered at such a detector position.

After a scattering event this reference plane changes because the direction has changed (though the plane is always vertical in the Cartesian plane during propagation).

4.3.2. Photon distance travelled

The algorithm in this subsection is based on Wood et al. (2013). After a photon is released from a source, it starts moving through the atmosphere. Each layer has a certain optical thickness which is a combination of the optical thicknesses of the gas, dust and clouds. These layer optical thicknesses have been calculated in the setup phase. The optical thickness along a path indicates the number of mean free paths of a photon along a path. In other words; it indicates the number of interactions a photon will have on average. Randomness is introduced by introducing a random optical thickness from one interaction to the other. This random τ_r will subsequently be scaled with the layer's optical thickness, τ_{layer}, and the layer's radial extent, Δr_{layer} to generate a distance travelled by the photon. The value e^{τ} is the probability that the photon moves an optical thickness τ without interacting. The opposite probability, interacting *before* travelling the full optical thickness is $1 - e^{\tau}$. A random number can be sampled from the probability density function in the following way: $x = 1 - e^{\tau}$. This leads to the following

$$\tau_r = -log(1 - x)\,, \tag{4.3}$$

where x is a random number uniformly distributed between 0 and 1. Now a distance travelled between interactions is found with

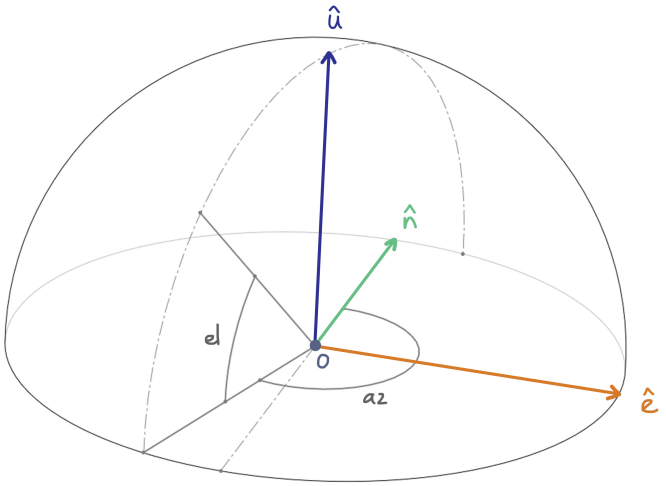

Figure 4.7: Depiction of a sky dome around a horizontal reference frame at a detector on the planet's surface. Compare the East-North-Up (ENU) unit vectors with those in Figure 4.6 where a set of these vectors is also plotted but in the context of the entire planet. The ENU unit vectors are used to transform incoming Cartesian photon directions ($\hat{\mathbf{dir}}$) into azimuths and elevations with Equations 4.1 and 4.2. In this reference frame, azimuth ,az, is zero at $\hat{\mathbf{n}}$ and is positive counter-clockwise when looking in the direction of $\hat{\mathbf{u}}$. The elevation, el, is zero at the horizon and 90° at the zenith.

$$L = \frac{\tau_r}{\tau_{layer}} * \Delta r_{layer} \, . \tag{4.4}$$

4.3.3. Travelling through layers

In PA3S it is possible to define an arbitrary number of layers to represent altitude differences in optical properties of actual atmospheric layers. Checking whether or not the photon moves into another layer is done by comparing the distance travelled (see Subsection 4.3.2) with the distance to an intersection with a layer boundary. Intersections are found taking into account that a photon cannot intersect a layer moving backward. At each iteration, it is checked if the photon has moved down a layer or up a layer. Moving down a layer is always checked first. A photon could intersect multiple layer boundaries if the distance travelled is long enough. If a photon intersects both the lower and upper layer, the distance to the intersection with the lower layer is always closer. A photon cannot intersect both layer boundaries *and* be closer to the upper layer intersection because it cannot move backward. This is evident from Figure 4.9.

Layer crossings are evaluated by finding intersections of a line (photon path) and a sphere (layer boundaries) in 3D. The equation of a sphere in 3D can be written as

$$r^2 = \|\mathbf{p} - \mathbf{c}\|^2 = \|\mathbf{p} - \mathbf{0}\|^2 \, , \tag{4.5}$$

where $\mathbf{p}$ is a point on the sphere and $\mathbf{c}$ is the position vector of the sphere center. Every layer boundary is a spherical surface with the sphere center at the planet center, therefore $\mathbf{c} = [0, 0, 0]$ in the Cartesian grid. A point on a line in 3D can be written with the following vector notation:

$$\mathbf{p} = \mathbf{p_0} + t\,\hat{\mathbf{dir}} \, , \tag{4.6}$$

here $\mathbf{p_0}$ is the line origin (the last known photon location), $\hat{\mathbf{dir}}$ is the direction unit vector and t is a distance along the line. To find an intersection between the line and sphere the equations are combined. After some manipulation the result is

$$(\hat{\mathbf{dir}} \cdot \hat{\mathbf{dir}})\, t^2 + 2(\hat{\mathbf{dir}} \cdot \mathbf{p_0})\, t + \mathbf{p_0} \cdot \mathbf{p_0} - r^2 = 0 \, . \tag{4.7}$$

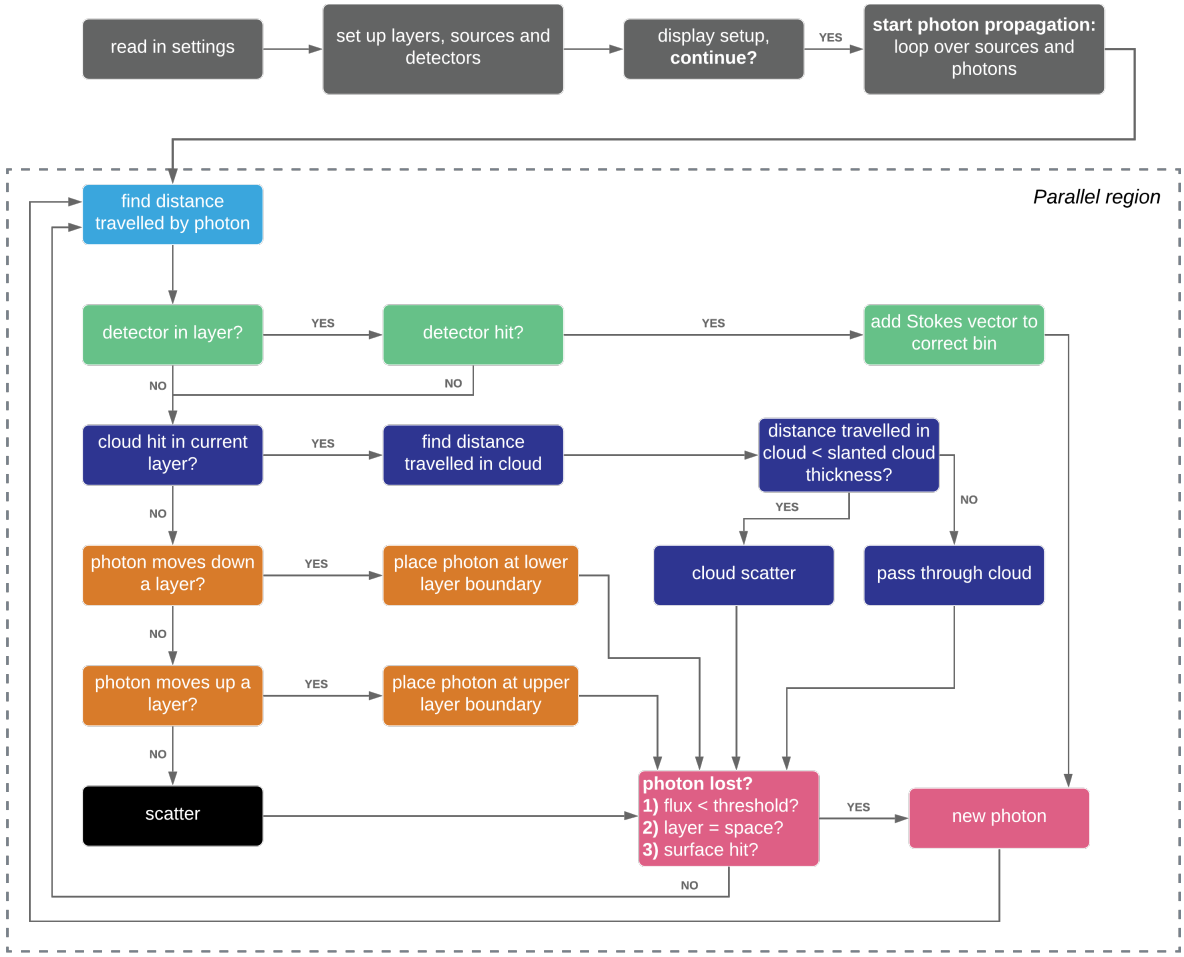

Figure 4.8: Flow chart of PA3S algorithm.

This is a quadratic equation in t. The equation can have no solutions (no intersection), one solution (line tangent to sphere) and two solutions (two intersections). In the algorithm, negative solutions are not valid because a photon can not travel backwards on its path. If there is a solution and the distance travelled is more than t the photon moves into the new layer and is placed at the layer boundary. If there are two positive solutions for t, the smaller of the two is taken since the photon reaches the intersection corresponding to the smaller t first.

4.3.4. Photon scattering

When a photon packet has travelled the distance L, it encounters a particle. Subsequently it can scatter and can possibly be partially absorbed. These two processes constitute interactions in the PA3S code (emission is ignored as stated in Section 2.2). In the setup phase the combined scattering matrices for each layer have been constructed. To determine the new direction of the photon packet after scattering, a scattering angle, θ, and azimuthal angle of scattering, ψ, have to be generated, see Figure 4.10. The scattering angle is also required to determine the new polarization state because the scattering matrix, $P(\theta)$, depends on θ). The algorithm is different for the cases of single scattering (photon has not yet scattered) and multiple scattering (photon has already scattered at least once) as will be explained in the following text.

Sampling single scattering θ with rejection method

The phase function (the (1,1)-element of the scattering matrix) represents the probability that a photon is scattered in a certain direction. Integrating the phase function over the whole solid angle equals a probability of 1. The azimuthal angle, ψ, is sampled uniformly from the range 0 - 2π. A scattering angle, θ, is sampled from the combined phase function using the rejection method. The method requires to

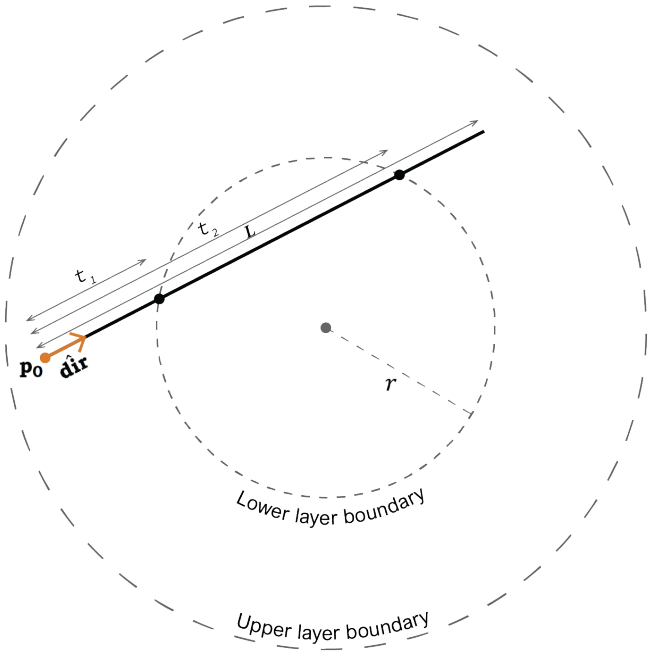

Figure 4.9: Figure showing variables used to check if a photon travels to another layer. The photon's last position is at $\mathbf{p_0}$, the photon propagation direction is $\hat{\mathbf{dir}}$, the radius of the lower layer boundary is r. Intersections between a the photon path (a line) and a layer boundary (a sphere) are found with Equation 4.7. In this figure, two intersections with the lower layer exist (one or zero intersections are also possible). The travelled photon path,L is longer than the distance to the closer intersection, t_1, and therefore the photon is placed at this closer intersection.

generate a random θ_r uniformly from 0 - π and a probability P_r uniformly from 0 - 1. The corresponding probability that the photon scatters in direction θ_r is:

$$P(\theta_r) = P_{11}(\theta_r) I_0 \ . \tag{4.8}$$

If $P(\theta_r) \geq P_r$, then θ_r is accepted as the scattering angle. Otherwise, a new θ_r is generated until the condition is met.

Sampling multiple scattering θ and ψ with rejection method
If the photon has already scattered once, Stokes parameters Q and U can be non-zero and they play a part in finding the scattering direction. Now both θ and ψ have to be sampled. A θ_r is sampled uniformly from 0 - π and a ψ_r is sampled from 0 - 2π. Again, a random probability, P_r, is sampled uniformly from 0 - 1. Now the probability that the photon scatters in direction θ, ψ is

$$P(\psi, \theta) = P_{11}(\theta) I_0 + P_{12}(\theta)[Q_0 cos(2\psi) + U_0 sin(2\psi)] \ . \tag{4.9}$$

If $P(\psi_r, \theta_r) \geq P_r$, θ, and ψ are accepted as the scattering angle and azimuthal angle. So, in contrast to the single scattering rejection method, the P_{12}-element of the scattering matrix also plays a role in multiple scattering.

Stokes vector rotation at scattering event
With θ and ψ the scattered direction can be found. The scattering matrix transforms an incoming Stokes vector into a scattered Stokes vector. This matrix is defined in the scattering plane. However, the incident Stokes vector is defined with respect to a different plane. Out of convenience, this plane is always the plane containing the direction, $\hat{\mathbf{dir}}$, and the local z-direction in the photon reference frame, see Figure 4.5. In Figure 4.11 from Hovenier and Van der Mee (1983), $\hat{\mathbf{dir}}$ corresponds to OP_1 and the local z-direction is ON, thus the plane the incident Stokes vector is with respect to the plane defined by ONP_1. The Stokes vector first has to be rotated to the scattering plane OP_1P_2 over an angle corresponding in magnitude to σ_1. Next, it is transformed by the scattering matrix. Finally, it

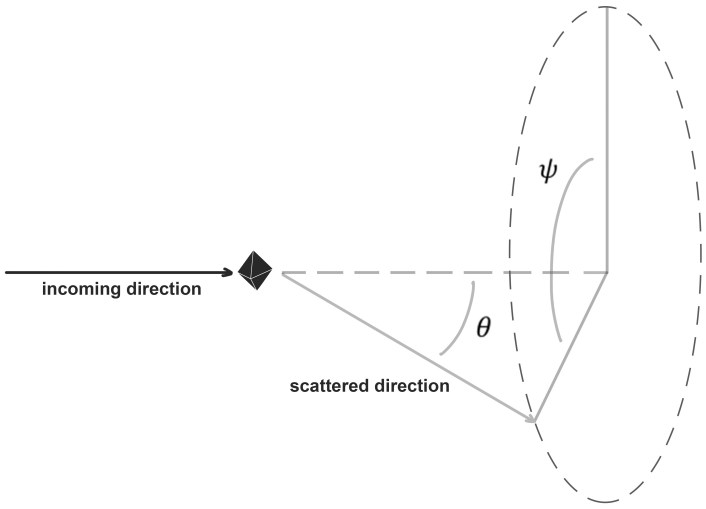

Figure 4.10: Figure showing the scattering angle, θ, and azimuthal angle of scattering, ψ. These angles determine the scattered direction.

is rotated over angle σ_2 to define it with respect to the plane containing the scattered direction (OP_2 or the new $\hat{\mathbf{dir}}$) and local North (ON or the local z-direction in the photon reference frame), i.e. the plane containing ONP_2. The incoming elevation and azimuth, ϑ' and φ', are found by transforming the incoming Cartesian photon direction, $\hat{\mathbf{dir}}$, to spherical coordinates in the photon reference frame (depicted in Figure 4.5). With θ and ψ (generated in the previous step), the scattered direction in spherical coordinates, ϑ , φ, can be calculated. Now, the angles σ_1 and σ_2 can be found using spherical triangles.

Firstly, σ_1 is defined by ψ. If $\varphi' > \varphi$ as in Figure 4.11, σ_1 simply equals ψ. By convention positive rotations are defined to be counter-clockwise when looking in the propagation direction (looking from O to D). In this case the rotation is negative, and the rotation matrix $L(\alpha)$ with $\alpha = -\sigma_1$ is

If $\varphi' < \varphi$ then $\sigma_1 = \psi - \pi$ and the rotation is counter-clockwise, thus positive. Resulting in

$$L(\sigma_1) = \begin{bmatrix} 1 & 0 & 0 & 0 \\ 0 & cos(2\sigma_1) & sin(2\sigma_1) & 0 \\ 0 & -sin(2\sigma_1) & cos(2\sigma_1) & 0 \\ 0 & 0 & 0 & 1 \end{bmatrix}. \tag{4.10}$$

In both cases the scattering matrix is transformed in plane ODS using scattering matrix $P(\theta)$:

$$P(\theta) = \begin{bmatrix} P_{11}(\theta) & P_{12}(\theta) & 0 & 0 \\ P_{12}(\theta) & P_{22}(\theta) & 0 & 0 \\ 0 & 0 & P_{33}(\theta) & P_{34}(\theta) \\ 0 & 0 & P_{34}(\theta) & P_{44}(\theta) \end{bmatrix}. \tag{4.11}$$

The angle σ_2 can be found using the Side-Angle-Side problem from spherical trigonometry (Wertz, 2001)

$$\sigma_2 = acos2\left[\frac{cos(\frac{\pi}{2} - \vartheta') - cos(\theta)cos(\frac{\pi}{2} - \vartheta)}{sin(\theta)sin(\frac{\pi}{2} - \vartheta)}, H(\frac{\pi}{2} - \vartheta')\right]. \tag{4.12}$$

If $\varphi' > \varphi$, the rotation from ODS to ONS is counter-clockwise (positive). If $\varphi' < \varphi$, this rotation will be clockwise (negative). Thus the rotation matrix will be

or

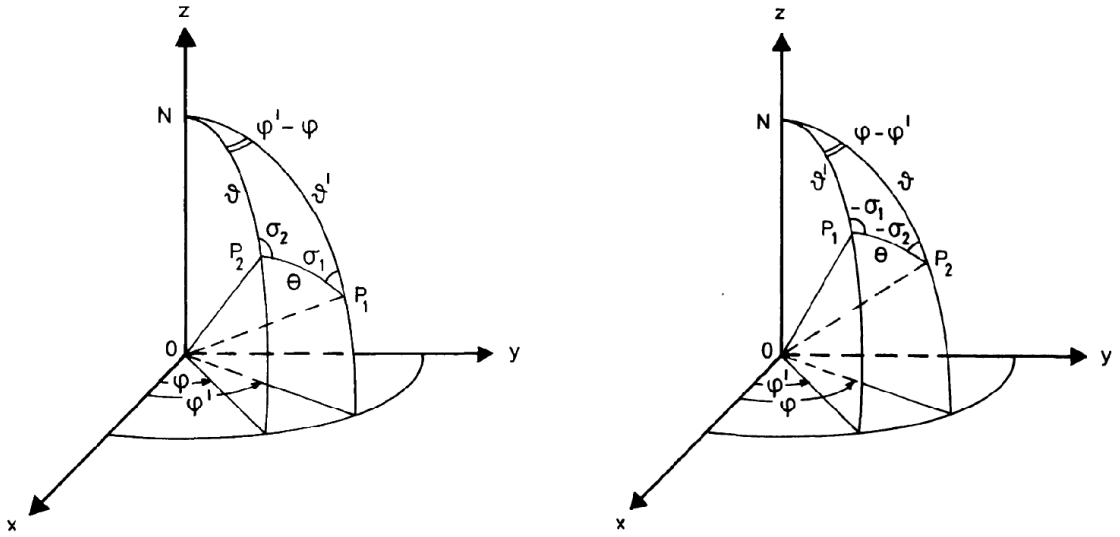

Figure 4.11: Figure from Hovenier and Van der Mee (1983), the xyz-frame is centered around the scattering volume at O, direction of incident light is OP_1, direction of scattered light is OP_2. The left figure shows a situation where incoming azimuth φ' is larger than scattered azimuth φ, right figure shows the opposite situation. The Stokes vector has to be rotated an angle σ_1 from plane ONP_1 to scattering plane OP_1P_2 before it is multiplied by the scattering matrix, finally the Stokes vector is rotated to plane ONP_2.

This results in case 1, $\varphi' > \varphi$:

$$\begin{bmatrix} I \\ Q \\ U \\ V \end{bmatrix}_s = L(+\sigma_2)P(\theta)L(-\sigma_1)\begin{bmatrix} I \\ Q \\ U \\ V \end{bmatrix}_i , \tag{4.13}$$

and case 2, $\varphi' < \varphi$:

$$\begin{bmatrix} I \\ Q \\ U \\ V \end{bmatrix}_s = L(-\sigma_2)P(\theta)L(+\sigma_1)\begin{bmatrix} I \\ Q \\ U \\ V \end{bmatrix}_i . \tag{4.14}$$

4.3.5. Interaction with a cloud

In the program a cloud is represented as a part of a spherical shell that has a different scattering matrix and optical thickness compared to the rest of the layer, see Figure 4.12. The scattering matrix, single scattering albedo and optical thickness of the CO_2 ice particles is included in Equations 2.26 and 2.27. The cloud shell element is defined with a certain latitude range ($\phi_{cl,min}$, $\phi_{cl,max}$), longitude range ($\lambda_{cl,min}$, $\lambda_{cl,max}$) and a radial extent ($r_{cl,min}$, $r_{cl,max}$). Now, the same equations as for finding intersections with layer boundaries from Subsection 4.3.3 can be used to find an intersection point with the cloud, $\mathbf{p}_{isct}$. Since the clouds on Mars are relatively thin, $\mathbf{p}_{isct}$ is calculated for a sphere with radius $(r_{cl,min} + r_{cl,max})/2$, instead of separately checking for intersections with two spheres with radii $r_{cl,min}$ and $r_{cl,max}$. Because the cloud is a shell element and not a full spherical shell, an added check is performed to confirm that the intersection point is within the cloud's latitude- and longitude-range, $\phi_{cl,min} \leq \phi_{isct} \leq \phi_{cl,max}$ and $\lambda_{cl,min} \leq \lambda_{isct} \leq \lambda_{cl,max}$. If so, the next step is to check whether or not the photon interacts with the cloud or passes through the cloud. Now, locally the cloud is assumed to be a flat plate with a certain thickness, $t_{cl} = r_{cl,max} - r_{cl,min}$. The cloud entry angle, α_{entry}, is determined with

$$\alpha_{entry} = arccos\left(\frac{\mathbf{p}_{isct} \cdot \hat{\mathbf{dir}}}{||\mathbf{p}_{isct}||\,||\hat{\mathbf{dir}}||}\right) , \tag{4.15}$$

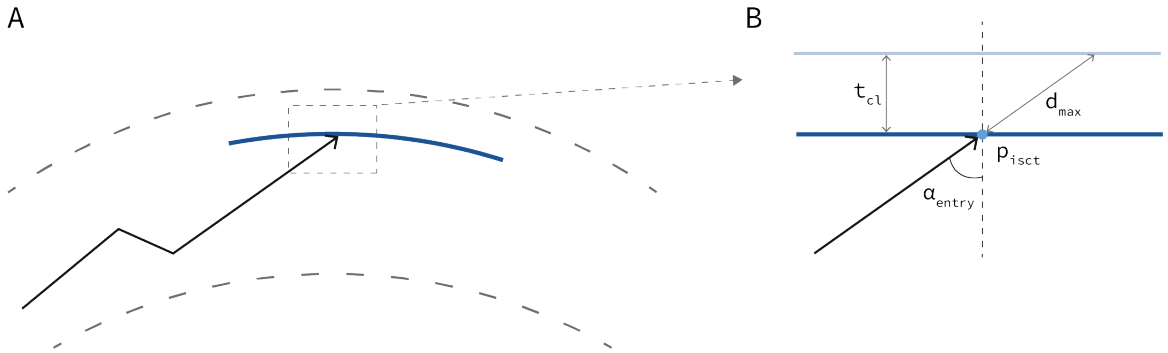

Figure 4.12: Schematic depiction of a photon interacting with a cloud. At A this cloud shell element is depicted with the curved, thick, blue line. The long dashed lines are layer boundaries. Two conditions are needed for a photon to hit a cloud: 1) the photon intersects a sphere with the cloud radius 2) this intersection is within the cloud latitude-longitude range. If the photon hits the cloud, locally the cloud is assumed to be flat with a certain thickness t_{cl}, see B. The light blue point is the cloud intersection, $\mathbf{p}_{isct}$, the entry angle α_{entry} is calculated by finding the angle between the vectors $\mathbf{p}_{isct}$ and $\hat{\mathbf{dir}}$. Then the maximum path through the cloud is $d_{max} = t_{cl}/cos\,\alpha_{entry}$. If a generated path length L (using the cloud optical thickness and the method from Subsection 4.3.2) is smaller than d_{max} the photon is scattered in the cloud, otherwise the photon passes through the cloud.

α_{entry}, is used to find the maximum path length through the cloud: $d_{max} = t_{cl}/cos\,\alpha_{entry}$. A photon path length before interaction, L, is generated in the same way as described in Subsection 4.3.2. If $L < d_{max}$ the photon will scatter due to the cloud particles, otherwise it will pass through the cloud. In this way transmission and scattering by the cloud are simulated. Note that to simplify the algorithm, photons that have already scattered once in the atmosphere are ignored, their contribution to skylight measured from the surface is negligible for the high altitude clouds.

4.3.6. Detection and another Stokes vector rotation

When the photon is present in a layer with detectors, it is checked whether or not the photon hits a sphere with the same radius as the detector using the equations as in Subsection 4.3.3. For example, if the detectors are at surface level, the algorithm checks if the photon hits the surface. Next, it is tested whether or not the intersection point is within the detector latitude- and longitude-range. If this is the case, the intersection point is used to find the correct detector by checking between which set of nodes of the detector bins the intersection is located, see Figure 4.4. Subsequently, the Cartesian direction unit-vector is converted into elevation and azimuth with Equation 4.2. A nearest neighbor binary search over 91×361 direction-bins (91 elevation bins and 361 azimuth bins) is performed with the converted elevation and azimuth and the incoming Stokes parameters are added to the correct direction-bin.

In Subsection 4.3.1, it was mentioned that Stokes vectors in this code are always referenced with respect to planes that are vertical in the Cartesian reference frame (planes containing the propagation direction, $\hat{\mathbf{dir}}$, and unit vector $[0, 0, 1]$. However, this representation is not practical in the local horizontal frame at a detector (Figure 4.7). The photon Stokes vector is rotated to the local meridian in the horizontal frame containing the incoming direction, using the same rotation method as in Subsection 4.3.4. The local meridian corresponds to the plane containing $\hat{\mathbf{dir}}$ and the local up-direction, $\hat{\mathbf{u}}$. Storing the Stokes vectors in this way allows for easy rotation of the Stokes vectors to an arbitrary meridian in the sky dome, like for example the solar meridian or a meridian aligned with the optical plane of an instrument. This is because the stored Stokes parameters have to be rotated over only one angle with the rotation matrix in Equation 2.10.

4.4. Run times

Monte Carlo simulations are known to have long run times. In PA3S, these increase mainly with the total number of photons. According to Wood et al. (2013), the number of photons in each bin (in PA3S: an adjustable number of detector bins, each containing 91×361 direction-bins) follows Poisson statistics, meaning that the random sampling errors of the energies in each bin are proportional to $1/\sqrt{N_i}$, where N_i is the number of photons in the bins. Thus a lot of photons are necessary to reduce large fluctuations due to sampling errors.

The dependency of run time on the number of photons is fairly linear, but other factors also influence run times. See Figure 4.13 where a plot is presented with run times for several runs at different number of photons. The timing results are given for 1 CPU core, but PA3S has been parallelized with the OpenMP (Open Multi-Processing) API. The actual run time reduces linearly with increasing number of cores. For example, one simulation with $1.7 \cdot 10^{12}$ photons (not plotted in Figure 4.13 to prevent skewing the plot) was performed with 14 cores, taking 114 hours instead of 1596 hours. Parallelization in the program is achieved by dividing photon paths over several cores, since each photon path is completely independent.

Next to the total number of photons, a notable factor that also increases the run time is increasing optical thickness, though the effect is less easily quantifiable compared to the effect of the total number of photons. For an indication, the last two timing results in Figure 4.13 are at equal total number of photons but the total vertical optical thickness (all atmospheric layers combined) differs by a factor of two. With a total atmospheric optical thickness of 0.2 the run time was 21.5 hours, a total optical thickness of 0.4 resulted in 30 hours. Run times also increase with the total number of layers, but this effect has not been investigated thoroughly.

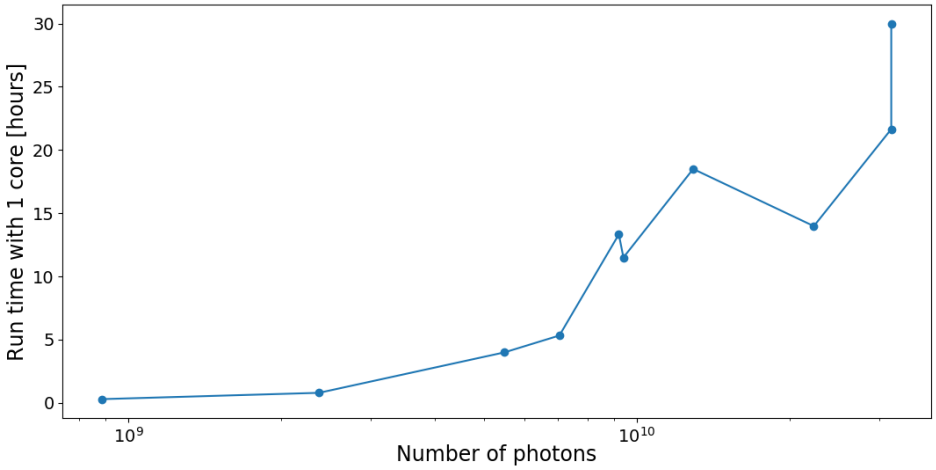

Figure 4.13: Total run time of PA3S code plotted against total number of photons. Plots are given for 1 core, the run time decreases linearly with increasing number of cores. Run time does not increase monotonically with total number of photons because it is also influenced by other factors. Most notably, run times also increase with increasing optical thickness and increasing number of layers.

4.5. Complementary programs

A number of Python scripts have been written to manipulate input and output data. It was necessary to convert scattering matrices from ADDA output and other sources to a standard format readable by the code. Tools have also been developed to generate scattering matrices of size distributions using multiple ADDA outputs (log-normal size distributions, but other distributions are easily implemented). Code output can be stored in text format, HDF5 format (The HDF Group, 1997-2019) or both. For both output file types, scripts have been written to easily visualize the data using the Python library Matplotlib (Hunter, 2007). Figures 4.16 and 4.17, and the figures in Chapter 5 have been generated with these scripts. The complementary scripts, can also produce plots similar to Figure 5.1 in Chapter 5, such a plot is meant to give a quick overview of the settings of a simulation; locations of sources, locations of detectors and the location of a cloud if present.

4.6. Validation of code with polarization portrait of Rayleigh sky

To validate the output of the PA3S code it is compared with the single scattering Rayleigh model. Natural skylight shows a distinct pattern under clear circumstances when only considering photons that have been scattered once. The pattern is visible in the degree of polarization (DoP, I_{pol}/I) and the angle of polarization (AoP, χ), and is a manifestation of the Rayleigh scattering scattering matrix in the sky dome (see Section 2.4 on Rayleigh scattering and Figure 2.6). The DoP and the AoP are calculated from the

Stokes parameters using Equations 2.6 and 2.7. Multiple orders of scattering, haze and clouds in the atmosphere muddle up this clear pattern. Second order scattering creates its own signature which is discussed in Section 5.2. The DoP and the AoP of the single scattering Rayleigh sky model from literature are compared with results from the code. The results have been generated by setting the maximum number of scattering interactions to 1, giving a pure single scattering Rayleigh sky.

When looking at a point in the sky-dome and pure single Rayleigh scattering, the local E-vector always makes a 90° angle with the scattering plane (the plane containing the observed direction and the Sun direction). See Figure 4.14a from Horváth (2014) showing the orientations of the electric vectors for a Rayleigh sky: take any point on one of the circles projected on the dome, the arc between this point and the Sun is perpendicular to the black line tangent to the point, this is true for every point. See Figure 2.4 for another example. The E-vector orientations form concentric circles around the Sun, shifting as the Sun moves across the sky-dome, see Figure 4.14b-c from Horváth (2014). An important note is that the pattern changes when taking the AoP with respect to different planes in the local horizontal reference frame. Several conventions exist for this, common ones are with respect to:

1) the solar meridian, containing the Sun direction and zenith

2) each local meridian, containing the observed direction and zenith (changes for every observed azimuth)

3) the North-South meridian

Different conventions give different patterns for the angle of polarization. In Figure 4.14 by Horváth (2014) convention **1** is used. Figure 4.15 from Pomozi et al. (2001) uses convention **2**. Conventions **2** and **3** give similar patterns but the angles are shifted by the angular distance between the solar meridian and the North-South meridian. This angular distance changes with latitude, on the equator it is 90°.

Plots for the DoP, the AoP and Stokes parameter I (total flux) are given in Figures 4.16 and 4.17. The AoP plots are shown for two conventions: with respect to the local meridian and with respect to the solar meridian. I is given for easy reference of the Sun's location in the sky. Plots of V (circular polarization flux) are not presented because P_{34} of the Rayleigh scattering matrix is zero for all scattering angles, therefore no V is present in the Rayleigh model. Results are presented for a wavelength of 0.4 μm and for two solar elevations, 1.5° (Figure 4.16) and 33.5° (Figures 4.17). Note that in both figures, the bottom-right AoP is taken with respect to the solar meridian (the meridian containing the Sun, zenith and the observer) and should be compared with Figure 4.14 (although pay attention that colors are shifted by 90°, 0° is blue in Figures 4.14 but red in Figures 4.16 and 4.17. In contrast, the bottom-left plots present the AoP with respect to each local meridian and should be compared with Figure 4.15. It is clear from comparison that the simulation results are validated in terms of the single scattering Rayleigh model.

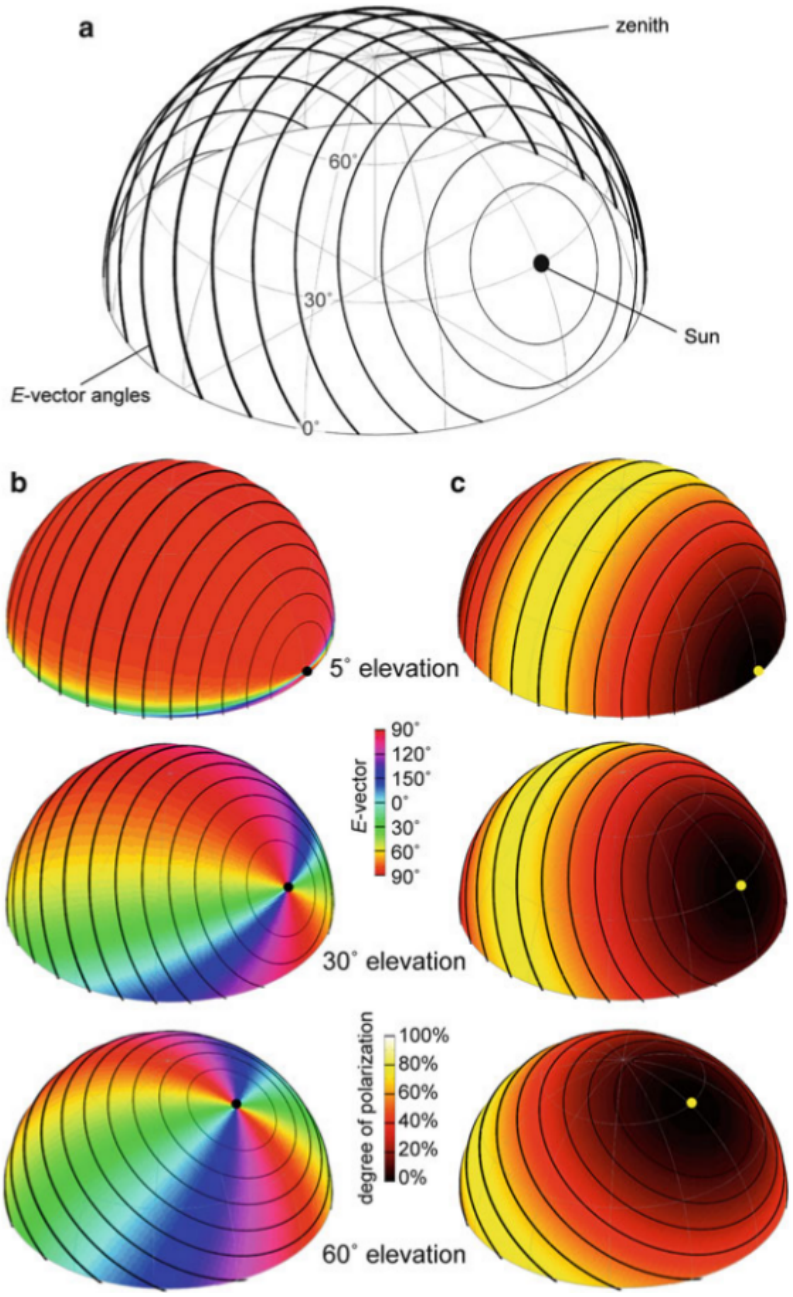

Figure 4.14: In this figure by Horváth (2014) the polarization portrait of the single scattering Rayleigh sky is projected onto a half sphere representing the sky dome. In **a** the E-vector orientations resulting from single Rayleigh scattering are depicted, the E-vector orientations form concentric circles centered around the Sun and anti-Sun. Subfigure **b** shows the angle of polarization (AoP) pattern. The AoP is defined with respect to the solar meridian in this figure (convention **1** in the text). For instance, in red regions the E-vectors are oriented perpendicular to the solar meridian. In **c** the degree of polarization (DoP) is presented. The DoP is minimum at the Sun and anti-Sun and maximum at 90° away from the Sun and anti-Sun, this is a manifestation of element P_{12} of the Rayleigh scattering matrix depicted in Figure 2.6. Comparing the plots in **a** and **b** for the three different solar elevations, it is clear that the concentric circles follow the Sun across the sky, causing the patterns to change.

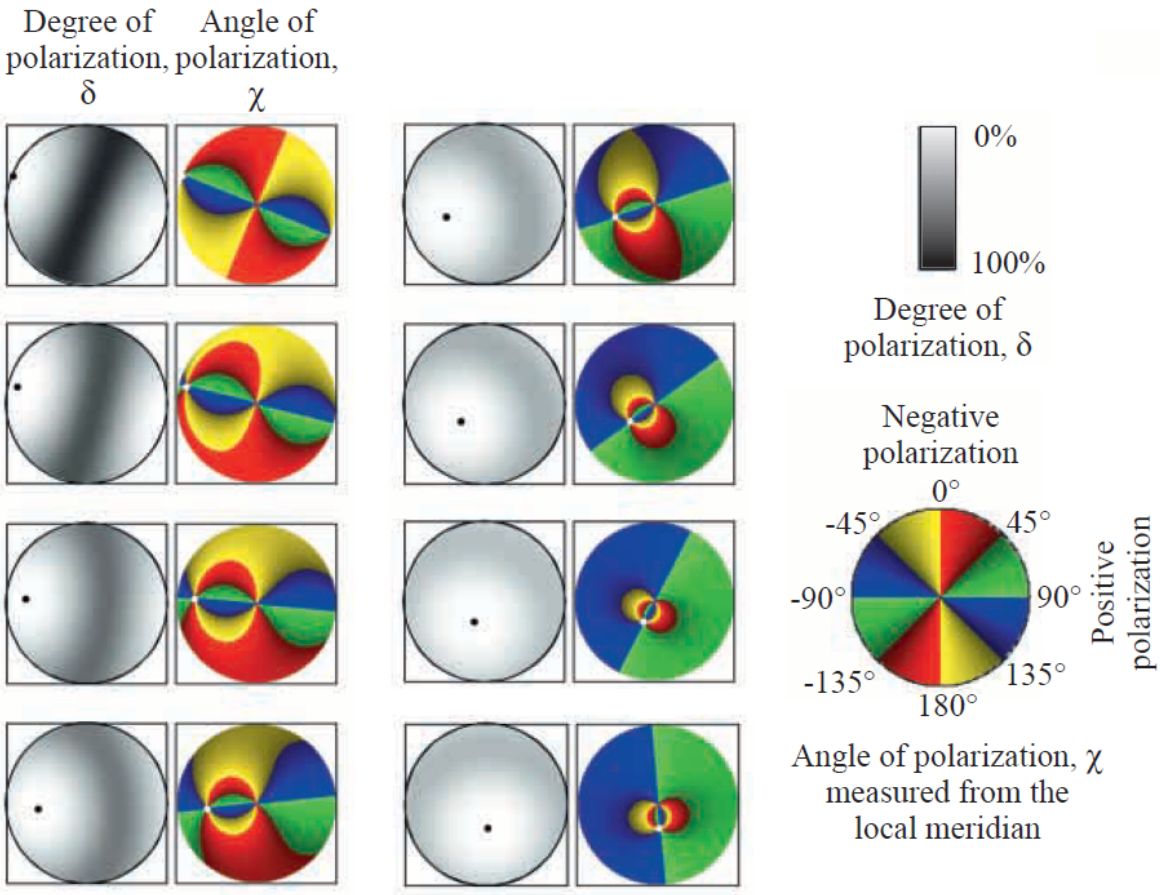

Figure 4.15: Figure by Pomozi et al. (2001) showing the angle of polarization (AoP) and degree of polarization (DoP) patterns of the sky dome in a 2D projection for several solar elevation angles. 90° elevation is in the middle of each plot, note the changing position of the black dot representing the Sun. The DoP is minimum at the Sun and anti-Sun and maximum at 90° away from the Sun and anti-Sun, this is a manifestation of element P_{12} of the Rayleigh scattering matrix depicted in Figure 2.6. The neutral points (points with minimum DoP) are not shifted. They are exactly at the Sun and the anti-Sun under the horizon, this is because these plots represent the single scattering Rayleigh sky. The AoP in these plots is with respect to each local meridian of incoming light (convention **2** in the text), in contrast to Figure 4.14 where the AoP is with respect to the solar meridian.

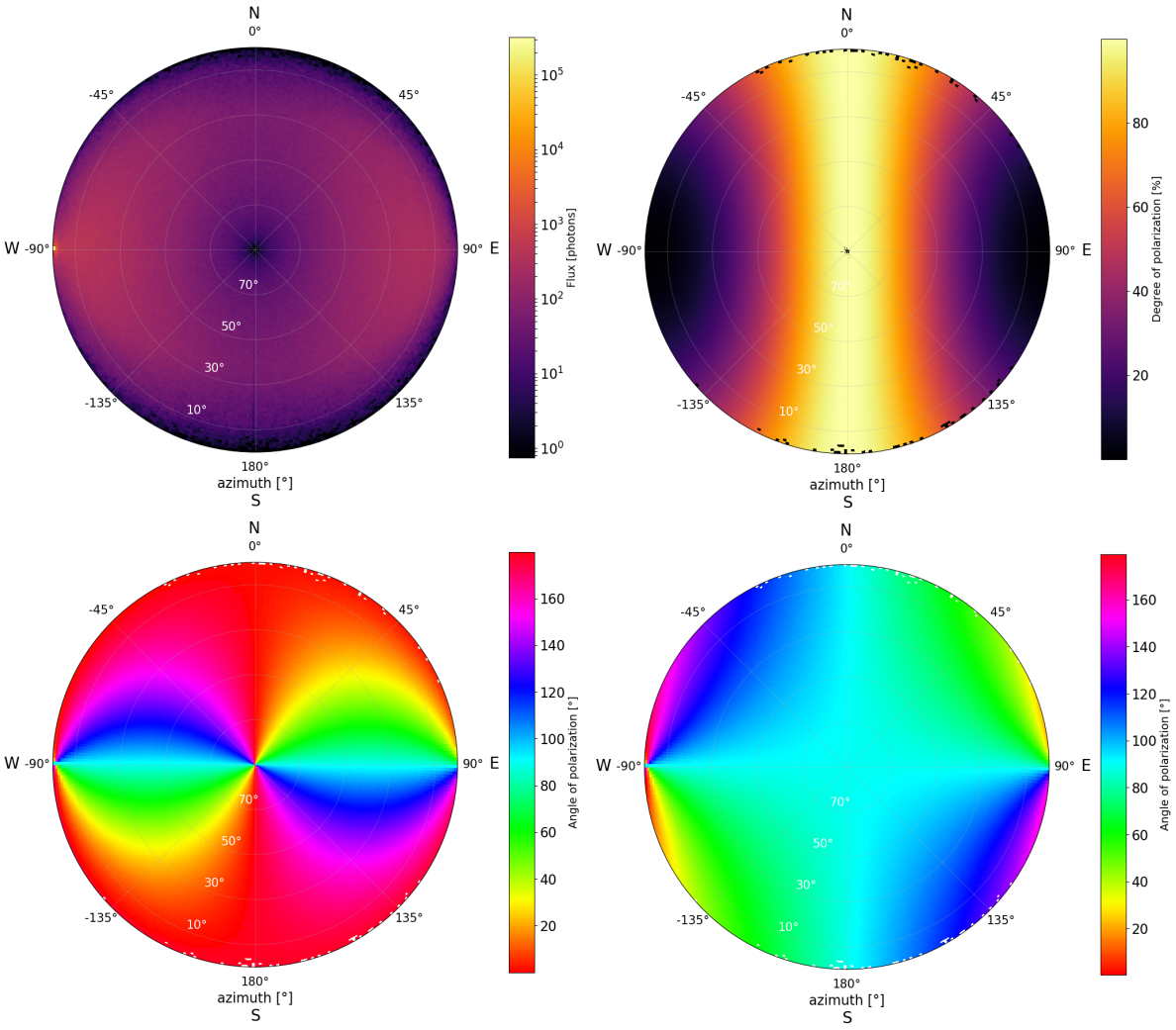

Figure 4.16: Output from PA3S for a *single* scattering Rayleigh sky at a detector near the equator with a solar elevation of 1.5°. Simulations were done with only CO_2 gas present, no dust and no clouds. **Top left**: flux in photons for easy identification of the Sun's position (bright dot in the West). **Top right**: degree of polarization, the pattern matches the patterns presented in Figures 4.14 and 4.15 with the maximum DoP at 90° from the Sun. **Bottom left**: angle of polarization with respect to each local meridian of incoming light at the detector. The pattern matches nicely with at similar elevation of 5° in Figure 4.15. **Bottom right**: angle of polarization with respect to the solar meridian, compare with Figure 4.14. The patterns are very similar apart from a difference in the color spectrum: in Figure 4.14 an AoP of 90° is red while in this figure it is light blue.

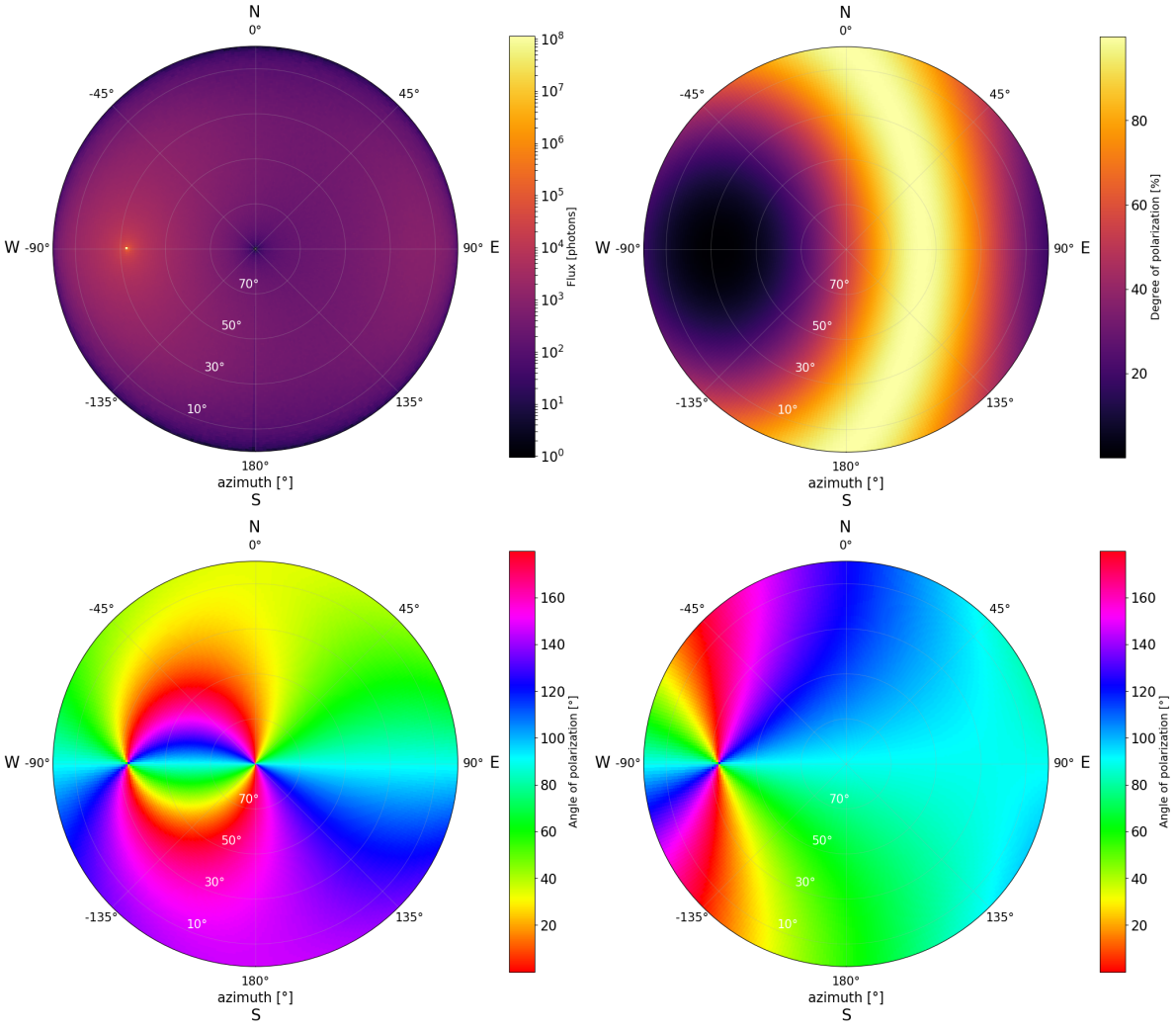

Figure 4.17: Similar to Figure 4.16 but with a solar elevation of 33.5°.

5

Results

In this chapter results, of the PA3S code for simulating Martian ground-based observations are presented. The following sections present results with different combinations of gas, dust and clouds present in the simulation. The simulations with clouds (Sections 5.3 and 5.5) are performed using a size distribution of cubes, i.e. the scattering matrix elements from Figure 3.8. Octahedra and cube-octahedra would give very similar results in the flux, the patterns visible in degree of polarization (DoP) and angle of polarization (AoP) will be different but this does not affect the eventual conclusions in the research. First, in Section 5.1 the layer setup used for most results presented in this chapter is given. Next, Section 5.2 starts with a description of second order Rayleigh scattering effects and discusses whether or not these effect are visible in the Martian atmosphere. The results in Section 5.2 are therefore without dust and CO_2 clouds, only with CO_2 gas. Section 5.3 discusses results for an atmosphere without dust loading, but with a cloud, such results could be compared with clouds in dust loaded scenarios to see the effects of the dust on the cloud signal. Section 5.4 deals with an atmosphere model with only gas and dust and briefly discusses the blue sunsets that occur on Mars. Finally, Section 5.5 gives the results with all constituents present.

5.1. Common simulation settings

Most results in this chapter are generated with the same number of layers and the same CO_2 gas pressure profile shown in Table 5.1, representing the Martian atmosphere under different atmospheric scenarios. These results are shown in Figures 5.5-5.13. Only the results in Figures 5.3 and 5.4 were not generated with these settings, since these results are meant to demonstrate second order Rayleigh scattering neutral points (explained in Section 5.2) in a hypothetical atmosphere with a more optically thick atmosphere compared to that of Mars. Such an atmosphere was necessary because the second order scattering neutral effects are not visible in the Martian atmosphere, as will be detailed in Section 5.2. The CO_2 gas pressure profile in Table 5.1 is based on Table 4.17 from Haberle et al. (2017). All results presented in this chapter are for detectors near the equator with the Sun in the West. Clouds, if present, are set up such that the cloud extends along the solar meridian (in West-East direction) covering all detectors in the twilight zone, see Figure 5.1.

Table 5.1: Settings for the number of layers and the CO_2 gas pressure profile used to generate results presented in Figures 5.5-5.13 (not Figures 5.3 and 5.4). The pressure profile is based on Table 4.17 from Haberle et al. (2017). Layer 1 starts at the surface, the highest layer, in this case layer 5, is always the start of space in PA3S.

layer	**layer start radius [km]**	**CO_2 gas pressure [Pa]**	**τ_{gas} [-]**
1	3389	562	0.0040
2	3392	316	0.0036
3	3399	74	0.001
4	3429	4	0.00006
5 (start of space)	3475	0	0

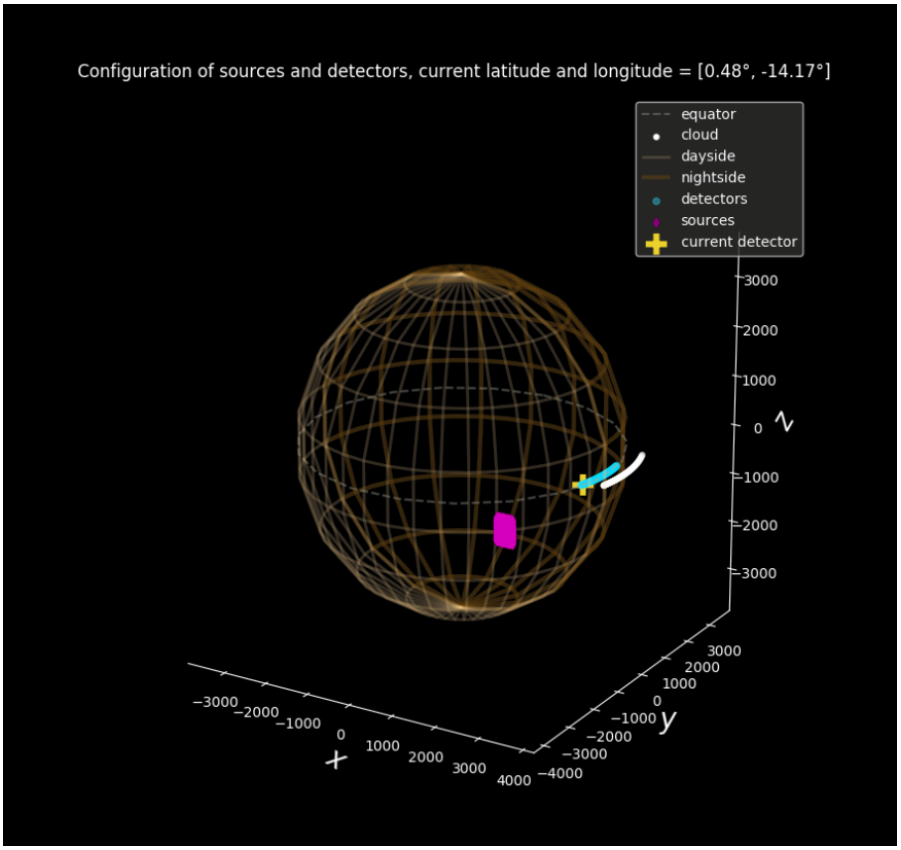

Figure 5.1: Output of a Python script complementary to the main PA3S code, used for the visualization of results and simulation settings. This plot shows the locations of the detectors (blue dots) and the currently selected detector (yellow plus sign), the presence and location of a cloud (white dots) and the extent of the photon point sources for this simulation (purple dots). The settings for simulations in this chapter are similar to those shown in this figure: detectors near the equator, cloud parallel to the direction of direct sunlight and a constrained sources disk to reduce unnecessarily long simulation times.

5.2. Rayleigh scattering neutral points in the Martian atmosphere

Second order Rayleigh scattering effects on Earth are well known and documented, see for example Horváth et al. (1998). It is interesting to see if these effects are also visible in the atmosphere of Mars. Results in this section are with only CO_2 gas present, no dust and no cloud. First, some theory on second order Rayleigh sky effects is given. Next, single scattering and multiple scattering results for a hypothetical atmosphere are presented to demonstrate the difference between the single scattering Rayleigh sky and the sky with second order effects included. This eventually leads to a comparison with results generated with a Mars atmosphere model.

The polarization of the sky differs from the ideal single scattering Rayleigh sky due to the presence of aerosols (that have a different scattering matrix) and multiple scattering. Rayleigh single scattering results in positive polarization, meaning perpendicular to the plane of scattering (the plane containing the observed point and the Sun, see for example Figure 4.14). In the ideal single scattering Rayleigh atmosphere there are two neutral points: one at the Sun and the other at the anti-Sun. See for example the first pair of DoP and AoP plots in Figure 4.15 or Figure 4.16. If enough multiple scattering is present, some negative polarization will be present in the direction of the Sun and anti-Sun. What was formerly one neutral point will split into two regions of zero polarization on the solar meridian, above and below both the Sun and the anti-Sun. These four neutral points follow the movement of the Sun in the sky. With increased atmospheric optical thickness their distance from Sun and anti-Sun increases since the amount of multiple scattering increases with increased optical thickness. This phenomenon is most evident at low elevations where incoming photons have had a longer path through the atmosphere.

The neutral points are called the Arago, Babinet and Brewster neutral points (the fourth neutral point is

unnamed). See Figure 5.2 from Horváth et al. (1998). On Earth the Arago point is located approximately 20°-30° above the antisun. The Babinet point is around 25°-30° above the Sun. Finally, the Brewster point is 25°-30° below the Sun. The fourth neutral point is only visible from high altitudes or from space because it is below the anti-Sun. It has been observed from a hot air balloon by Horváth et al. (2002). Only two of the neutral points can be visible at one time: Arago-Babinet or Babinet-Brewster. More details on these neutral points can be found in Horváth et al. (1998).

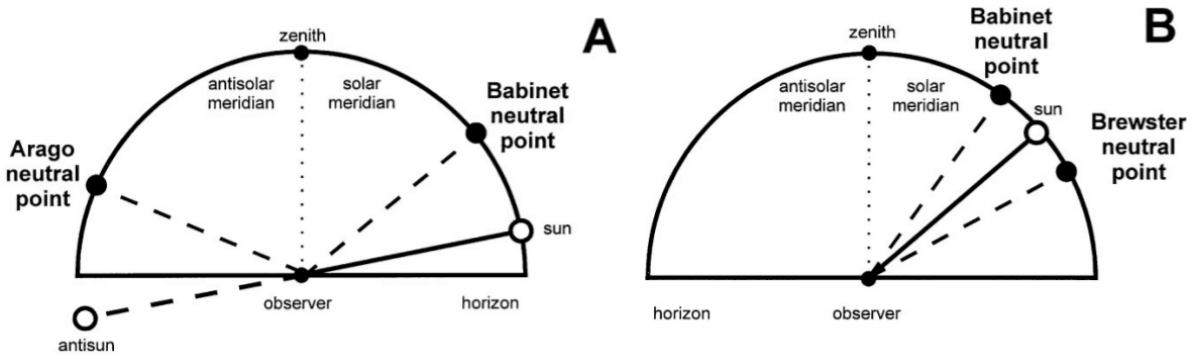

Figure 5.2: Figure by Horváth et al. (1998) showing the three neutral points caused by second order Rayleigh scattering, the fourth neutral point is not shown. **A** shows Arago-Babinet, **B)** shows Babinet-Brewster. The neutral points form when the single neutral points at the Sun (and anti-Sun) splits into two points, the points follow the Sun along its path over the sky dome. Only two neutral points are visible at the same time. The more optically thick the atmosphere, the further the away the neutral points are from their original position at the Sun and anti-Sun.

Figures 5.3 and 5.4 show the AoP and the DoP, respectively, in the sky in a rectangular projection for comparison of the polarization pattern of respectively single scattering (top) and multiple scattering (bottom) situations. The figures compare the AoP and the DoP of two runs, the top plots show results of a run with maximum number of scattering set to 1, bottom plots are the AoP and the DoP for a run with maximum number of scattering set to 8. The simulations were done with CO_2 gas, without dust, without clouds for the same atmosphere, two layers with total optical thicknesses: $\tau_1 = 0.27$ and $\tau_2 = 0.017$. These values are far higher than the optical thickness of the clear Martian atmosphere, which is around 0.01 for $\lambda = 0.4$ μm and 0.00065 for $\lambda = 0.8$ μm. The Sun is due West in both figures at 6.5° elevation. Multiple scattering (bottom plots) is clearly characterized by a more fuzzy picture compared to single scattering. With single scattering, photons from a certain direction can have followed only one path. With multiple scattering included there is more randomness.

The AoP in Figure 5.3 is with respect to the local meridian, the color coded angles are with respect to the vertical. It is visible that the clear neutral point at the Sun (90° West) in the top plot has been replaced by a band of vertically polarized photons (red) in the bottom plot. The neutral point in the West has shifted up a few degrees elevation, corresponding to the Babinet point from Figure 5.2. In the East the Arago point is not indistinguishable, the atmospheric optical thickness is not high enough to shift the Arago point above the horizon.

In both plots in Figure 5.4 values larger than 8% have been cut off for more color resolution in the areas with low DoP. Due West it is visible that the area with low DoP is stretched out to higher elevations in the bottom plot compared to the top plot. In the anti-Sun's half of the sky (East) the area with low DoP is also higher at higher elevation in the bottom plot than in the top plot. These stretched out areas of low polarization correspond with the Arago and Babinet neutral points from Figure 5.2.

See Figure 5.5 for the AoP and the DoP results using the Martian atmosphere model from Section 5.1. No effects similar to the bottom plots in Figures 5.3 and 5.4 is visible. The Martian atmosphere is too thin too observe neutral points caused by second order Rayleigh scattering.

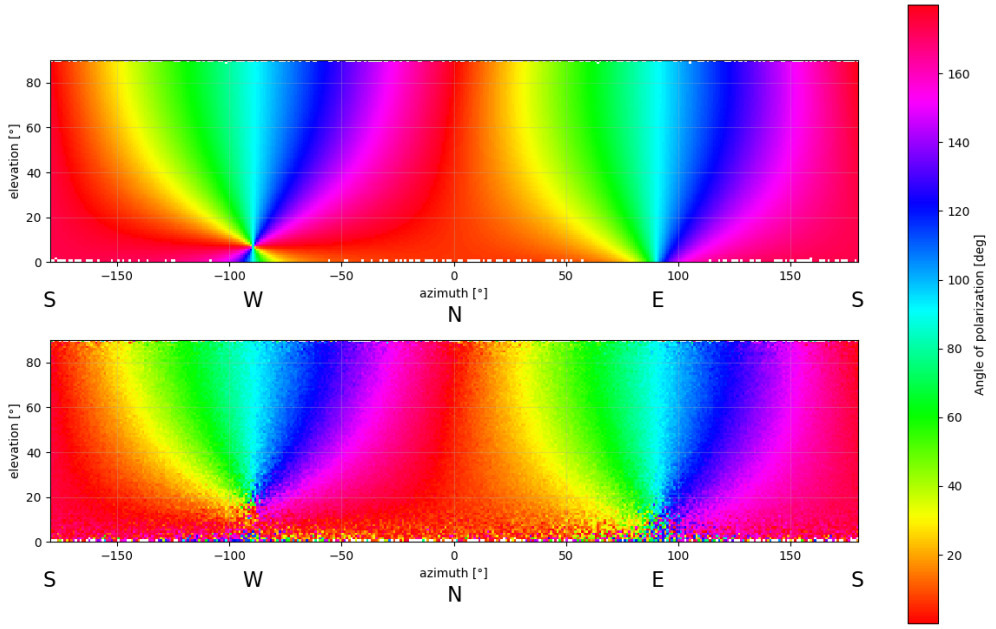

Figure 5.3: Comparison of angle of polarization for an ideal single scattering Rayleigh sky (top) and multiple scattering sky (bottom). The AoP is with respect to the local meridian (convention **2** in Chapter 4). In this rectangular projection, the meridians correspond to the vertical at each respective azimuth. Thus, the color coded angles are with respect to the vertical (red is 0° or 180° and therefore vertical, light blue is 90° and horizontal). Both plots are generated for the same solar elevation of 6.5° with the same atmosphere model: 2 layers, $\tau_1 = 0.27, \tau_2 = 0.017$. A clearly defined neutral point is present at the position of the Sun (90° West). The bottom plot is more noisy because the photons are allowed to scatter more than once. Looking in the direction of the Sun, a vertically polarized band is visible. Instead of a clearly defined neutral point at the Sun at 6.5° as in the top plot, a more hazy neutral point forms a few degrees above. This corresponds to the Babinet point in Figure 5.2. The same type of band is seen forming in the direction of the anti-Sun (90° East), but no clear neutral point can be distinguished. The atmosphere is not yet optically thick enough to shift the Arago point (see Figure 5.2) above the horizon.

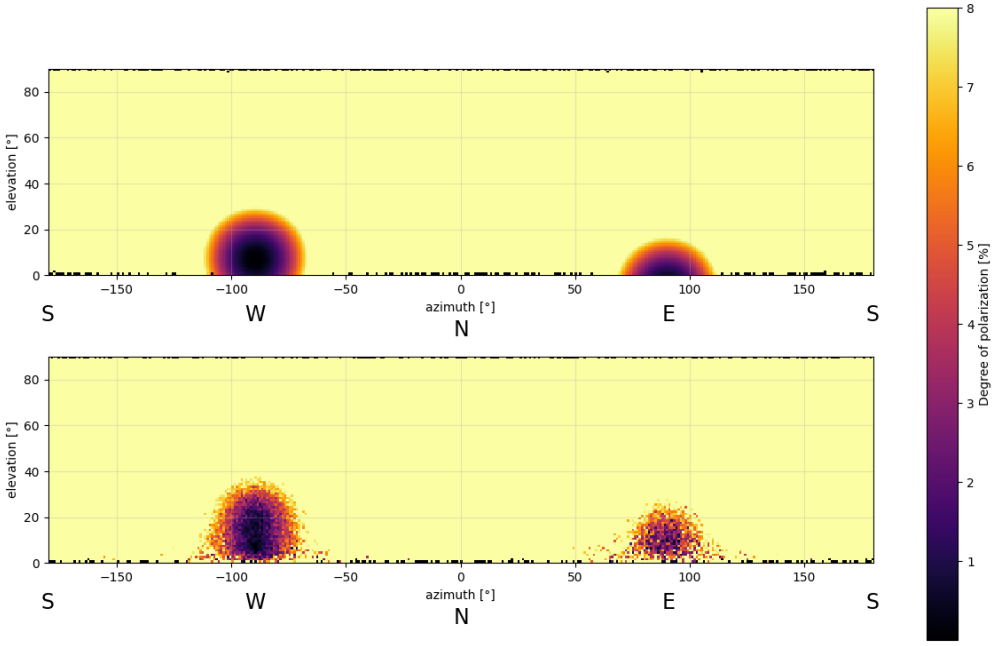

Figure 5.4: Similar to Figure 5.3 but for degree of polarization. The DoP values are capped at 8% to achieve better color resolution in low-DoP areas. A neutral point is present at the position of the Sun (90° West) in the top plot. The bottom plot is more noisy because the photons are allowed to scatter more than once. The area of low polarization (<1%) is stretched out to higher elevation in the bottom plot compared to the top plot. This area corresponds to the Babinet point in Figure 5.2. The same type of stretching of the low polarization area is happening in the direction of the anti-Sun (90° East) altough less clearly. The atmosphere is not yet optically thick enough to shift the Arago point (see Figure 5.2) above the horizon.

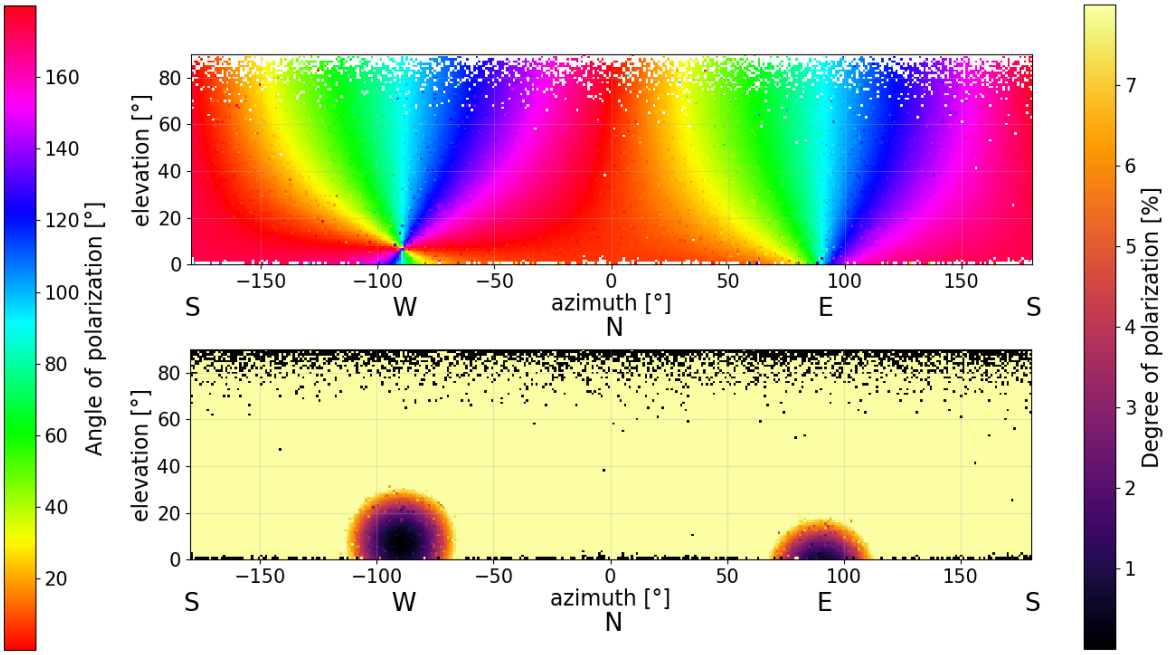

Figure 5.5: The AoP (top) and the DoP (bottom) for the simulated Martian atmosphere (settings from Section 5.1) at solar elevation angle of 6.5°. Compare with Figures 5.3 and 5.4, none of the effects seen in the bottom plots in those figures can be discerned in this figure. The Martian atmosphere is too thin to observe neutral points caused by second order Rayleigh scattering.

5.3. With ice clouds, without dust

In this section, results are presented for a Martian atmosphere with an ice cloud, but without dust. This is not a realistic scenario as the optical thickness of the entire atmosphere on very clear days is rarely below 0.2, see Figure 2.9. Nevertheless, it is useful to know what a clear observation of the clouds would look like for comparison with more realistic simulations. Note that in the presence of a cloud, the positions of the detectors with respect to the cloud are different for every detector, resulting in different viewing geometries. A way to handle this is by defining a long cloud covering all the detectors. The results are given for one wavelength, 0.4 μm. Figure 5.6 shows the flux (top-left), the DoP (top-right) and the AoP (bottom) of a cloud that is only 6 m in vertical extent with the Sun at 2.5° solar elevation. The results indicate that without the dust, such a thin cloud would have been visible easily, even when the Sun is still above the horizon. Looking at the flux in Figure 5.6, the shape of the phase function for a size distribution of cubes (blue P_{11} plot in Figure 3.8) in blue is discernible. The cloud exhibits strong forward-scattering, a wavy pattern for mid-range scattering angles and a slight back-scattering peak. In the DoP a barcode-like pattern is visible. Octahedra and cube-octahedra would show a different type of barcode-like pattern. In regions in the sky dome were the cloud is not present, the DoP pattern of a Rayleigh sky is visible. In Figure 5.6, the AoP of the cloud shows a discontinuous pattern. These discontinuities coincide with bands in the cloud where the DoP of the cloud is smaller than the background DoP of the CO_2 gas and therefore the AoP of the gas is observed.

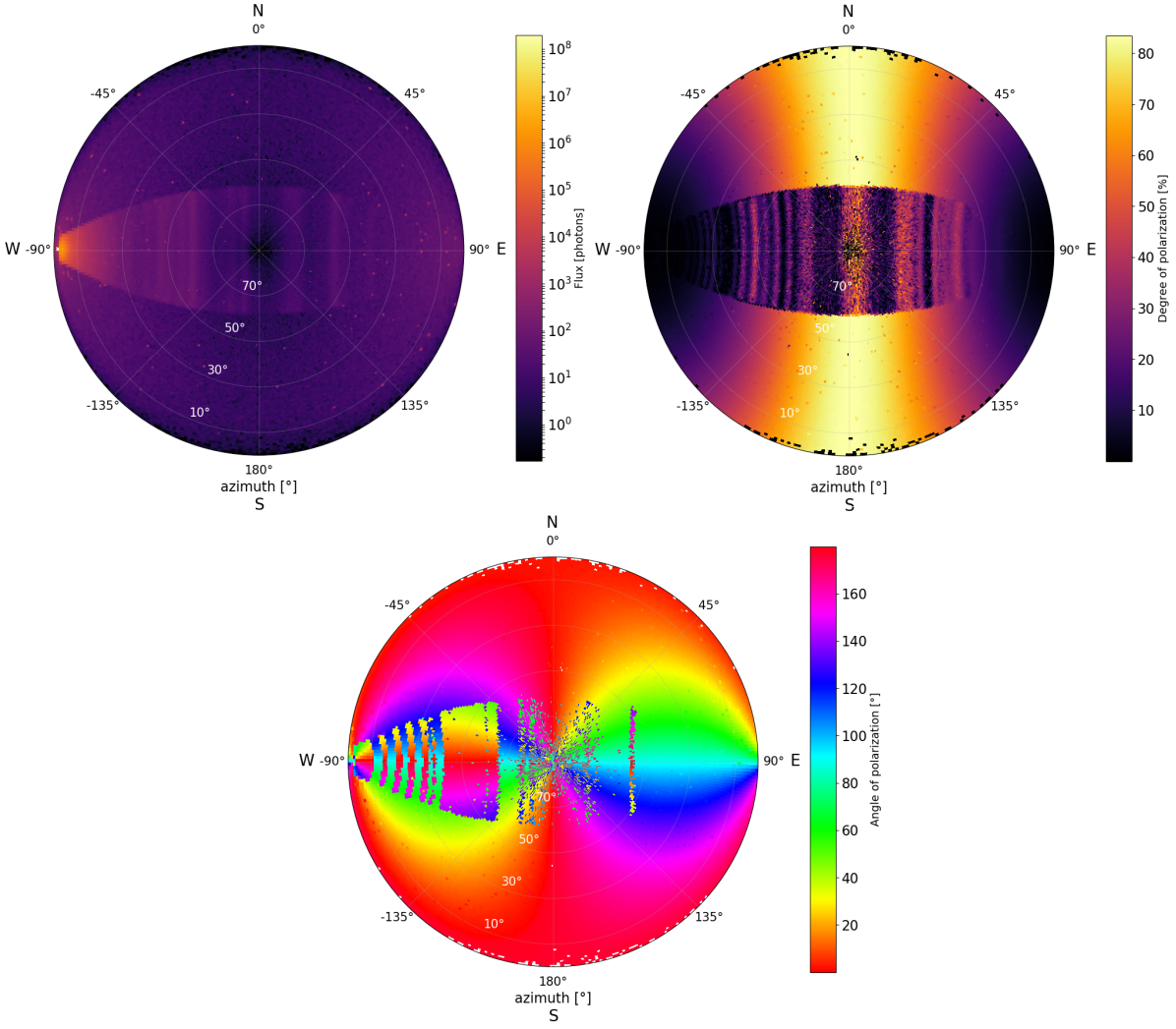

Figure 5.6: PA3S results for an atmosphere without dust loading, with CO_2 gas and a cloud present. Flux (top-left), the DoP (top-right) and the AoP (bottom) of a cloud that is 6 m in vertical extent are presented. The results have been generated for a size distribution of cubes at 0.4 µm and the Sun is at 2.5° solar elevation. These atmospheric conditions are not realistic, the background dust optical thickness is rarely less than 0.2, see Figure 2.9. The figure serves to demonstrate the patterns in flux, the DoP and the AoP caused by the CO_2 ice particles in the sky.

5.4. Cloudless, dusty atmosphere and blue Martian sunsets

This section presents results for an atmosphere with gas and dust, without clouds. Also, it is investigated whether or not the blue sunsets that are known to occur on Mars can be simulated with PA3S. The wavelengths at which the results has been generated are slightly different than in the other sections in this chapter: 0.45 μm (blue), 0.55 μm (green) and 0.68 μm (red). Unlike the wavelengths used in the other sections, these wavelengths roughly correspond to actual blue, green and red light. In Figure 5.7, a setting Sun is presented in blue (left) and red (right). The figure demonstrates how the daytime Martian atmosphere is brighter in red than in blue, leading to the orange-brown sky color atmosphere. This effect is caused by the stronger scattering of red light and higher absorption of blue light.

Results of the red, green and blue channels have been combined to create a true color approximation of the Martian atmosphere during sunset. See Figure 5.8 for the RGB color composites in two dust loading scenarios, the top plot is for $\tau_{tot} \approx 0.2$ (τ_{tot} is actually wavelength-dependent but this is just for an indication) and $\tau_{tot} \approx 0.4$. In the bottom plot, the Sun disk is obscured more by the dust than in the top plot, resulting in a larger bright patch, whereas in the top plot the bright area is more concentrated near the Sun. Red dominates in both plots, but in the direction of the Sun the sky is whiter. This makes sense since blue and green are scattered less than red, they will be relatively stronger in the region near the Sun. No blue sunset is visible however. According to Ehlers et al. (2014), an important factor causing the blue Martian sunsets is the wavelength dependence of the Martian dust scattering matrix. In this research the wavelength dependence of the dust scattering matrix has not been implemented, see Figure 2.6. Ehlers et al. (2014) state that Martian dust shows stronger scattering of blue light compared to red light at small scattering angles. This added increase in ”blueness” would probably turn the white areas in Figure 5.8 into a light-blue.

In Figure 5.9, the AoP (top) and the DoP (bottom) patterns of a dusty atmosphere without clouds are given at a solar elevation of 30°, the Sun is at 90° West. The AoP pattern is similar to that of CO_2 gas but much more noisy because of the presence of multiple scattering. In the bottom plot, it is interesting to note the orange band in the eastern part of the sky with a $DoP > 10\%$. This result corresponds to element P_{12} of the dust scattering matrix. See Figure 2.6, P_{12} shows a shallow valley that peaks at a scattering angle of roughly 100°.

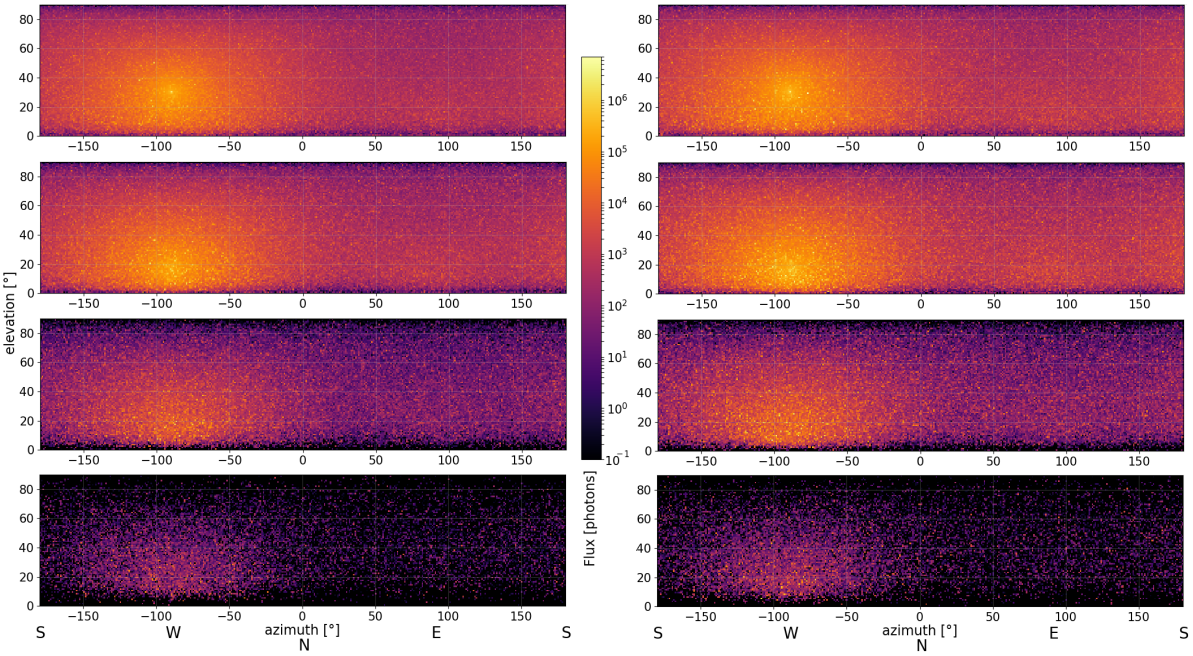

Figure 5.7: Flux results for simulations without clouds with a fairly heavy dust loading. The left set of plots is in blue (0.45 µm), the right set of plots is in red (0.68 µm). From top to bottom the solar elevation angles of the plots are: 30°, 15°, 0° and -7.5°. Both simulations were done with the same number of photons and with the same dust mixing ratio profile, see Section 2.5. However, because of the different Q_{ext} of the two wavelengths, (see Figure 2.8) the optical thicknesses resulting from Equation 2.24 will not be equal. Red light will scatter more often than blue light, $\tau_{tot,blue} = 0.426$, $\tau_{tot,red} = 0.500$. Also, blue light is absorbed more than red light, $a_{blue} \approx 0.8$, $a_{red} \approx 0.97$. These wavelength dependencies of dust optical thickness and single scattering albedo cause the Martian atmosphere to be brighter in red than in blue. However, at low solar elevation angles, the prevalence of red over other wavelengths (especially blue) is weaker in the area near the Sun, causing the Martian sunset to be a bluish white. The effect is very faintly visible in this figure. Because a logarithmic scale is used, flux values at the same order of magnitude are mapped to similar color values rendering the right set of plots only slightly brighter than the left set. See Figure 5.8, which is a composite image made from blue, green and red channels where the aforementioned effect is better visible.

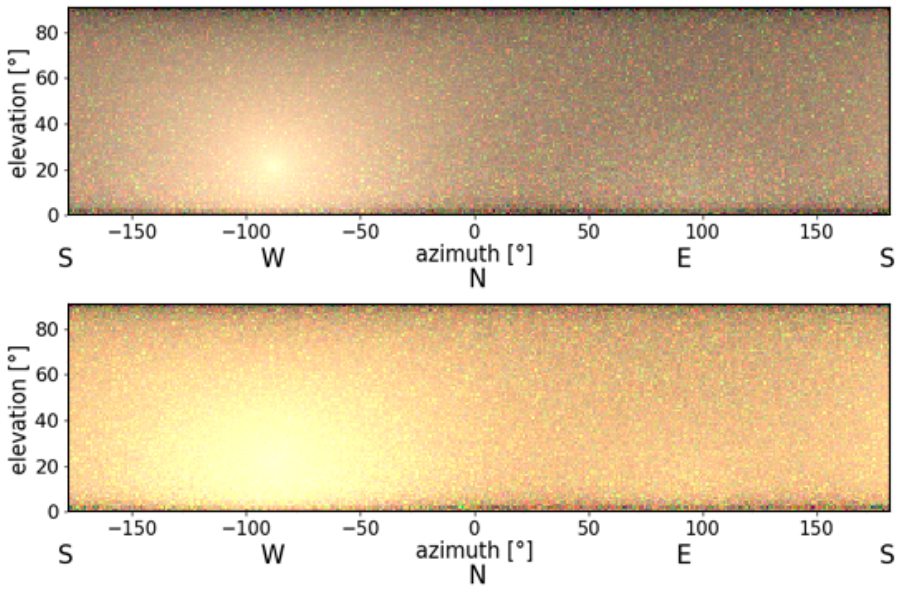

Figure 5.8: Composite image made by combining three channels: 0.45 µm (blue), 0.55 µm (green) and 0.68 µm (red). The top plot is at lower dust loading, roughly for $\tau_{tot} \approx 0.2$ and the bottom plot is for $\tau_{tot} \approx 0.4$. Actually τ_{tot} is different for each wavelength resulting in the reddish color. The Sun is obscured more by a bright haze in the bottom plot. Whitening of the area around the Sun is clearly visible, due to the presence of more blue and green light coming from these directions compared to other parts of the sky. However, no bluish color is visible, this is probably because the wavelength dependence of the dust scattering matrix was not taken into account in this research. Ehlers et al. (2014) state that such a dependency explains the white-bluish color of the Martian sunset. The RGB coloring scheme capped flux values above a certain threshold. Subsequently, the flux values of each channel were mapped to grey-scale and the grey-scale values of each pixel were scaled such that the ratios of RGB values correspond to the ratios of the original flux values in red, green and blue. The threshold was set at $1 \cdot 10^5$ photons. With a different total number of photons this threshold would have to be different to produce the same plots and changing the threshold has a strong influence on the eventual color. Thus, even though these figures are very reminiscent of the Martian atmosphere, they only indicate that red light scatters more in the PA3S simulation as expected.

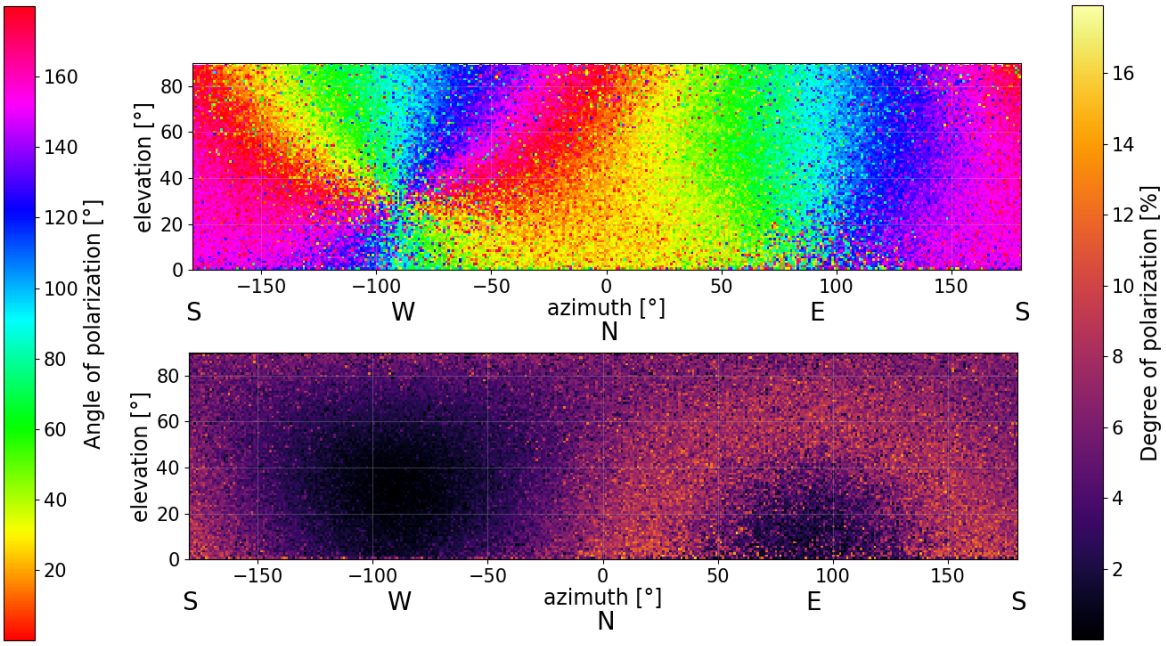

Figure 5.9: AoP (top) and DoP (bottom) patterns in a dusty Martian atmosphere without clouds. The plots are given at a solar elevation of 30°, the Sun is at 90° West. The AoP pattern is similar to that of CO_2 gas but much more noisy because of the presence of multiple scattering. In the bottom plot, it is interesting to note the orange band in the eastern part of the sky with $DoP > 10\%$. This result corresponds to element P_{12} of the dust scattering matrix. See Figure 2.6, P_{12} shows a shallow valley that peaks at a scattering angle of roughly 100°.

5.5. With clouds, with dust

Simulations with dust and clouds included showed that even at low dust loading scenarios (total vertical $\tau_{dust} \approx 0.2$) the CO_2 ice clouds will not be visible during the day, shown in Subsection 5.5.2. However, the simulations suggest that the CO_2 ice clouds *will* be visible during twilight.

In this section, first, the flux and the DoP of simulated mesospheric clouds are presented for four different scenarios corresponding to different optical thicknesses of the cloud and the dust. Subsequently, results for the best scenario and wavelength are shown for a simulation with a high total amount of photons, $1.7 \cdot 10^{12}$.

5.5.1. Results for different atmospheric conditions and wavelengths

The four scenarios considered in this subsection are:

1) $\tau_{cloud} = 0.1$, $\tau_{dust} \approx 0.2$, Figure 5.10.

2) $\tau_{cloud} = 0.1$, $\tau_{dust} \approx 0.4$, Figure 5.11.

3) $\tau_{cloud} = 0.3$, $\tau_{dust} \approx 0.2$, Figure 5.12.

4) $\tau_{cloud} = 0.3$, $\tau_{dust} \approx 0.4$, Figure 5.13.

In each of Figures 5.10-5.13 results are shown for these scenarios at three wavelengths: 0.4 (top), 0.6 (middle) and 0.8 (bottom) μm, referred to as blue, green and red. The dust optical thicknesses are actually wavelength dependent (see Sections 2.5 and 5.4) and deviate slightly around the values $\tau_{dust} = 0.2$ and $\tau_{dust} = 0.4$ for each wavelength. Nevertheless, the mixing ratio profiles were the same for each wavelength, thus values 0.2 and 0.4 are just used to distinguish between scenarios with different mixing ratio profiles. The cloud optical thicknesses were based on the analysis by Määttänen et al. (2010). In contrast to τ_{dust}, the cloud optical thicknesses, τ_{cloud}, are given the same value for each wavelength. The cloud scattering matrices that have been used are for size distributions of cubes and have been calculated with methods described in Chapter 3, corresponding scattering matrix elements are presented in Figure 3.8. Based on conclusions made in Section 3.5, the single scattering albedo of the clouds, a_{cloud} was taken as 1.0.

The clouds in all figures are clouds that are 0.1 km in vertical extent at an altitude of 70 km. The vertical extent of the cloud is important in the PA3S algorithm, see Subsection 4.3.5. According to Dowling and Radke (1990), on Earth, cirrus clouds have typical values of 1.5 km and usually range between 0.1 km to 8 km in vertical extent. Määttänen et al. (2010) state that they found in their analysis that Martian mesospheric CO_2 ice clouds range between 5 to 10 km in vertical extent, though they are not clear whether this refers to the more common cirrus clouds or less common cumulus clouds. Thus, 0.1 km is taken as a conservative value for the vertical extent, representing cirrus-like mesospheric CO_2 ice clouds. Figures 5.10-5.13 are all for a solar elevation of -9.5°. In most scenarios, the clearest cloud signal could be seen in at this solar elevation. From the plots, it is evident that the cloud DoP pattern is best visible in blue wavelengths. Especially in red, the cloud signal stands out better in lower dust loading scenarios, compare the bottom plots of Figure 5.10 with 5.11 and the bottom plot of Figure 5.12 with 5.13. In blue, the cloud signal is less sensitive to dust loading because blue is scattered less than green and red, resulting in more direct, blue light hitting the clouds. This is in line with the reasoning in Section 5.4. In all cases, the clouds are more easily detected in the DoP than in the flux.

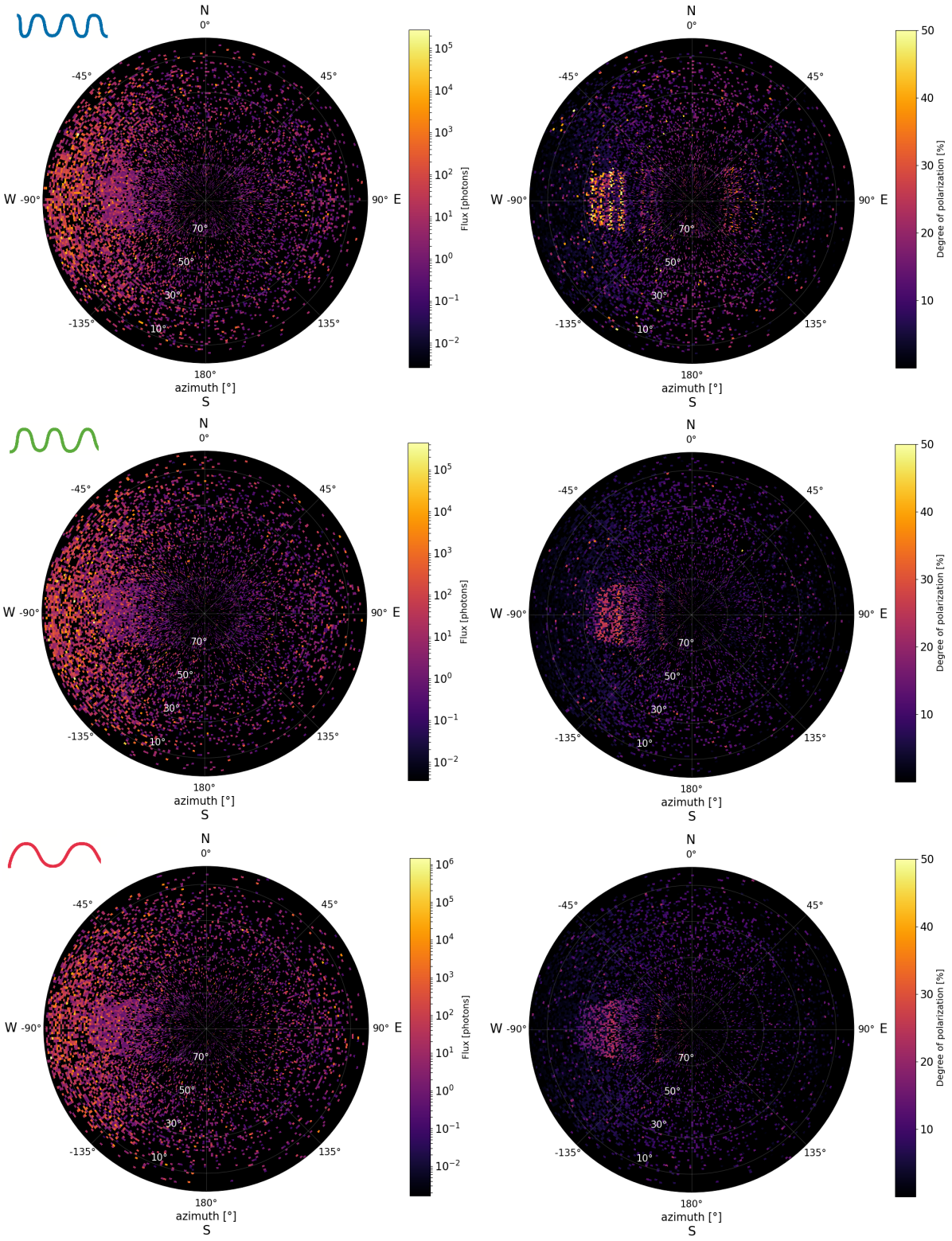

Figure 5.10: PA3S results with dust loading included and a 100 m thick CO_2 cloud present at 70 km altitude. The cloud is parallel to the West-East meridian and part of it is visible in the sky plots as a faint, broad band running from West to East. The left plots give the flux in photons and the right plots show the DoP. These results are all generated in the twilight zone at a solar elevation of -9.5°, given at three wavelengths in the visible spectrum: 0.4 (top), 0.6 (middle) and 0.8 (bottom) µm. The layer settings and CO_2 gas pressure profile settings were according to Table 5.1. The cloud optical thickness and dust loading correspond to scenario **1** from the text: $\tau_{cloud} = 0.1$, $\tau_{dust} \approx 0.2$.

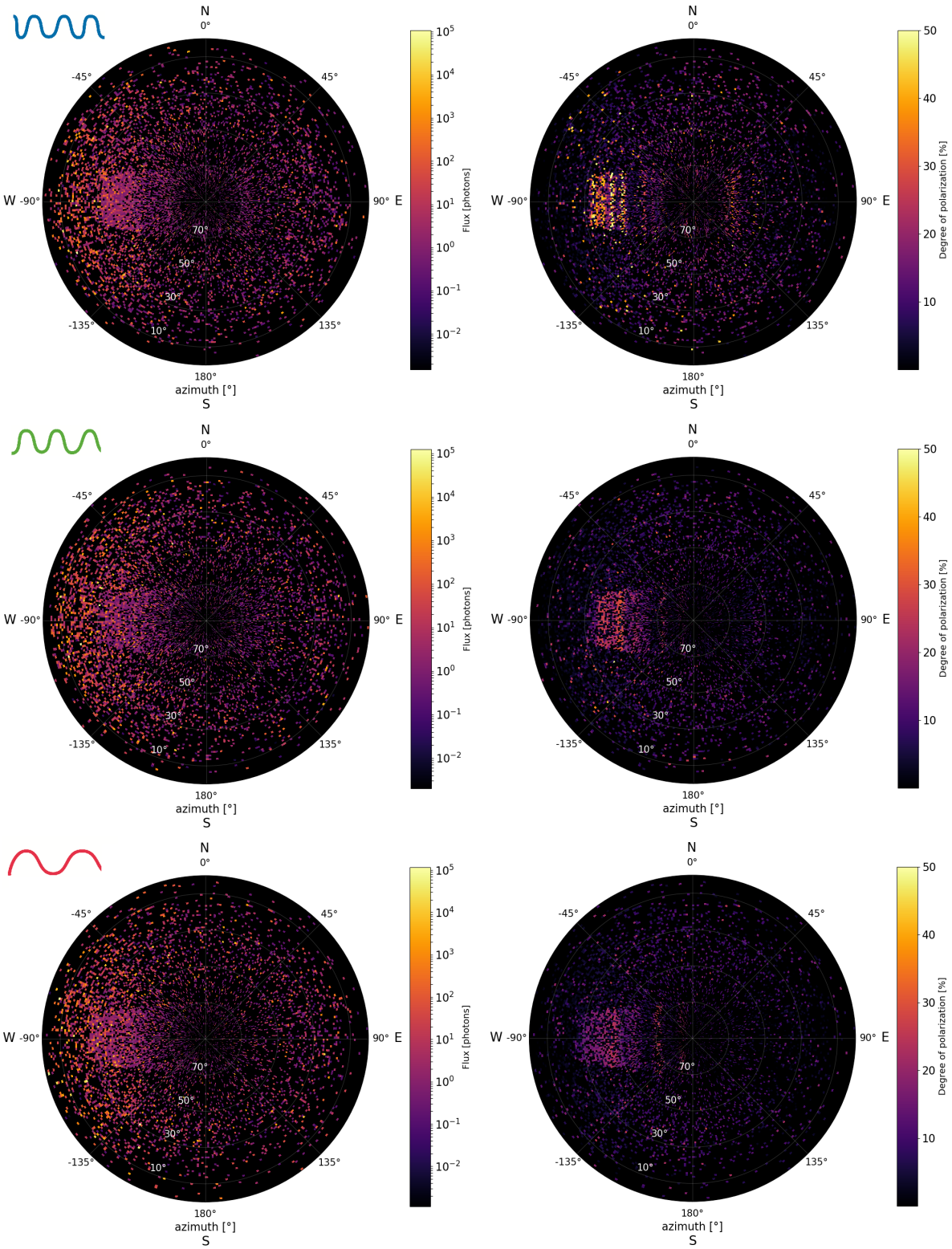

Figure 5.11: Similar to Figure 5.10 but with scenario **2** from the text: $\tau_{cloud} = 0.1$, $\tau_{dust} \approx 0.4$.

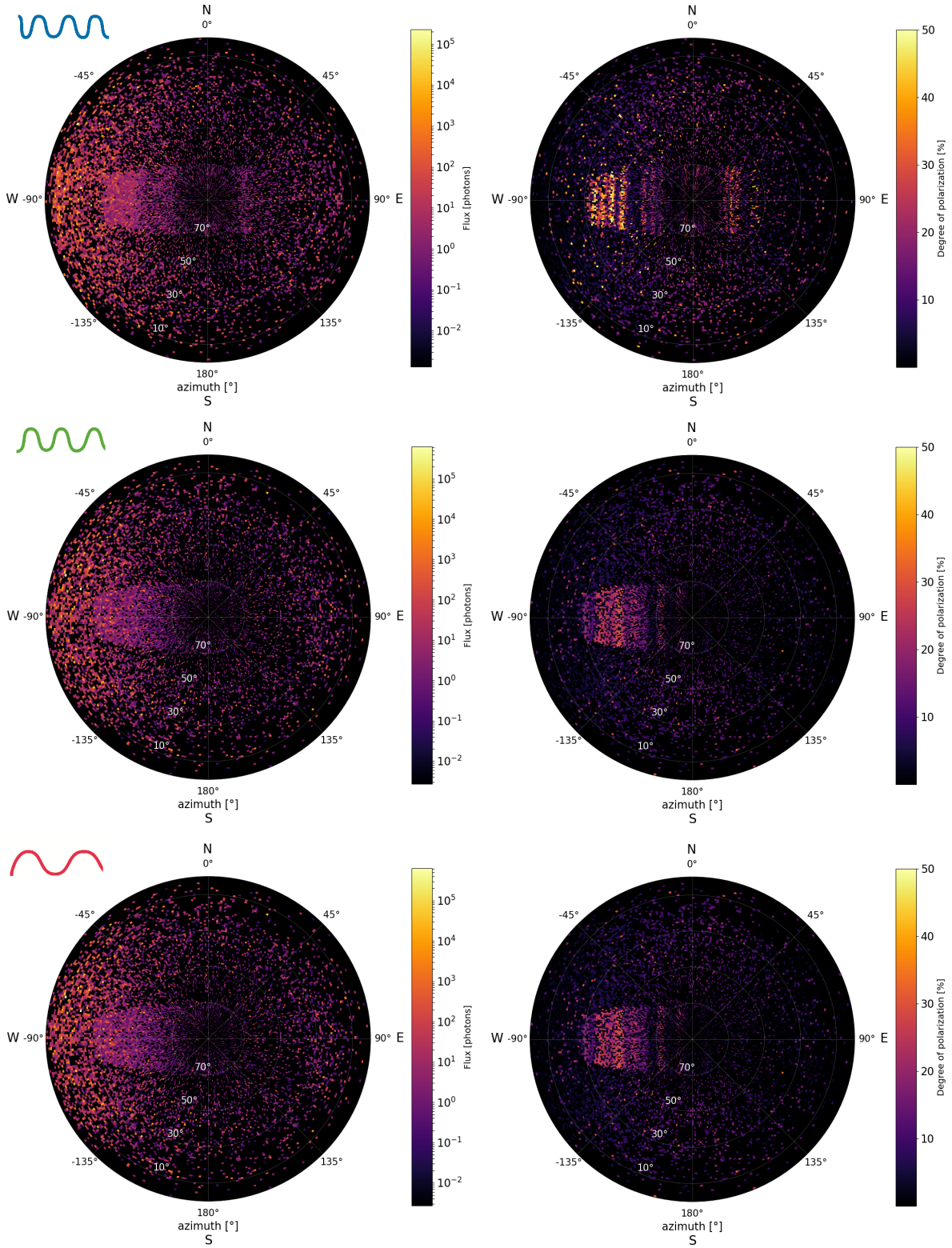

Figure 5.12: Similar to Figure 5.10 but with scenario **3** from the text: $\tau_{cloud} = 0.3$, $\tau_{dust} \approx 0.2$.

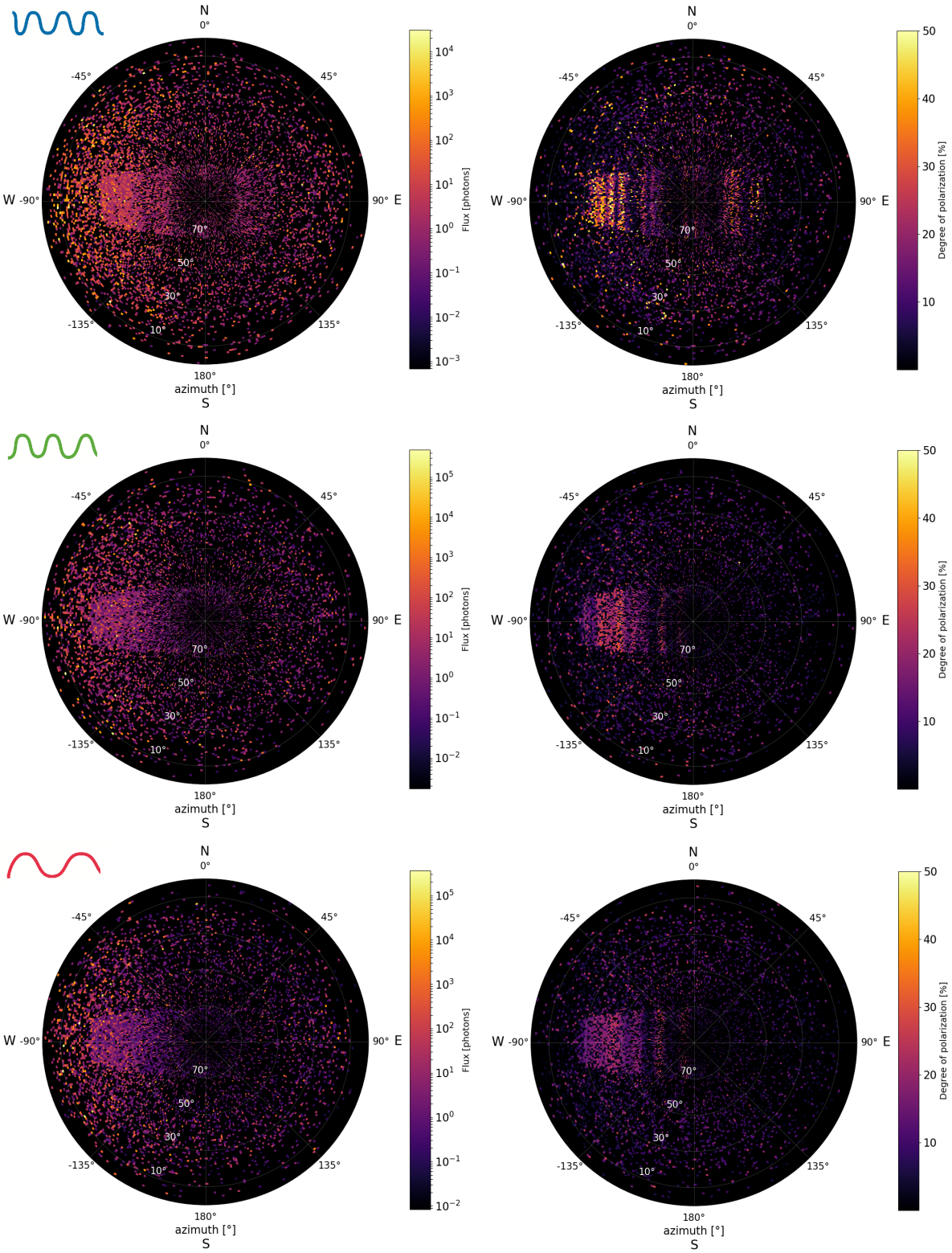

Figure 5.13: Similar to Figure 5.10 but with scenario **4** from the text: $\tau_{cloud} = 0.3$, $\tau_{dust} \approx 0.4$.

5.5.2. Results in blue with a large number of photons

Figures 5.10-5.13 serve the purpose of identifying the best wavelength and atmospheric conditions, these are: blue (0.4 μm), $\tau_{cloud} = 0.3$ and $\tau_{dust} \approx 0.2$. With these settings and the same cloud of 100 m in vertical extent, another simulation was done with a high total number of photons, $1.7 \cdot 10^{12}$. The flux, the DoP and Q and U Stokes parameters of this simulation run are presented in Figure 5.14 for $\theta_S = -9.5°$. From the flux plot (top left) it is clear that a sufficient number of photons has reached the detector, but no cloud is visible in the flux. In the DoP (top right) a cloud signal is discernible along the solar meridian (along West-East direction) starting around 60° elevation in the Western sky until roughly 50° elevation in the Eastern sky. The strongest cloud DoP is near 50° elevation in the East with a value of approximately 20%. The bottom plots in Figure 5.14 show the Q and U signals, respectively. The cloud Q and U signals are relatively weak compared to the strongest Q and U in the sky due to the dust, coming from the West. The cloud Q varies between being one to two orders of magnitude weaker than the dust Q in the West. It seems that the high cloud DoP at 50° elevation in the East is mainly because of the contribution by Q. The U signal of the cloud is weaker; it is two orders of magnitude weaker than the strongest dust U in the West, without any significant peak value. However, a faint barcode pattern is visible at careful inspection. Even though the cloud's Q and U signals are fairly weak, the cloud is still distinguishable in the corresponding DoP signal at high elevations in the East and West because the background signal is weak in this directions. It should be noted though that the low number of photons of the Q and U signals is important to consider during instrument design.

Figures 5.15 and 5.16 show the same flux and DoP results of blue light from Figure 5.14, but depicted only along the solar meridian for several solar elevation angles, θ_S. In the 2D projections of the sky dome in Figure 5.14, the solar meridian corresponds to a line connecting 90° West and 90° East. At $\theta_S = 5.5°$ and $\theta_S = 15.5°$, the cloud is not visible in neither the flux nor the DoP. In the twilight zone, at $\theta_S = -9.5°$, the cloud is still not detectable in the flux, but it is visible in the DoP. The observed DoP along the solar meridian starts to vary strongly in the range of zenith angles between -30° and +50° compared to the DoP at $\theta_S = 5.5°$ and $\theta_S = 15.5°$: between 0 and 20% (corresponding elevations are between 60° in the East and 40° in the West). This range in zenith angles is analogous to a range of scattering angles between 60° and 140°.

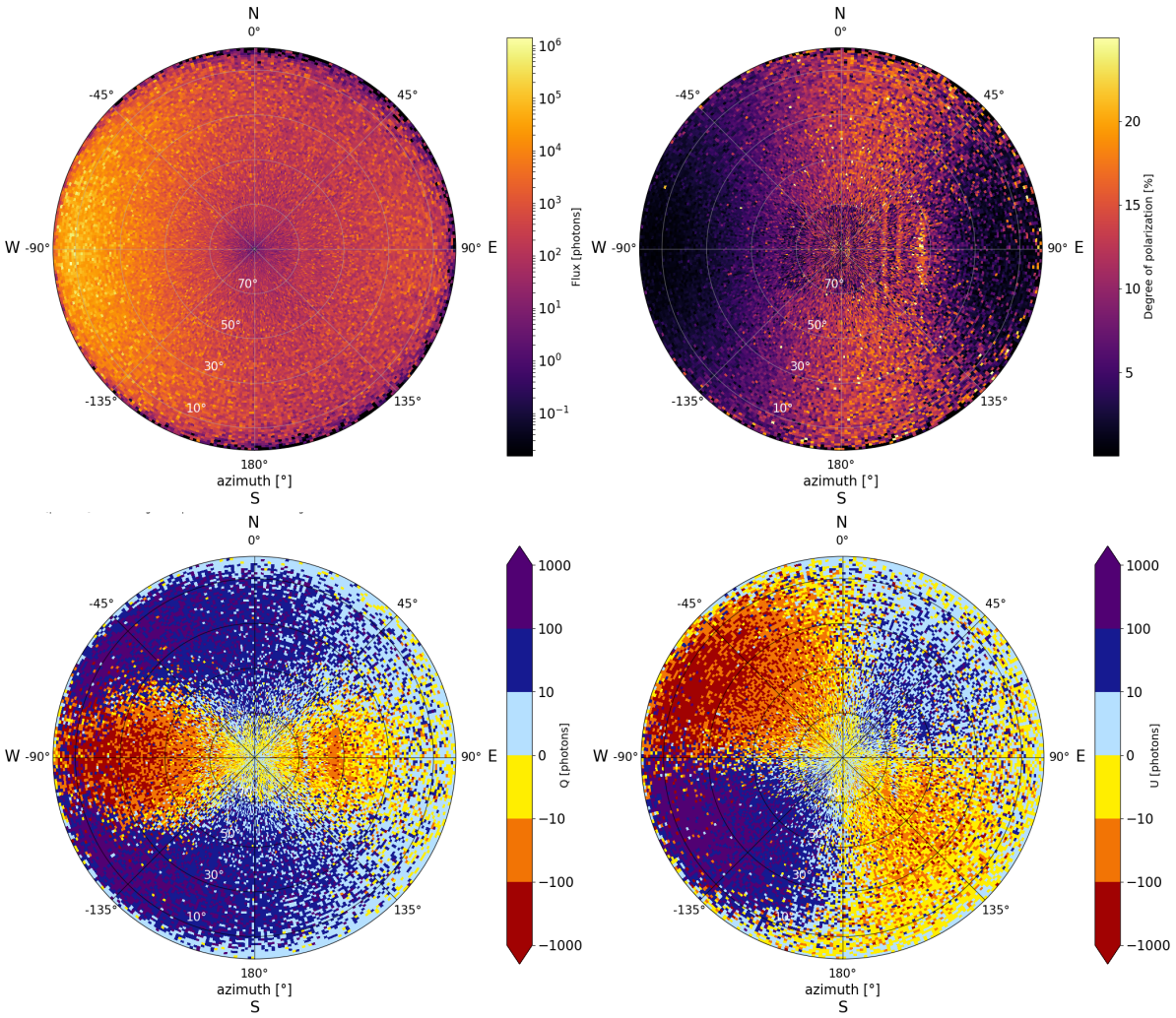

Figure 5.14: PA3S results in blue in the twilight zone at solar elevation angle of -9.5° for a long run with $1.7 \cdot 10^{12}$ photons. The simulation was performed with dust optical thickness $\tau_{dust} \approx 0.2$ and cloud optical thickness $\tau_{cloud} = 0.3$, the Sun has set in the West. In the flux (top left), no cloud is visible. In the DoP a barcode-like cloud signal is visible along the solar meridian from 60° elevation in the Western sky until roughly 50° elevation in the Eastern sky. At some parts of the sky along the solar meridian, the cloud DoP depolarizes the signal noticeably, corresponding to the darker patches in the DoP. The cloud's Q signal (bottom left) contributes most to the DoP a pattern is visible in the Eastern sky, peaking around 50 ° elevation in the East. The cloud U (bottom right) is weaker, though a very faint barcode pattern is visible in the East. The bottom plots are given with a discrete color range to be able to distinguish the orders of magnitude of the respective Q and U signals Both Q and U are one to two orders of magnitude weaker than the forward scattered dust Q and U signals in the Western sky, but the results suggest that a high elevations in the Western and Eastern sky the cloud is observable in the DoP.

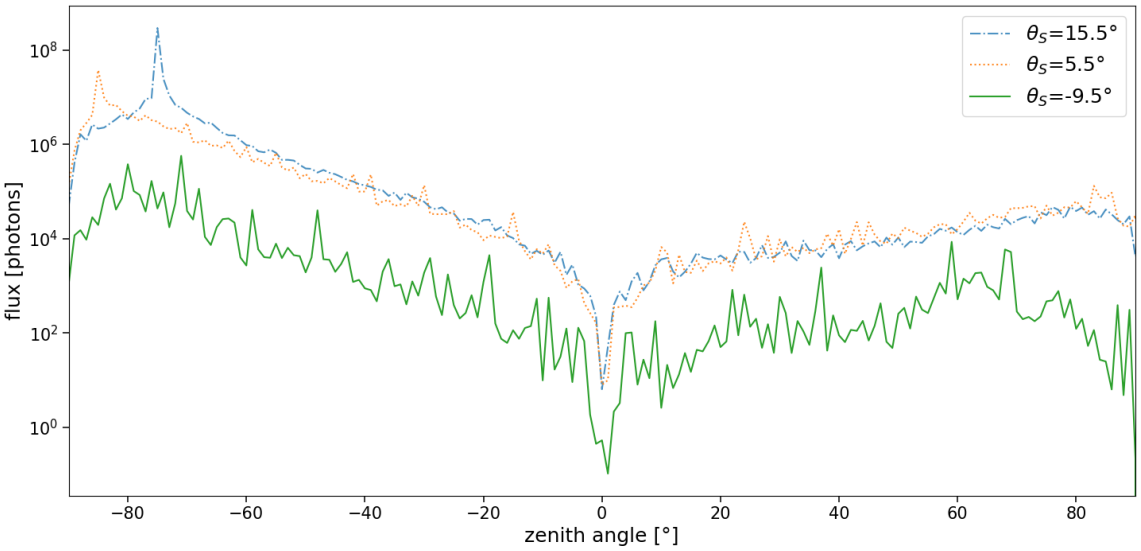

Figure 5.15: Flux along the solar meridian at the equator for simulated detectors at three solar elevation angles, θ_S, in blue light. Each detector has a 100 m thick cloud overhead but it is clear that no cloud is discernible in the flux. A cloud is present at the each of the three detectors corresponding to the three solar elevation angles. The zenith angle equals elevation minus 90°, -90° is due West, +90° is due East. The Sun is setting in the West and the lines in blue and yellow are still on the day-side, the two spikes to the left coincide with the position of the Sun. The green line is in the twilight-zone; the flux is considerably weaker and more noisy because fewer photons reached this detector.

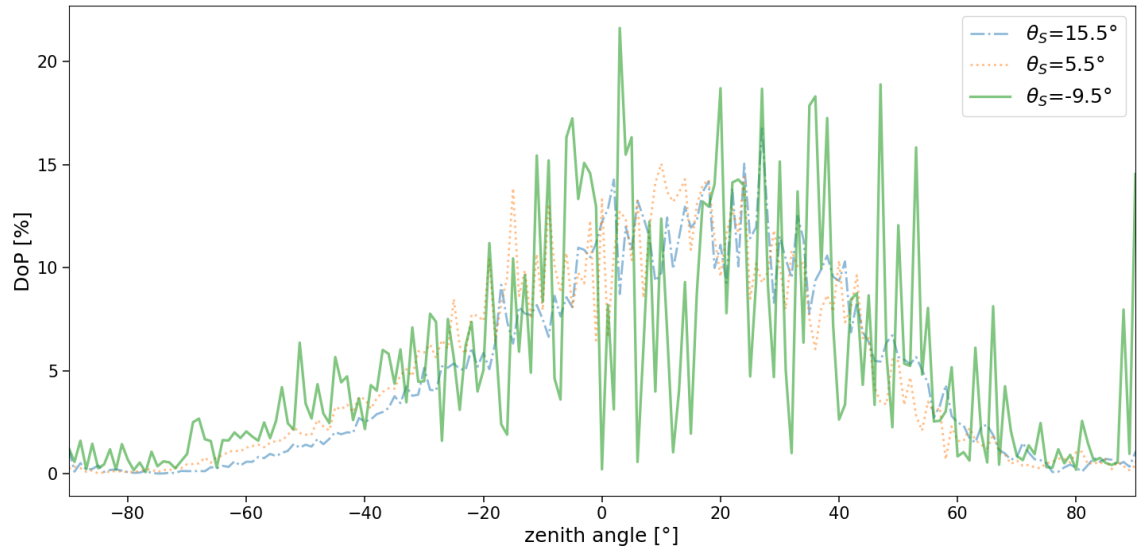

Figure 5.16: Similar to Figure 5.15 but for the DoP. The presence of a cloud is evident at $\theta_S = -9.5$ at zenith angles between -30° and +50° (elevations between 60° in the East 40° in the West). This is visible in the strong oscillations between 0 and 20% DoP that the green line exhibits, corresponding to the similar bar-code pattern seen in the DoP plot in Figures 5.14. The range in zenith angles is analogous to a range of scattering angles between 60° and 140° (singly scattered light along the solar meridian coming from zenith corresponds to a scattering angle of 90°). Thus, the simulated DoP of the cloud is distinguishable at a broad range of scattering angles.

6

Conclusions

In this chapter, conclusions of the research are given. The objective of the research was to predict the flux and polarization signals of light interacting with mesospheric CO_2 ice clouds, as observed from the Martian surface during twilight, using a spherical shell radiative transfer code.

Relevant constituents for the simulation of CO_2 ice clouds in the Martian atmosphere
The relevant constituents (next to the CO_2 ice clouds) for a radiative transfer simulation of the Martian atmosphere were identified to be CO_2 gas and dust. Optical thicknesses, single scattering albedos and scattering matrices were derived at wavelengths 0.4, 0.6 and 0.8 μm. For CO_2 gas, Rayleigh scattering theory was applied, and for the dust, experimental data from literature was used.

Derivation of optical properties of CO_2 ice
Optical constants of CO_2 ice have been calculated with the ADDA software (Yurkin and Hoekstra, 2011) for three particle shapes: cubes, octahedra and cube-octahedra. Scattering matrix elements of size distributions of these shapes have been calculated at the three considered wavelengths using a size distribution from literature.

Influence of CO_2 gas
The CO_2 gas on Mars does not obscure the CO_2 ice clouds because the Martian atmosphere is very thin. Furthermore, no second order Rayleigh scattering neutral points occur in the Martian atmosphere because the atmosphere is not optically thick enough enough.

Influence of dust
The influence of dust is of much greater importance for a surface based observation strategy than the CO_2 gas. The clouds are not visible during the day because of the dust. During twilight, the CO_2 ice clouds are more easily detected in low dust-loading scenarios. The simulations with PA3S suggest that, because of the dust, stronger cloud signals are observable in lower wavelengths. Lower wavelengths have a smaller dust optical thickness, meaning more direct light can hit the clouds. Lower wavelengths are absorbed more strongly by dust, thus the background light is weaker in lower wavelengths.

Feasibility of surface-based observation strategy
Simulations were only done for cubes because, based on calculation of optical properties of octahedra and cube-octahedra, it was determined that using these two shapes would give different DoP patterns but would have no influence on the conclusions regarding feasibility. Simulation results suggest that a surface-based observation strategy of the mesospheric CO_2 ice clouds is feasible. Data acquired from the surface can potentially characterize the CO_2 ice clouds, offering valuable insight into several processes at work in the Martian atmosphere. It will be difficult to detect the clouds in the flux because of the background dust. Detection through measurement of the DoP of the clouds is promising. Looking at a broad range of scattering angles is crucial for two reasons: firstly, to distinguish the clouds more easily from the background dust in the DoP, and secondly, to successfully determine cloud particle morphology. Different cloud particle shapes result in different DoP patterns. Patterns measured at broad scattering angles could be compared with scattering matrix elements generated with computer algorithms or with experiments to find matches. The simulated signal in Q and U is relatively weak

(around one to two orders of magnitude weaker than the strongest signal in the twilight sky), this is something that should be considered in instrument design.

Development of a flexible, spherical radiative transfer code with polarization
The PA3S code has been developed in such a way that it can be applied to other problems where sphericity of the atmosphere is not negligible. In this research, PA3S has been used for low and negative solar elevation angles, but the code can also simulate illumination conditions at high solar elevation angles. The code has been successfully validated with Rayleigh single scattering polarization portraits from literature. PA3S has also been made parallel with OpenMP for better performance. Scripts for effective visualization of PA3S output have been developed as well.

7

Discussion

In this report, the developed PA3S code has been used to predict the flux and polarization signals of mesospheric CO_2 ice clouds. Based on the predicted signal, general advice regarding a surface-based instrument is given in Sections 7.1-7.6. Finally, recommendations for extension of the PA3S code are presented in Section 7.7.

7.1. Timing and pointing of instrument

PA3S simulation results suggest that the mesospheric CO_2 clouds are observable from the surface during twilight. Simulations with a 100 m thick cloud at 70 km, showed that the cloud was visible in the degree of polarization (DoP) between solar elevation angles of -8° and -12° with the best signal at around -10° solar elevation. A vertical extent of 100 m is relatively small according to analysis by Määttänen et al. (2010). Clouds larger in vertical extent will probably be brighter and visible for longer to some degree, but at a certain size, there will be enough multiple scattering in the cloud such that the cloud DoP-signal decreases in strength. This depolarizing effect due to *cloud* multiple scattering has not been investigated in this research. This should not be confused with multiple scattering by the gas and dust which has been implemented. The strong forward scattering of the Martian dust obscures the cloud signal at lower elevation angles when looking at the Sun's half of the sky, even at large negative solar elevation angles. The cloud signal is also difficult to detect when looking in the direction of the anti-sun at low elevations. This is because little direct sunlight can reach the clouds due to the large amount of dust, and at a certain point the planet is in the way. The CO_2 ice clouds are best observable between 60° elevation in the East and 40° elevation in the West, this is analogous to a range of scattering angles between 60° and 140°.

Being able to measure large parts of the sky and at broad scattering angles is important. Observations at broad ranges of scattering angles can effectively discern the barcode-pattern visible for instance in Figures 5.10-5.13. An instrument that sees a lot of the sky at once is also less sensitive to the orientation of the platform it is mounted on, like a rover. Moreover, during real observations, the clouds will often not be perfectly homogeneous stretching over the entire sky dome above the detector (though Määttänen et al. (2010) do present an observation of a large cloud, stretching out over two-thirds of a degree in longitude and a full degree in latitude, see Figure 1.5). They could be a collection of discontinuous streaks or parts of the cloud could be obstructed by lower altitude clouds. It is not necessarily straightforward where to point the instrument at. Looking at most of the sky dome at once nullifies this problem and eliminates moving parts for pointing in the design. FlySPEX (Snik et al., 2016) is an instrument with such capabilities. See Figure 7.1 from Snik et al. (2016) for an impression of the FlySPEX design. It should be noted that saving large swaths of the sky could require high amounts of memory. Also, link budget constraints might complicate such measurements.

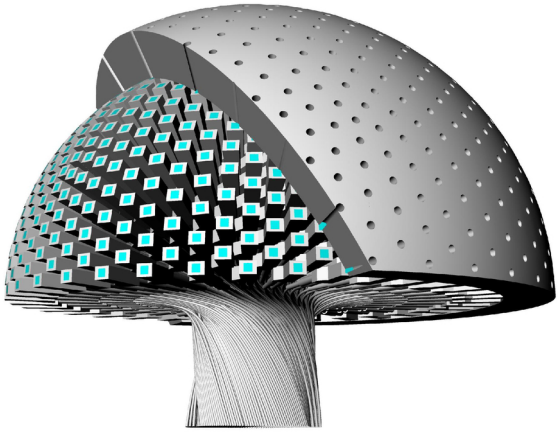

Figure 7.1: Render of the FlySPEX design from Snik et al. (2016).

7.2. Measured quantities

The clouds are barely visible in the flux and the flux does not give a lot of information on particle shape. Therefore, a good approach is to detect the DoP of a cloud for a wide range of scattering angles. A range of approximately 30° scattering angles would give already very useful information already but the broader the range, the easier it is to identify the particle shape.

A DoP pattern can be compared with the scattering matrix (P_{12}) of suspected candidates for particle shapes for qualitative information on particle shapes, sizes, composition (the condensation nuclei are not known) and refractive index. This is also possible if multiple scattering is present in the mesospheric cloud. Multiple scattering will be less polarized and will thus decrease the DoP, but it will not eliminate the pattern. This pattern could also be visible in the angle of polarization (AoP), but accurate measurements of the AoP are more difficult and would not provide more information than DoP measurements.

Even though the DoP signal of the clouds is observable in the twilight zone, the Q and U signals (which are the main contribution to the DoP) of the mesospheric CO_2 ice clouds at a low solar elevation angles have been found to be relatively weak; around one to two orders of magnitude weaker than the stronger dust Q and U signals in the Sun's part of the sky. This low photon flux has important implications for the instrument design. An instrument must be capable to perform a measurement from a relatively small amount of photons and sensitive enough to detect small differences in for example Q or U. Longer integration times could aid in this matter, but the movement of the clouds and thus the shifting of the DoP patterns should also be taken into account.

The more prevalent, thin CO_2 clouds will not be visible in the circular polarization, V. However, thicker cumulus clouds might give some signal in V, but this was not explored in this research because of the cloud single scattering simplification, see Subsection 4.3.5. However, the dust on the day side probably does give a signal in, V. Results with PA3S suggest so, see Figure 7.2. Most instruments do not measure V in planetary atmospheres because it is significantly smaller in magnitude compared to Q and U. V is thus more easily lost in the noise, meaning the measurements are more difficult and less accurate. It is interesting to note that some polarimetry approaches, like that of FlySPEX, assume that $V = 0$, which is not the case on Mars because of multiple scattering by dust. Results of PA3S could be a useful tool to estimate errors this might cause or to apply corrections.

7.3. Wavelength

The simulations where done at three wavelengths: 0.4, 0.6 and 0.8 μm. Observing in smaller wavelengths is the most promising. Firstly, the P_{12}-element for all combinations of particle shape and wavelength in Chapter 3 showed more complexity across the range of scattering angles for 0.4 μm than for the longer wavelengths. The effect of element P_{12} is the most significant on the DoP because the more prevalent cirrus-type clouds are thin and photons will likely not scatter often in the clouds. Though,

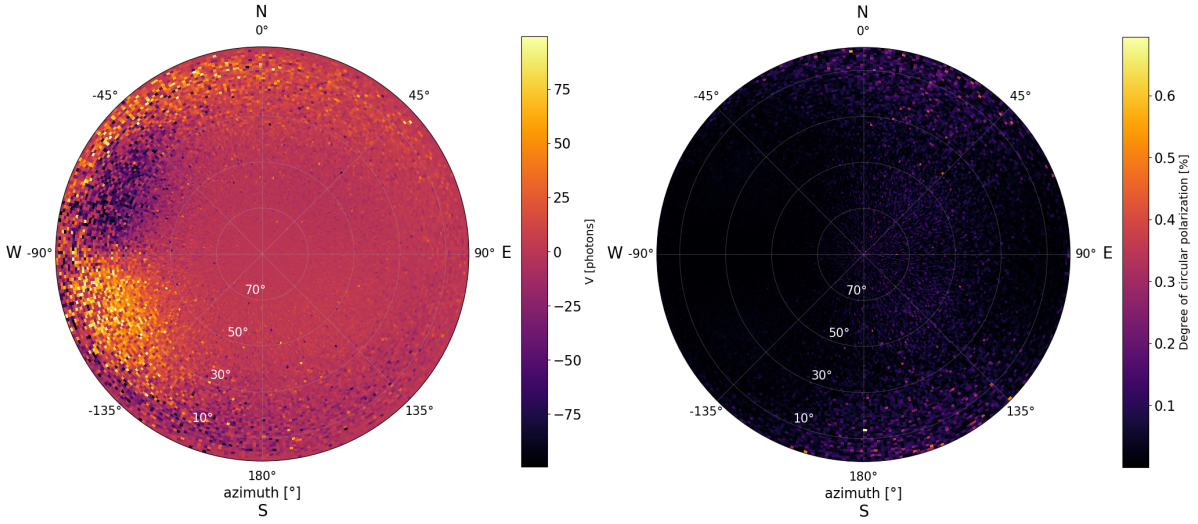

Figure 7.2: PA3S results for dust on the day side, solar elevation angle is 20.5°, the Sun is in the West. There is a signal in V (left plot) caused by multiple scattering by dust when looking West. The dust scattering matrix, shown in Figure 2.6, exhibits strong forward scattering, explaining the high amount of multiply scattered light coming from the West. In the right plot, the degree of circular polarization is shown, $DoCP = V/I$. It is clear that this signal is very weak, $< 1\%$.

because at smaller wavelengths the number of features over the range of scattering angles is higher, a better angular resolution might be necessary at smaller wavelengths. Secondly, the Martian dust is more optically thick for wavelengths of 0.6 and 0.8 μm, because of the wavelength dependence of the Martian dust extinction coefficient, $Q_{ext}(\lambda)$, as seen in Figure 2.8 from Smith et al. (2013). PA3S simulation indicate that more blue light will directly hit the mesospheric clouds and less scattered blue light from the background dust and gas will be present in the twilight zone. In contrast to the wavelength dependence of the cloud particle scattering matrix, the wavelength dependence of the cloud optical thickness has not been taken into account. Results for wavelengths of 0.4, 0.6, 0.8 μm were generated with the same cloud optical thickness based on the range found by Määttänen et al. (2010) ($\tau = 0.01 - 0.6$ and median values of $0.13 - 0.2$). This dependency could be included for further refinement of the results.

7.4. Measurement season

The Martian dust is the most significant factor that obscures the CO_2 ice clouds when observing them from the surface. Even when the atmosphere is at its clearest, the dust total optical thickness rarely is below 0.2, see Figure 2.9 (Smith et al., 2013). The best time to observe the mesospheric clouds is when there is a higher chance of the mesospheric clouds forming and when dust loading is lowest. Luckily, there is overlap between these time windows. This is no coincidence since the Martian dust heats up the atmosphere (Clancy et al., 2000). Määttänen et al. (2010) compared mesospheric cloud observations with output of a General Circulation Model (GCM). They concluded that most of the clouds were detected where the GCM predicted the coldest temperatures at mesospheric altitudes, at solar longitudes of $L_S = 0 - 30°$. Smith et al. (2013) mention that considerably more dust is present during perihelion season ($L_S = 180 - 360°$) than during aphelion season ($L_S = 0 - 180°$). The dust also reaches higher altitudes during perihelion season, potentially blocking direct sunlight that would have otherwise hit the clouds during the twilight period.

7.5. Cloud particle single scattering calculations

The cloud particle scattering matrices were calculated using the software package ADDA (Yurkin and Hoekstra, 2011). Simulations were run at reasonable grid sizes and until convergence. However, at larger size parameters simulation runs took up a lot of computing time. ADDA was used in parallel mode, but the available number of cores was limited. Some ADDA runs at high size parameters where done at lower refractive indices as mentioned in Section 3.5 to shorten run times. This is not ideal, run times could be shortened using more cores or other methods of calculating the cloud particle scattering

matrices could be looked into and compared with ADDA.

Also, ADDA simulation were performed for three particle shapes (cubes, octahedra and cube-octahedra) at three wavelengths (0.4, 0.6 and 0.8 μm) for one size distribution (1-3 μm, based on analysis by Määttänen et al. (2010)). For interpretation of actual observations, more ADDA results for more combinations of shapes, wavelengths and size distributions should be generated. Possibly, these could be combined with scattering matrices derived from experimental measurements. Mangan et al. (2017) created CO_2 ice crystals under Martian atmospheric circumstances and give a description of their method. They did not measure a scattering matrix however. Similar experiments for other particles have been done by other studies, for example Laan et al. (2009). A collection of such results is available in the Amsterdam-Granada light scattering database (Muñoz et al., 2012).

Furthermore, the ADDA output used to generate scattering matrices of size distributions of cloud particles were generated with a real refractive index that was assumed to be constant in the visible spectrum, and with an imaginary refractive index that was set to zero. These assumptions were deemed appropriate for the accuracy required in this research, see Section 3.5. ADDA simulations could be performed using a wavelength-dependent real refractive index and/or including the imaginary refractive index, but such a refinement would only be relevant in the context of a comparison of actual measurements with ADDA results.

7.6. Further analysis with PA3S

For further analysis of a surface-based observational strategy and for instrument sizing, PA3S results can be used. It is advisable to increase signal-to-noise-ratio of PA3S output with more photons, this could be done on more powerful computers with more cores. Furthermore, it is recommended to perform simulations for more dust loading scenarios and more cloud settings (optical thickness, vertical and horizontal extent representing cirrus vs. cumulus clouds).

7.7. Recommendations for extension of the code

Adding cloud multiple scattering

In Subsection 4.3.5, it was noted that cloud interaction is simulated as a photon intersecting a spherical shell segment. Subsequently, the maximum distance travelled through the cloud is compared with the slanted thickness of the cloud (see Figure 4.12 for a depiction) to check whether or not the photon scatters or passes through the cloud. This means that only single scattering is supported in the cloud. Such a method is acceptable for the mesospheric Martian clouds since they are relatively optically thin. However, it is not suitable for clouds that are very large or very dense, such as cumulus clouds on Earth. In such a situation a cloud cell is better suited. Such a cell could have six walls, a photon can scatter multiple times within this cell. After each scatter it should be checked if the photon has crossed one of the walls of the cloud cell.

Surface reflection

Currently the code does not include surface reflection. Since the context of this report was a surface-based observation strategy, this feature was not developed. During twilight conditions, light reflected from the Martian surface is negligible and will have little effect obscuring the cloud signals. For another application where surface reflection is not negligible, it can straightforwardly be added.

Water ice clouds

Smith et al. (2013) mentions that water ice clouds are often found atop dust layers. Such water clouds could possibly be confused for CO_2 clouds. Therefore, evaluation of their flux and polarization signals might be useful. Addition of such clouds into the code would be a fairly straightforward process. It would simply require the addition of a cloud with optical properties corresponding to water ice under Martian atmospheric conditions.

Adding dependence of scattering matrix on incoming photon direction

All the atmospheric constituents in PA3S have been assumed to be randomly oriented. Because of this, the scattering matrix is independent of the orientation of a scattering particle with respect to the incoming photon direction. In some situations, the assumption of randomly oriented particles is not valid. For example, in Earth's atmosphere, thin hexagonal ice crystals can all align horizontally in

still air. Refraction of sunlight hitting such horizontally aligned crystals is known to cause two optical phenomena: sun dogs and circumzenithal arcs.

Two things would have to be done to account for this effect, regarding both ADDA and PA3S. In this research, ADDA results have been generated with a setting that averages over all incoming directions of a light beam, resulting in one scattering matrix for all combinations of incoming photon directions and particle orientations. Thus, to account for the aforementioned effect, different scattering matrices would have to be generated, with ADDA or with similar software, for different directions of the incoming light beam with respect to the orientation of the scattering particle. Subsequently, an extension to PA3S should be added that identifies the correct scattering matrix that should be sampled, based on the angle between the incoming photon direction and orientation of the particle. The current photon direction is always known in PA3S. Particle orientation could be defined as some angle with respect to the local horizon.

Placement of detectors in the atmosphere
In this research all detectors were placed on the surface and hence only elevations from 0° to 90° have been considered. Implementing a detector placed in the atmosphere using the full elevation range (-90° to 90°) has not been tested but could be easily added. A possible application for such a setting is to simulate measurements by balloons.

Bibliography

Aoki, S., Sato, Y., Giuranna, M., Wolkenberg, P., Sato, T. M., Nakagawa, H., and Kasaba, Y. Mesospheric CO2 ice clouds on Mars observed by Planetary Fourier Spectrometer onboard Mars Express. *Icarus*, 302:175–190, 2018.

Ayranci, I., Vaillon, R., and Selçuk, N. Performance of discrete dipole approximation for prediction of amplitude and phase of electromagnetic scattering by particles. *Journal of Quantitative Spectroscopy and Radiative Transfer*, 103(1):83–101, 2007. ISSN 00224073. doi: 10.1016/j.jqsrt.2006.06.006.

Clancy, R. T. and Sandor, B. J. CO2 ice clouds in the upper atmosphere of Mars. *Geophysical Research Letters*, 25(4):489–492, 1998. doi: 10.1029/98GL00114. URL https://agupubs.onlinelibrary.wiley.com/doi/abs/10.1029/98GL00114.

Clancy, R. T., Sandor, B. J., Wolff, M. J., Christensen, P. R., Smith, M. D., Pearl, J. C., Conrath, B. J., and Wilson, R. J. An intercomparison of ground-based millimeter, MGS TES, and Viking atmospheric temperature measurements: Seasonal and interannual variability of temperatures and dust loading in the global Mars atmosphere. *Journal of Geophysical Research E: Planets*, 105(E4):9553–9571, 2000. ISSN 01480227. doi: 10.1029/1999JE001089.

Clancy, R. T., Wolff, M. J., Whitney, B. A., Cantor, B. A., and Smith, M. D. Mars equatorial mesospheric clouds: Global occurrence and physical properties from Mars Global Surveyor Thermal Emission Spectrometer and Mars Orbiter Camera limb observations. *Journal of Geophysical Research: Planets*, 112(E4), 2007.

Creasey, J. E., Forbes, J. M., and Hinson, D. P. Global and seasonal distribution of gravity wave activity in Mars' lower atmosphere derived from MGS radio occultation data. *Geophysical research letters*, 33(1), 2006.

de Haan, J. F., Bosma, P. B., and Hovenier, J. W. The adding method for multiple scattering calculations of polarized light. *Astronomy and Astrophysics*, 183:371–391, 1987.

De Rooij, W. A. and Van der Stap, C. C. A. H. Expansion of Mie scattering matrices in generalized spherical functions. *Astronomy and Astrophysics*, 131:237–248, 1984.

Dowling, D. R. and Radke, L. F. A summary of the physical properties of cirrus clouds, 1990. ISSN 08948763.

Draine, B. T. and Flatau, P. J. Discrete-dipole approximation for scattering calculations. *JOSA A*, 11 (4):1491–1499, 1994.

Egan, W. G. and Spagnolo, F. A. Complex index of refraction of bulk solid carbon dioxide. *Applied optics*, 8(11):2359–2360, 1969.

Ehlers, K., Chakrabarty, R., and Moosmüller, H. Blue moons and Martian sunsets. *Applied optics*, 53 (9):1808–1819, 2014.

Gondet, B., Montmessin, F., Langevin, Y., Bibring, J., Drossart, P., Forget, F., and Fouchet, T. Hyperspectral imaging if convective CO2 ice clouds in the equatorial mesosphere of mars. In *Bulletin of the American Astronomical Society*, volume 39, page 472, 2007.

GrabCad. Basic Geometric Shapes 3D, 2019. URL https://grabcad.com/library/basic-geometric-shapes-3d-1. [Online; accessed 10-10-2019].

Haberle, R. M. et al. *The Atmosphere and Climate of Mars*. Cambridge Planetary Science. Cambridge University Press, 2017. doi: 10.1017/9781139060172.

Hansen, J. E. and Travis, L. D. Light scattering in planetary atmospheres. *Space science reviews*, 16 (4):527–610, 1974.

Hartwick, V. L., Toon, O. B., and Heavens, N. G. High-altitude water ice cloud formation on Mars controlled by interplanetary dust particles. *Nature Geoscience*, 12(7):516–521, 2019. ISSN 17520908. doi: 10.1038/s41561-019-0379-6. URL http://dx.doi.org/10.1038/s41561-019-0379-6.

Herr, K. C. and Pimentel, G. C. Evidence for solid carbon dioxide in the upper atmosphere of Mars. *Science*, pages 47–49, 1970.

Horváth, G. *Polarized light and polarization vision in animal sciences, second edition*. Number December. 2014. ISBN 9783642547188. doi: 10.1007/978-3-642-54718-8.

Horváth, G., Gál, J., Pomozi, I., and Wehner, R. Polarization portrait of the Arago point: Video-polarimetric imaging of the neutral points of skylight polarization. *Naturwissenschaften*, 85(7):333–339, 1998. ISSN 00281042. doi: 10.1007/s001140050510.

Horváth, G., Bernáth, B., Suhai, B., Barta, A., and Wehner, R. First observation of the fourth neutral polarization point in the atmosphere. *Journal of the Optical Society of America A*, 19(10):2085, 2002. ISSN 1084-7529. doi: 10.1364/josaa.19.002085.

Hovenier, J. W. et al. *Transfer of Polarized Light in Planetary Atmospheres*. Springer Netherlands, Dordrecht, 1st edition, 2004.

Hovenier, J. and Van der Mee, C. Fundamental relationships relevant to the transfer of polarized light in a scattering atmosphere. *Astronomy and Astrophysics*, 128:1–16, 1983.

Hulst, H. C. v. d. *Light scattering by small particles*. Courier Corporation, 1981.

Hunter, J. D. Matplotlib: A 2d graphics environment. *Computing In Science & Engineering*, 9(3):90–95, 2007.

Isenor, M., Escribano, R., Preston, T. C., and Signorell, R. Predicting the infrared band profiles for CO2 cloud particles on Mars. *Icarus*, 223(1):591–601, 2013.

Kislat, F., Clark, B., Beilicke, M., and Krawczynski, H. Analyzing the data from X-ray polarimeters with Stokes parameters. *Astroparticle Physics*, 68:45–51, 2015. ISSN 0927-6505. doi: https://doi.org/10.1016/j.astropartphys.2015.02.007. URL http://www.sciencedirect.com/science/article/pii/S092765051500033X.

Laan, E. C., Volten, H., Stam, D. M., Munoz, O., Hovenier, J. W., and Roush, T. L. Scattering matrices and expansion coefficients of martian analogue palagonite particles. *Icarus*, 199(1):219–230, 2009.

Laboratory of Paper Coating and Converting at Åbo Akademi University. Litebil. URL http://users.abo.fi/jkniivil/litebil/.

Lemmon, M. T., Wolff, M. J., Bell, J. F., Smith, M. D., Cantor, B. A., and Smith, P. H. Dust aerosol, clouds, and the atmospheric optical depth record over 5 Mars years of the Mars Exploration Rover mission. *Icarus*, 251:96–111, 2015. ISSN 10902643. doi: 10.1016/j.icarus.2014.03.029.

Määttänen, A., Montmessin, F., Gondet, B., Scholten, F., Hoffmann, H., González-Galindo, F., Spiga, A., Forget, F., Hauber, E., Neukum, G., et al. Mapping the mesospheric CO2 clouds on Mars: MEx/OMEGA and MEx/HRSC observations and challenges for atmospheric models. *Icarus*, 209(2):452–469, 2010.

Mangan, T. P., Salzmann, C. G., Plane, J. M. C., and Murray, B. J. CO2 ice structure and density under Martian atmospheric conditions. *Icarus*, 294:201 – 208, 2017. ISSN 0019-1035. doi: https://doi.org/10.1016/j.icarus.2017.03.012. URL http://www.sciencedirect.com/science/article/pii/S0019103516306832.

McConnochie, T. H., Bell III, J. F., Savransky, D., Wolff, M. J., Toigo, A. D., Wang, H., Richardson, M. I., and Christensen, P. R. THEMIS-VIS observations of clouds in the Martian mesosphere: Altitudes, wind speeds, and decameter-scale morphology. *Icarus*, 210(2):545–565, 2010.

Mischenko, M. I. et al. Concepts, terms, notation. In Mischenko, M. I. et al., editors, *Light Scattering by Nonspherical Particles*. Academic Press, San Diego, California, 2000.

Montabone, L., Lemmon, M. T., Smith, M. D., Wolff, M. J., Forget, F., and Millour, E. Reconciling dust opacity datasets and building multi-annual dust scenarios for Mars atmospheric models. *Fourth International Workshop on the Mars Atmosphere: Modelling and Observations, 8-11 February 2011, Paris, France*, 4:103–105, 2011. URL http://www-mars.lmd.jussieu.fr/paris2011/abstracts/montabone2_paris2011.pdf.

Montmessin, F., Bertaux, J. L., Quémerais, E., Korablev, O., Rannou, P., Forget, F., Perrier, S., Fussen, D., Lebonnois, S., Rébérac, A., and Dimarellis, E. Subvisible CO2 ice clouds detected in the mesosphere of Mars. *Icarus*, 183(2):403–410, 2006. ISSN 00191035. doi: 10.1016/j.icarus.2006.03.015.

Montmessin, F., Gondet, B., Bibring, J. P., Langevin, Y., Drossart, P., Forget, F., and Fouchet, T. Hyperspectral imaging of convective CO2 ice clouds in the equatorial mesosphere of Mars. *Journal of Geophysical Research E: Planets*, 112(11):1–14, 2007. ISSN 01480227. doi: 10.1029/2007JE002944.

Muñoz, O., Moreno, F., Guirado, D., Dabrowska, D. D., Volten, H., and Hovenier, J. W. The Amsterdam-Granada Light Scattering Database. *Journal of Quantitative Spectroscopy and Radiative Transfer*, 113(7):565–574, 2012. ISSN 00224073. doi: 10.1016/j.jqsrt.2012.01.014.

Nave, C. R. Classification of Polarization, 2017. http://hyperphysics.phy-astr.gsu.edu/hbase/phyopt/polclas.html.

Penttilä, A., Zubko, E., Lumme, K., Muinonen, K., Yurkin, M. A., Draine, B., Rahola, J., Hoekstra, A. G., and Shkuratov, Y. Comparison between discrete dipole implementations and exact techniques. *Journal of Quantitative Spectroscopy and Radiative Transfer*, 106(1-3):417–436, 2007. ISSN 00224073. doi: 10.1016/j.jqsrt.2007.01.026.

Pomozi, I., Horváth, G., and Wehner, R. How the clear-sky angle of polarization pattern continues underneath clouds: Full-sky measurements and implications for animal orientation. *Journal of Experimental Biology*, 204(17):2933–2942, 2001. ISSN 00220949.

Schuh, R. Arbitrary particle shape modeling in ddscat and validation of simulation results. In Wriedt, T. and Hoekstra, A. G., editors, *Proceedings of the DDA - Workshop*, pages 22–24. Institut fur Werkstofftechnik, March 2007. doi: http://diogenes.iwt.uni-bremen.de/vt/laser/papers/DDA-Workshop-final-proceedings.pdf.

Schulze, W. and Abe, H. Density, refractive index and sorption capacity of solid CO2 layers. *Chemical Physics*, 52(3):381–388, 1980.

Seiber, B. A., Smith, A. M., Wood, B. E., and Müller, P. R. Refractive indices and densities of H2O and CO2 films condensed on cryogenic surfaces. *Applied optics*, 10(9):2086–2089, 1971.

Smith, M. D., Wolff, M. J., Clancy, R. T., Kleinböhl, A., and Murchie, S. L. Vertical distribution of dust and water ice aerosols from CRISM limb-geometry observations. *Journal of Geophysical Research E: Planets*, 118(2):321–334, 2013. ISSN 01480227. doi: 10.1002/jgre.20047.

Snik, F., Keller, C. U., Wijnen, M., Peters, H., Derks, R., and Smulders, E. FlySPEX: a flexible multi-angle spectropolarimetric sensing system. *Polarization: Measurement, Analysis, and Remote Sensing XII*, 9853(May 2016):985308, 2016. ISSN 1996756X. doi: 10.1117/12.2223824.

Spiga, A., González-Galindo, F., López-Valverde, M.-Á., and Forget, F. Gravity waves, cold pockets and CO2 clouds in the Martian mesosphere. *Geophysical Research Letters*, 39(2), 2012.

Subirana, J. S., Zornoza, J. M., and Hernández-Pajares, M. Transformations between ECEF and ENU coordinates, 2011. URL https://gssc.esa.int/navipedia/index.php/Transformations_between_ECEF_and_ENU_coordinates. [Online; accessed 10-04-2019].

Tempelmeyer, K. E. and Mills, D. W. Refractive index of carbon dioxide cryodeposit. *Journal of Applied Physics*, 39(6):2968–2969, 1968. ISSN 00218979. doi: 10.1063/1.1656707.

The HDF Group. Hierarchical Data Format, version 5, 1997-2019. http://www.hdfgroup.org/HDF5/.

Vincendon, M., Pilorget, C., Gondet, B., Murchie, S., and Bibring, J.-P. New near-IR observations of mesospheric CO2 and H2O clouds on Mars. *Journal of Geophysical Research: Planets*, 116(E11), 2011. doi: 10.1029/2011JE003827. URL https://agupubs.onlinelibrary.wiley.com/doi/abs/10.1029/2011JE003827.

Warren, S. G. Optical constants of carbon dioxide ice. *Applied Optics*, 25(16):2650, 1986. ISSN 0003-6935. doi: 10.1364/ao.25.002650.

Washburn, E. W. and West, C. J. *International critical tables of numerical data, physics, chemistry and technology*. McGraw Hill, New York, 1948.

Wertz, J. R. *Mission Geometry; Orbit and Constellation Design and Management*. Springer, 2001.

Wood, K., Whitney, B., and Bjorkman, J. Introduction to Monte Carlo Radiation Transfer. 2013.

Young, A. T. Rayleigh scattering. *Applied Optics*, 20(4):533–535, Feb 1981. doi: 10.1364/AO.20.000533. URL http://ao.osa.org/abstract.cfm?URI=ao-20-4-533.

Yurkin, M. A. and Hoekstra, A. G. The discrete-dipole-approximation code ADDA: Capabilities and known limitations. *Journal of Quantitative Spectroscopy and Radiative Transfer*, 112(13):2234–2247, 2011. ISSN 0022-4073. doi: https://doi.org/10.1016/j.jqsrt.2011.01.031. URL http://www.sciencedirect.com/science/article/pii/S0022407311000562.

Yurkin, M. A. and Hoekstra, A. G. User Manual for the Discrete Dipole Approximation Code. pages 1–64, 2014. URL http://a-dda.googlecode.com/svn/tags/rel{_}1.3b4/doc/manual.pdf.

Yurkin, M. A., Maltsev, V. P., and Hoekstra, A. G. The discrete dipole approximation for simulation of light scattering by particles much larger than the wavelength. *Journal of Quantitative Spectroscopy and Radiative Transfer*, 106(1-3):546–557, 2007. ISSN 00224073. doi: 10.1016/j.jqsrt.2007.01.033.

Zhao, H., Xu, W., Zhang, Y., Li, X., Zhang, H., Xuan, J., and Jia, B. Polarization patterns under different sky conditions and a navigation method based on the symmetry of the AOP map of skylight. *Optics Express*, 26(22):28589, 2018. doi: 10.1364/oe.26.028589.